

**NEW COMPUTATIONAL METHODS FOR 3D STRUCTURE
DETERMINATION OF MACROMOLECULAR COMPLEXES BY SINGLE
PARTICLE CRYO-ELECTRON MICROSCOPY**

Dissertation

zur Erlangung des mathematisch-naturwissenschaftlichen Doktorgrades

"Dr. rerum naturalium"

an der Georg-August-Universität Göttingen

vorgelegt von

Martin Schmeißer

aus Hamburg

Göttingen 2009

Members of Thesis Committee:

Prof. Dr. Holger Stark (First Referee)

Prof. Dr. Ralf Ficner (Second Referee)

Prof. Dr. Erwin Neher

Affirmation

I hereby declare that this thesis has been written independently and with no other sources and aids than quoted.

Göttingen, 12.3.2009

Martin Schmeißer

Publications and Software

Publications

Parts of this thesis have been published, submitted to publication or presented at conferences:

Schmeisser, M., B. C. Heisen, M. Luettich, B. Busche, F. Hauer, T. Koske, K.-H. Knauber and H. Stark (2009). "Parallel, distributed and GPU computing technologies in single particle electron microscopy." Acta Crystallogr D **Accepted Manuscript**.

Schmeisser, M., B. C. Heisen, H. Stark, D. Moser and A. S. Frangakis (2008). Parallel processing with graphics cards. Workshop. New Algorithms in Macromolecular Crystallography and Electron Microscopy. J. P. Abrahams. Leiden, NL.

Schmeisser, M. and H. Stark (2009). Method and device for recording and processing projection images. PCT/EP2009/000435. M.-P.-G. z. F. d. W. e.V. Germany, European Patent Office.

Luettich, M., B. Sander, B. C. Heisen, M. Schmeisser, B. Busche and H. Stark (2008). 3D Structure Determination of Dynamic Macromolecular Complexes by single particle cryo-EM. New Algorithms in Macromolecular Crystallography and Electron Microscopy. J. P. Abrahams. Leiden, NL.

Hauer, F., N. Fischer, U. Kothe, M. Schmeisser, M. V. Rodnina and H. Stark (2009). An extended ribosomal L7/L12 stalk and ribosomal expansion segments on the large ribosomal subunit of *Thermotoga maritima* as revealed by 3D cryo-EM. **To appear in Journal of Structural Biology**.

Software

The following software has been developed within the context of this thesis:

AmiraImagic: A plug in for import and manipulation of Imagic data in the Mercury Amira Visualization package.

3DMC: A tool for three-dimensional mass centering of models.

ImportExport: A tool for storing and administration of EM Projects and Data in a relational Database.

ClustWatch: A tool for administration of a plurality of computing nodes, administration of computing time, resources and tasks.

SmartTray: Framework for volunteer and cluster computing

Supervised Alignment Tools: Tools for MRA to multiple sets of references including CCC based partitioning of results.

3DView: A 3D viewer to compare, visualize and analyze a plurality of 3D models

EulerLib: A library for storing, calculating and manipulating projection directions

ClustCMD: Command Line Tools for ImportExport, Clustwatch and SmartTray for scripting use

Table of Contents

Affirmation.....	3
Publications and Software.....	4
Publications.....	4
Software	5
List of Figures.....	9
List of Tables	12
List of Abbreviations	13
ABSTRACT	15
ACKNOWLEDGEMENTS	16
1 Introduction	17
1.1 Methods for structure determination of macromolecular assemblies	17
1.1.1 Single particle electron microscopy.....	17
1.1.2 Crystallographic methods.....	18
1.2 Fundamentals of light microscopy.....	18
1.2.1 Optical transfer function.....	20
1.2.2 Resolution.....	22
1.3 Electron microscopy.....	23
1.3.1 Electron properties.....	23
1.3.2 Electron optics.....	26
1.3.3 The Fourier transform.....	27
1.3.4 Image formation.....	30
1.3.5 Phase contrast.....	31
1.3.6 Phase-contrast-transmission function (PCTF)	34
1.4 Single particle analysis	37
1.4.1 Image acquisition	40
1.4.2 Preparation of data sets for single particle analysis.....	41
1.4.3 Alignment	43
1.4.4 Multivariate statistical analysis and clustering of aligned images	46
1.4.5 Iterative approach	49
1.5 Assignment of projection directions	50
1.5.1 Definition of Euler angles	50
1.5.2 Established methods for assignment of projection directions.....	52
1.5.3 Angular reconstitution	52

1.5.4	Tilt series	53
1.5.5	Random Conical Tilt (RCT)	54
1.5.6	Orthogonal tilt	55
1.6	Reconstruction techniques.....	56
1.6.1	Fourier based methods.....	57
1.6.2	Direct methods	57
1.6.3	Iterative methods	58
1.6.4	Refinement via projection matching once a start structure is determined.....	58
1.7	Determination of obtained resolution by Fourier-Shell-Correlation (FSC)	60
1.8	Improvement of processing speed for algorithms used in EM.....	62
1.8.1	Need for speed.....	62
1.8.2	How to improve computational speed?	63
1.8.3	Divide et impera.....	64
1.8.4	Hardware architectures and their implications for parallel processing	64
1.8.5	If you can't have a faster CPU use more of them.....	66
1.8.6	Shared memory computing	67
1.8.7	Farming.....	67
1.8.8	GPU computing.....	68
1.8.9	Historical - Limitations alleged by Amdahl's law.....	69
1.8.10	Data parallel programming	71
1.9	Change your code	72
1.9.1	Software standards for shared memory and distributed computing.....	72
1.9.2	Software standards for GPU programming.....	74
1.10	Aim of the work	75
2	Materials and methods	76
2.1	Software	76
2.2	Biochemical methods.....	77
2.2.1	Chemicals.....	77
2.2.2	Buffers and solutions	78
2.2.3	Laboratory materials.....	79
2.2.4	Special equipment	80
2.2.5	Bacterial samples and plasmids.....	81
2.3	EM imaging conditions	82
2.4	Preparation of EM samples.....	83

2.4.1	Preparation of holey carbon film coated EM grids	83
2.4.2	Preparation of EM samples for negative stain electron microscopy.....	83
2.4.3	Preparation of cryo EM samples	85
3	Results.....	86
3.1	Towards 3D structure determination of Acetyl-CoA Carboxylase from <i>Corynebacterium glutamicum</i>	86
3.1.1	Purification of AccBC-AccD1 complex from <i>C. glutamicum</i> strain Δ pyc paacBC p-H6D1	87
3.1.2	Negative stain EM of Acetyl CoA-Carboxylase complex AccBC-AccD1	88
3.1.3	Optimization of purification of AccBC-AccD1 complex from <i>C. glutamicum</i> strain Δ pyc paacBC p-H6D1 for EM	91
3.1.4	RCT negative stain EM of Acetyl CoA-Carboxylase complex AccBC-AccD1 after optimized purification	92
3.2	Getting ready for the next hardware generation.....	97
3.2.1	The SmartTray	97
3.2.2	Foundations for GPU computing.....	100
3.3	Getting ready for the next generation of instrumentation.....	101
3.3.1	New methods for computation of missing cone free starting models	102
3.3.2	Connectivity graph.....	103
3.3.3	Informative value of connectivity graphs	115
3.3.4	Influences of misclassification and alignment errors on the connectivity graph and assigned projection directions.....	116
3.3.5	Separation of conformational differences.....	117
3.3.6	Influence of alignment and tilt errors on reconstructed starting models	122
4	Discussion.....	128
5	Bibliography	135
	Curriculum Vitae	150

List of Figures

Figure 1-1 Diffraction	18
Figure 1-2 The convolution of an object and an aberrated PSF.....	19
Figure 1-3 The PSF for a perfect optical system	19
Figure 1-4 Airy disks for different pupil diameters	20
Figure 1-5 The PSF of a typical human eye depending on the present pupil diameter.....	20
Figure 1-6 The Transfer of spatial frequencies through an optical system	21
Figure 1-7 Visualization of the Rayleigh criterion for resolution.....	22
Figure 1-8 Aberration correction in light optics.....	26
Figure 1-9 Spherical aberration correction in electron optics	27
Figure 1-10 Zernike like phase plates in electron optics.....	32
Figure 1-11 Transformation of phase contrast to amplitude contrast	33
Figure 1-12 The pCTF at different defoci.....	36
Figure 1-13 A “biological macromolecule” in different conformations.....	37
Figure 1-14 Projection views generated by “conformation 1”.....	38
Figure 1-15 Projection views generated by “conformation 2”.....	39
Figure 1-16 Particles in the specimen.....	40
Figure 1-17 Example of raw data.....	42
Figure 1-18 Preparation steps for further digital images processing	43
Figure 1-19 Translational and rotational degrees of freedom in 2D Alignment	44
Figure 1-20 References for the "reference free" alignment scheme	46
Figure 1-21 Alignment and “class averages”	47
Figure 1-22 Iterative alignment and classification.....	49
Figure 1-23 Angular reconstitution	52
Figure 1-24 Random Conical Tilt.....	55
Figure 1-25 Orthogonal Tilt Reconstruction	56
Figure 1-26 Projection matching.....	59
Figure 1-27 A „healthy“ FSC.....	61
Figure 1-28 Examples of „unhealthy“ FSC plots	62
Figure 1-29 The von Neumann Architecture	65
Figure 1-30 Flynn’s Taxonomy	66
Figure 1-31 GPU Hardware Architecture	68
Figure 1-32 Amdahl’s law.....	70
Figure 1-33 Gustafson-Barsis law.....	71

Figure 2-1 Cryo microscope CM200 FEG	82
Figure 2-2 The "Sandwich" preparation technique	84
Figure 3-1 Acetyl-CoA Carboxylase Gel Filtration Plots	87
Figure 3-2 Spot Scan of fractions between 45 and 55 ml from A-CoA gel filtration.....	89
Figure 3-3 Typical 2D MSA based A-CoA class averages from A-CoA	90
Figure 3-4 Comparison of typical 2D A-CoA class sums.....	90
Figure 3-5 Spot scan of gel filtration peak 55 – 65 ml from A-CoA gel filtration.....	91
Figure 3-6 Tilted Pairs from A-CoA	93
Figure 3-7 2D class sums from A-CoA obtained after GraFix	93
Figure 3-8 Comparison of 2D class sums from A-CoA	94
Figure 3-9 Artificial 3D models from A-CoA	95
Figure 3-10 Artificial models of the likely overall organization of AccBC-AccD1 complex..	96
Figure 3-11 2D class sums from A-CoA, cryo in holes	96
Figure 3-12 The Workflow of the “SmartTray” Framework	99
Figure 3-13 A list of Nodes running the Smart Tray is kept on the Master server.....	100
Figure 3-14 FEI “Titan Cryos” cryo electron microscope	102
Figure 3-15 Schematic illustration of tilt and class sum relations of projection images	103
Figure 3-16 Definition of spherical polar coordinates	104
Figure 3-17 The first untilted image (UT1) used as the starting point for the algorithm ...	105
Figure 3-18 Alignment untilted side.....	105
Figure 3-19 Tilt from untilted to tilted side.....	106
Figure 3-20 Alignment on untilted side, tilt from untilted to tilted side	107
Figure 3-21 Alignment untilted, tilt from untilted to tilted side, alignment tilted side	108
Figure 3-22 Tilt from untilted to tilted side, alignment on tilted side.....	108
Figure 3-23 Tilt untilted to tilted side, alignment tilted, tilt tilted to untilted side	109
Figure 3-24 Alignment untilted, untilted to tilted, alignment tilted, tilt tilted to untilted .	110
Figure 3-25 First step of the new approach.....	112
Figure 3-26 Building up of a connectivity graph and assignment of projection directions .	113
Figure 3-27 Relationships utilized for connectivity graph and projection directions.....	114
Figure 3-28 Sample connectivity graph obtained	115
Figure 3-29 Validation of circular subgraphs.....	117
Figure 3-30 Connectivity graph for perfect classification	119
Figure 3-31 Connectivity graph systematic miss classification	120
Figure 3-32 Connectivity graph cross miss classification	121

Figure 3-33 Models from RCT and new method reconstruction..... 123
Figure 3-34 Influence of alignment and tilt inaccuracy..... 125
Figure 3-35 Quality of models with known alignment and tilt inaccuracy..... 126
Figure 3-36 Reconstructed models quality..... 127

List of Tables

Table 2-1 Software used within this thesis.....	76
Table 2-2 Chemicals used within this thesis.....	77
Table 2-3 Buffers and solutions used within this thesis.....	78
Table 2-4 Laboratory materials used within this thesis.....	79
Table 2-5 Special equipment used within this thesis.....	80
Table 2-6. Bacterial samples and plasmids used within this thesis.....	81
Table 2-7 Magnification settings used for recording of data sets.....	82
Table 2-8 Magnifications errors for magnifications from Table 2-7.....	82
Table 2-9. Effective magnifications resulting from Table 2 7.....	83

List of Abbreviations

2D	Two-dimensional
3D	Three-dimensional
Å	Angstrom ($1\text{Å} = 10^{-10}\text{ m}$)
ACo	Acetyl Coenzyme A
ART	Algebraic Reconstruction Technique
CCC	Cross Correlation Coefficient
CCD	Charge Coupled Device
CPU	Central Processing Unit
cryo-EM	Cryogenic Electron Microscopy
DFT	Discrete Fourier Transformation
FFT	Discrete Fast Fourier Transformation
FSC	Fourier Shell Correlation
GPU	Graphical Processing Unit
HAC	Hierarchical Ascending Classification
HPC	High Performance Computing
ICA	Independent Component Analysis
MPI	Message Passing Interface
MRA	Multi Reference Alignment
MSA	Multivariate Statistical Analysis
NA	Numerical Aperture
OTF	Optical Transfer Function
OTR	Orthogonal Tilt Reconstruction
PCA	Principal Component Analysis
PCTF	Phase-Contrast Transfer Function
PSF	Point Spread Function
RCT	Random Conical Tilt
SIMD	Single Instruction Multiple Data
SIMT	Single Instruction Multiple Threads
SIRT	Simultaneous Iterative Reconstruction Technique
SISD	Single Instruction Single Data
TEM	Transmission Electron Microscopy

ABSTRACT

New computational methods for 3D structure determination of macromolecular complexes by single particle cryo-Electron Microscopy

In cryo-electron microscopy (cryo-EM) single-particle reconstruction, projection images of many first order structural identical copies of the specimen of interest are combined to recover the underlying three-dimensional object. The analyzed particles are embedded in vitreous ice in a hydrated state at many random orientations and projection images are recorded using a transmission electron microscope (TEM). The heterogeneity of two-dimensional projection image data resulting from the co existence of different conformational or ligand binding states of a macromolecular complex remains a major obstacle as it impairs the validity of reconstructed density maps and limits the progress towards higher resolution. Nevertheless, single particle cryo-EM is the method of choice for structure determination of large macromolecular complexes that are difficult to purify in the amounts and quality needed for X-ray crystallization. In contrast to other structure determining techniques, single particle cryo-EM is not an ensemble technique. Images of individual macromolecular complexes are recorded that can potentially be used to detect structural variations within a single dataset which is highly important for structure determination of large and dynamic macromolecular assemblies. However, computational tools to sort large datasets of images into subpopulations representing images that belong to a unique 3D object are still missing. In structural analysis of macromolecular assemblies with a high degree of structural dynamics, separation of conformations is a challenging task because for each particle image there are six degrees of freedom (translations and rotations), an unknown number of conformations and a high level of noise that have to be considered simultaneously. Classical random conical tilt reconstruction, utilizing additional experimental information by recording of tilted image pairs generates single class sum starting models, limited by a missing cone of information and a low Signal to Noise ratio originated at the limited number of class members and thus projection views used for reconstruction. A new method is presented, based on acquisition of tilted image pairs under cryo conditions facilitating classification of both untilted and tilted raw images. In these double-classified tilted pairs in combination with their experimental tilt angular relationships of the classified particles, angular relationships relative to each other are conserved. This information can be utilized to compute multi class sum starting models without a missing cone. Additionally, the information obtained by classification and tilt relationships can be used to separate particles in different conformations into individual models. The novel strategy is intended to gain insight into the 3D structures and structural diversity of so far poorly characterized dynamic assemblies. Increased computational demands, originated at the increased number of projection images to process in order to analyze conformational differences, are addressed and strategies to overcome these using recent developments in information technology such as Multicore-, Parallel- and GPU- processing are presented. Each parallel processing paradigm alone can improve overall performance, while combining all paradigms, unleashes the full power of today's technology. The increased computational performance thus makes certain applications feasible that were virtually impossible before.

ACKNOWLEDGEMENTS

I would like to express sincere appreciation to my thesis committee: Professor Dr. Ralf Ficner, Professor Dr. Erwin Neher and Professor Dr. Holger Stark. Thanks for giving me the opportunity to be part in this interesting research and thanks for your guidance and inspiration. In addition, I would like to thank Burkhard Heisen in special and also Niels Fischer, Florian Hauer, Björn Sander, Prakash Dube and Dietmar Riedel for interesting and valuable discussions. Further thanks go to Professor Dr. Klaus Weber for immeasurable biochemical experience and Kathy Gelato for native English skills. I thank Tobias Koske, Karl-Heinz Knauber and Mario Lüttich for hardware and software support and the fulfillment of my sometimes extraordinary demands and ideas. Thanks also go to Gordon Freeman, Percival Cox, John Dorian and Christopher Turk for interdisciplinary discussions. I would also like to thank all members of the Stark, Riedel and Lührmann labs for providing biochemical assistance, courtesy in many ways and their pleasant company. Last but not least I would like to thank my dog Bonzo for bearing company and keeping my feet warm during the writing of this thesis as well as the rest of my family who made it possible for me to present this work.

1 Introduction

If you want to understand function, study structure.

(Crick 1988)

Structure without function is a corpse, function without structure is a ghost.

(Vogel and Wainwright 1969)

To understand biological processes apart from the functional analysis, the determination of the structure of proteins and macromolecular complexes is a key issue. There are several well established methods for the determination of protein structures.

1.1 Methods for structure determination of macromolecular assemblies

1.1.1 Single particle electron microscopy

Especially for structure determination of large, possibly asymmetric and biochemical and or conformational homogeneous complexes that are difficult to purify in the amounts and quality needed for X-ray crystallization, single particle electron microscopy is the method of choice (Frank 1996; Frank 2002; van Heel 2002; Stark and Luhrmann 2006; Leschziner and Nogales 2007). It is not an ensemble technique and it does not rely on the formation of protein crystals. The only prerequisite is the presence of a sample containing the purified protein of interest in a moderate concentration. Today this method routinely delivers three-dimensional structures of macromolecular complexes at 4-20 Angstrom resolution. Even for large, asymmetric macromolecular complexes, a visualization of e.g. α -helices (Golas, Sander et al. 2003), conformational changes upon ligand binding (Golas, Sander et al. 2005) or tRNAs bound to translating ribosome (Stark, Orlova et al. 1997) can thus be realized. The instrument used, a transmission electron microscope (TEM), delivers two-dimensional projection images of macromolecular assemblies. Many structurally identical copies, in first order congruent in three dimensions, exist in the specimen analyzed. The three-dimensional structure of an object can be reconstructed from a series of two-dimensional projections along different directions. The mathematical theory for determining a function from its projections was originally derived by Radon (Radon 1917) leading to the development of several reconstruction algorithms used in e.g. tomography and electron microscopy, as reviewed in (Budinger, Gullberg et al. 1979). In electron microscopy, bright field weak phase contrast images are projections of the specimen oriented randomly within the sample, resulting in different projection directions. A series of micrographs can thus be used for a

three-dimensional reconstruction (DeRosier and Klug 1968) if the projection directions of individual projection images can be identified.

1.1.2 Crystallographic methods

Although arguably the best standard method for structure determination at atomic resolution is X-Ray crystallography, it still depends on the crystallization of the protein to study. Not only crystallization but also data analysis is impeded if the protein studied is either flexible or undergoes biochemical or conformational changes. In these cases if a crystal can be formed at all, the analysis of diffraction patterns makes the intensities and thus the waves' amplitudes accessible but not the waves' phases. Another crystallographic method is electron crystallography which depends on the existence of two-dimensional protein crystals. These can be analyzed using an electron microscope. In diffraction mode, diffraction patterns that can be recorded as in X-Ray Crystallography represent the amplitudes of the diffracted electron waves. The phases can be accessed by using the electron microscope in imaging mode. The information can be combined for structure determination, thus solving the phasing problem for electron microscopy, but the formation of a two-dimensional crystal is still necessary.

1.2 Fundamentals of light microscopy

There are several similarities between light microscopy and transmission electron microscopy. Therefore, fundamentals of light microscopy are introduced first. Due to the wave-particle duality, depending on the problem analyzed, either geometric or wave optics can be used for

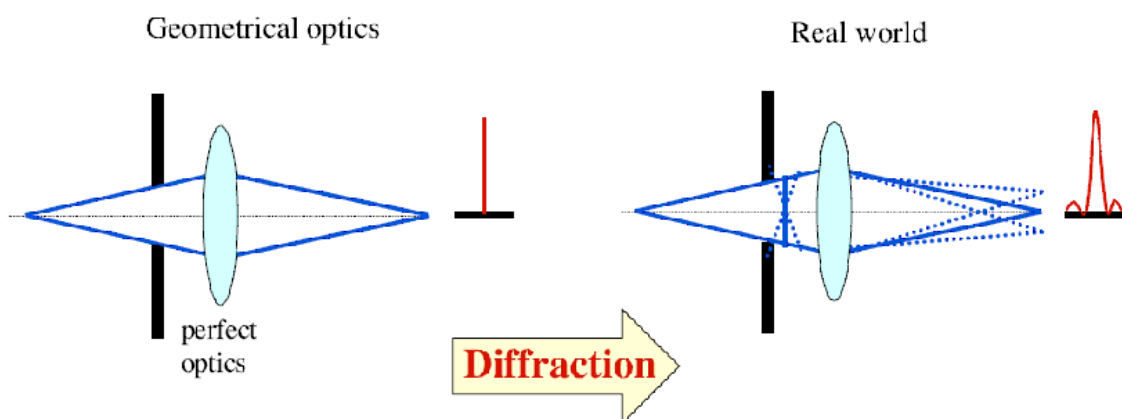


Figure 1-1 The image produced when imaging a point like object is the so called point spread function (PSF). Due to diffraction a blurring occurs in reality.

description in light microscopy. Geometrical optics describes the propagation of light, ignoring the wave nature of light, as illustrated in the left image of Figure 1-1.

In reality, a vast number of factors are responsible for the variations of the dimension and geometry of the image of a point light object produced by an optical system (Abbe 1873). First of all, the influence of diffraction is analyzed.

The point spread function (PSF) describes the image produced when imaging a point-like object as shown in the right image of Figure 1-1. As a microscope is a linear spatial invariant optical system, its imaging properties are completely defined by its PSF.

$$b(\vec{r}) = o(\vec{r}) \otimes h(\vec{r}) = \int o(\vec{r}') \cdot h(\vec{r} - \vec{r}') d\vec{r}'$$

Equation 1-1

In case of incoherent image generation, the image $b(\vec{r})$ produced by a linear spatial invariant system is given by the convolution of the object function $o(\vec{r})$ and the intensity PSF $h(\vec{r})$ as illustrated in Figure 1-2.



Figure 1-2 The convolution of an object in this case the capital letter E and an aberrated PSF in this case the PSF of a human eye. Figure modified from (Yoon, Jeong et al. 2004)

The PSF for a lens of lower opening angle is the Airy disc, which is the Fraunhofer diffraction pattern for a circular pupil as shown in Figure 1-3. In an ideal system it only depends on the diameter d of the pupil (Figure 1-4) which is illustrated in Figure 1-4.



Figure 1-3 The PSF for a perfect optical system is the Airy disc, which is the Fraunhofer diffraction pattern for a circular pupil.

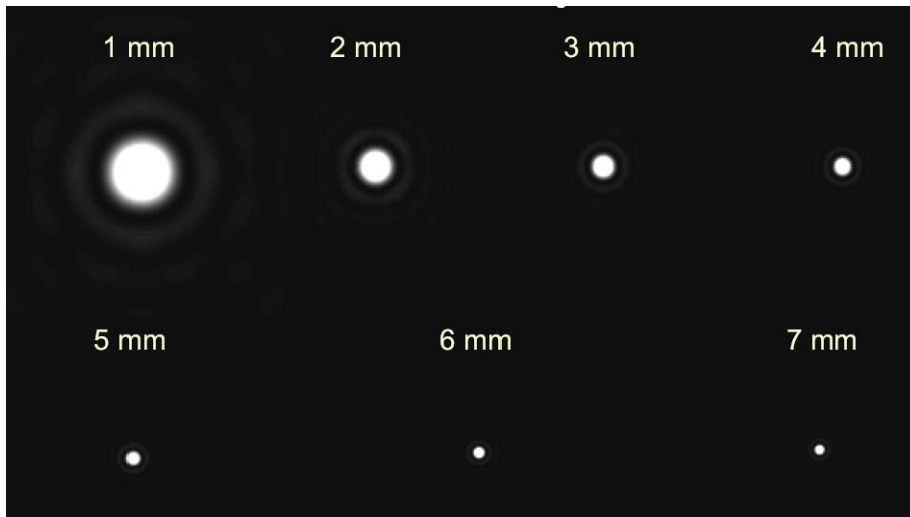


Figure 1-4 Airy disks for different pupil diameters d .

In reality there is no ideal optical system. In reality there are imperfections in the optics that influence the behavior of the PSF. When imaging with an aberrated PSF, the image will be aberrated. An example is given in Figure 1-5.

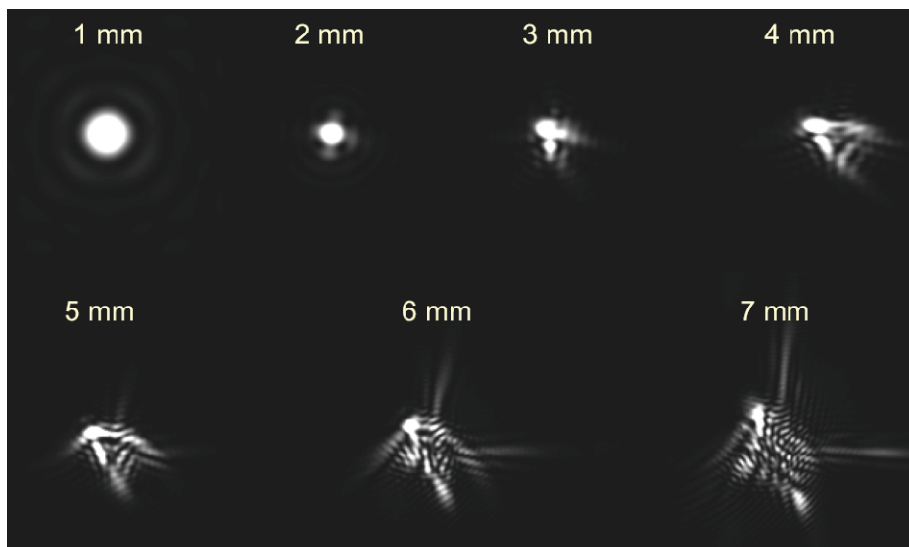


Figure 1-5 The PSF of a typical human eye depending on the present pupil diameter. This corresponds to the present adjustment of the iris. Figure modified from (Yoon, Jeong et al. 2004).

1.2.1 Optical transfer function

Apart from the PSF, the optical transfer function (OTF) is often used to characterize the properties of an optical system. The image generated by the system is given by the convolution between the object and the PSF like shown in Figure 1-2. The frequency spectrum of the

image $F(b(\vec{r}))$ is given by the product of the object's frequency spectrum and the Fourier transform of the PSF $F(h(\vec{r}))$ which is called OTF.

$$F(b(\vec{r})) = F(o(\vec{r}) \otimes h(\vec{r})) = F(o(\vec{r})) \cdot F(h(\vec{r}))$$

Equation 1-2

Therefore the OTF represents the spectrum of spatial frequencies that are transmitted by the system.

If the OTF is zero or nearly zero for some spatial frequencies, these frequencies are barely transmitted. This means that details of the object which lie in this spatial frequency range cannot be resolved. The OTF can be interpreted as a measure of the reduction of contrast from object to image which is illustrated in Figure 1-6. Contrast is the difference in intensity for two different objects.

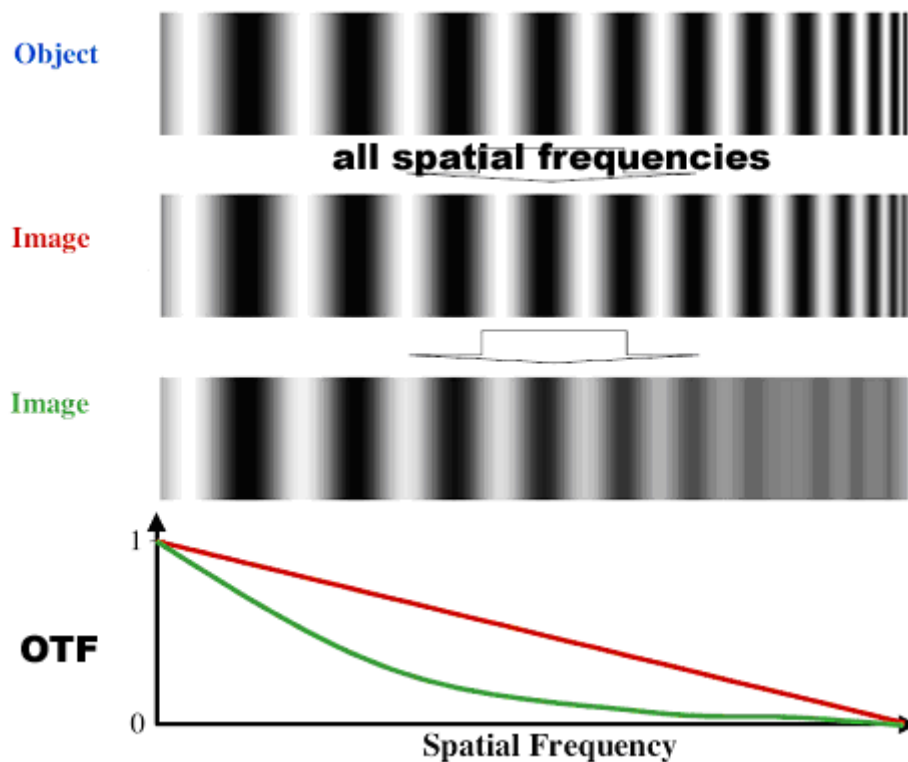


Figure 1-6 The transfer of spatial frequencies through an optical system is described by the OTF. Frequencies where the OTF equals zero cannot be transmitted. Structures in this spatial frequency range cannot be resolved.

1.2.2 Resolution

A reasonable definition of resolution describes the constraints necessary to distinguish an object from its neighboring object. Figure 1-7 shows an illustration of the Rayleigh-criterion which states that two objects can be discerned when the maximum of the diffracted image of one object correlates with the first minimum of the diffracted image of *the other object*.

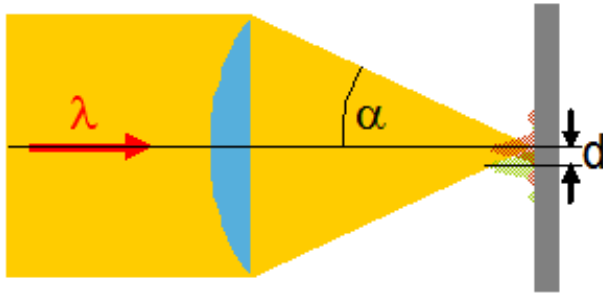


Figure 1-7 Visualization of the Rayleigh criterion for resolution.

This is fulfilled when the object to neighbor distance d is:

$$d \geq 0.61 \frac{\lambda}{n \sin \alpha}$$

Equation 1-3

where λ is the wavelength of the light used, n the refractive index and α , the half cone of opening angle of the objective used. The denominator $n \sin \alpha$ in Equation 1-3 is called numerical aperture (NA). Resolution of a light microscope is limited by the wave length of the light used as shown in equation 1.3 due to diffraction. This limits the light microscopes resolution to a resolution of ≈ 200 nm. Although methods have been developed recently, circumventing this limitation in the case of laser fluorescence microscopy e.g. in (Denk, Strickler et al. 1990; Klar, Jakobs et al. 2000), these methods rely on fluorescent dyes, possibly in combination with antibodies for image generation. The dimension of these dyes chromophores alone lies in the magnitude of proteins, feasible for studies of e.g. cell organelles. The study of protein structures yet is still unpromising using these techniques.

1.3 Electron microscopy

In electron microscopy, instead of photons, electrons are used for imaging. The electron wavelength depends on the particle velocity and thus the acceleration voltage applied and is much smaller than the wavelength of light. Electrons are focused by electromagnetic fields used to form electron lenses. These features combined result in the property that electron microscopy is limited due to the construction of the electron microscope imaging system, not due to a limitation by diffraction in contrast to light microscopy. The properties of electrons and electron optics are now introduced in detail.

1.3.1 Electron properties

Charged particles or point charges experience the so called Lorentz force:

$$\vec{F}_{Lorentz} = q(-\vec{\nabla}\phi - \frac{\partial\vec{A}}{\partial t} + \vec{v} \times (\vec{\nabla} \times \vec{A}))$$

where

$$\vec{E} = -\vec{\nabla}\phi - \frac{\partial\vec{A}}{\partial t}$$

and

$$\vec{B} = \vec{\nabla} \times \vec{A}$$

and therefore

$$\vec{F}_{Lorentz} = q[\vec{E} + (\vec{v} \times \vec{B})]$$

Equation 1-4

In the presence of electromagnetic fields, where q is the charge, \vec{E} is the electrical field vector, \vec{v} is the velocity vector of the charge and \vec{B} is the magnetic field vector. The lens effect of an axially symmetrical electric field as well as that of a rotational symmetric magnetic field can be derived from Equation 1-4. In case of an axially symmetrical electric field, the equipotential surfaces are figures of revolution. They intersect the axis at right angles, and in the neighborhood of their vertex they are approximately spherical. If the space between these surfaces is imagined filled with a medium of a refractive index proportional to the field strength, a succession of lenses is obtained, somewhat distorted outside, but of the correct shape near the axis. As a combination of aligned lenses is again a lens, the imaging effect of the electric field is immediately evident. The explanation of the magnetic type of

lens is somewhat more complicated. The Lorentz force exerted by a magnetic field on a moving electron is at right angles both to the direction of the field and to the direction of motion. The effect is a twisting or equipotential surfaces rotation of the electron trajectories around the axis, an effect which has no counterpart in ordinary optics. The magnetic vector potential \vec{A} is zero at the axis and increases approximately linearly with the radius r . This means that the equivalent potential decreases outside the axis and that the magnetic field has a repellent effect, i.e., it drives the electrons back, toward the axis. Therefore, a magnetic lens is always a condensing lens. Of the numerous defects which lenses can have, only three are of interest in microscopy: the spherical aberration, the chromatic aberration, and the axial coma. Spherical aberration, the most important of the lens defects in electron microscopy, means that an axial point is imaged as a point strictly speaking only while the imaging rays are infinitesimally close to the axis. These are called paraxial rays, and their intersection with the axis is the paraxial or Gaussian image. At larger angles α , the intersection moves away from the Gaussian point by a distance which is called the longitudinal spherical aberration, and which in first approximation is proportional to α^2 . A point will be imaged as a disk of a diameter proportional to α^3 . This diameter is called the transversal spherical aberration. These characteristics can be applied to use electrons in an imaging system comparable to light microscopy (Ruska and Knoll 1931) and was used by Ernst Ruska in Berlin in 1931 to build the first electron microscope (Knoll and Ruska 1932). Starting with a 17-fold magnification, the electron microscope potential has been constantly increased and nowadays delivers resolutions ~ 0.5 Angstrom in Transmission mode. Due to the electrons much smaller wavelength, in EM a much better resolution than in light microscopy can be achieved. The electron wavelength λ depends on the acceleration voltage used following De-Broglie equation:

$$\lambda = \frac{h}{mv}$$

Equation 1-5

where h is Planck's constant, m the mass and v the particles velocity. For an electron this leads to:

$$\lambda = \frac{1.225}{U_0(1 + 0.98 \cdot 10^{-6}U_0)} [nm]$$

Equation 1-6

where U_0 is the electron microscopes acceleration voltage in Volt. The electrons' relativistic mass increase:

$$m(v) = \frac{m_0}{\sqrt{1 - \frac{v^2}{c^2}}}$$

Equation 1-7

is already taken into account in Equation 1-6

Following Equation 1-6 the electron wavelength for typical acceleration voltages in the range of 100-400 kV is approximately 100,000 fold smaller than the wavelength of visible light, which lies in the range of 380-780 nm. Although due to the construction of the electron microscope imaging system, not due to a limitation by diffraction, the resolution limit of the electron microscope is only 1000-fold higher than the resolution of a light microscope and can be expressed by:

$$d_{min} = 0.6 \sqrt[4]{C_S \lambda_e^3}$$

Equation 1-8

where d again is the object to neighbor distance in the object plane, λ_e the electrons' used wavelength and C_S the spherical aberration coefficient of the electron microscope objective. Spherical aberration in electron microscopy is an image defect similar to spherical aberration in light microscopy (see Figure 1-8), resulting from the fact that real lenses - light-optical and magnetically - diffraction power varies with the distance to their axis, resulting in varying focal lengths, depending on the distance to the axis. An object point will therefore not be imaged as a point but as a disc. Spherical aberration coefficient is therefore also called opening error.

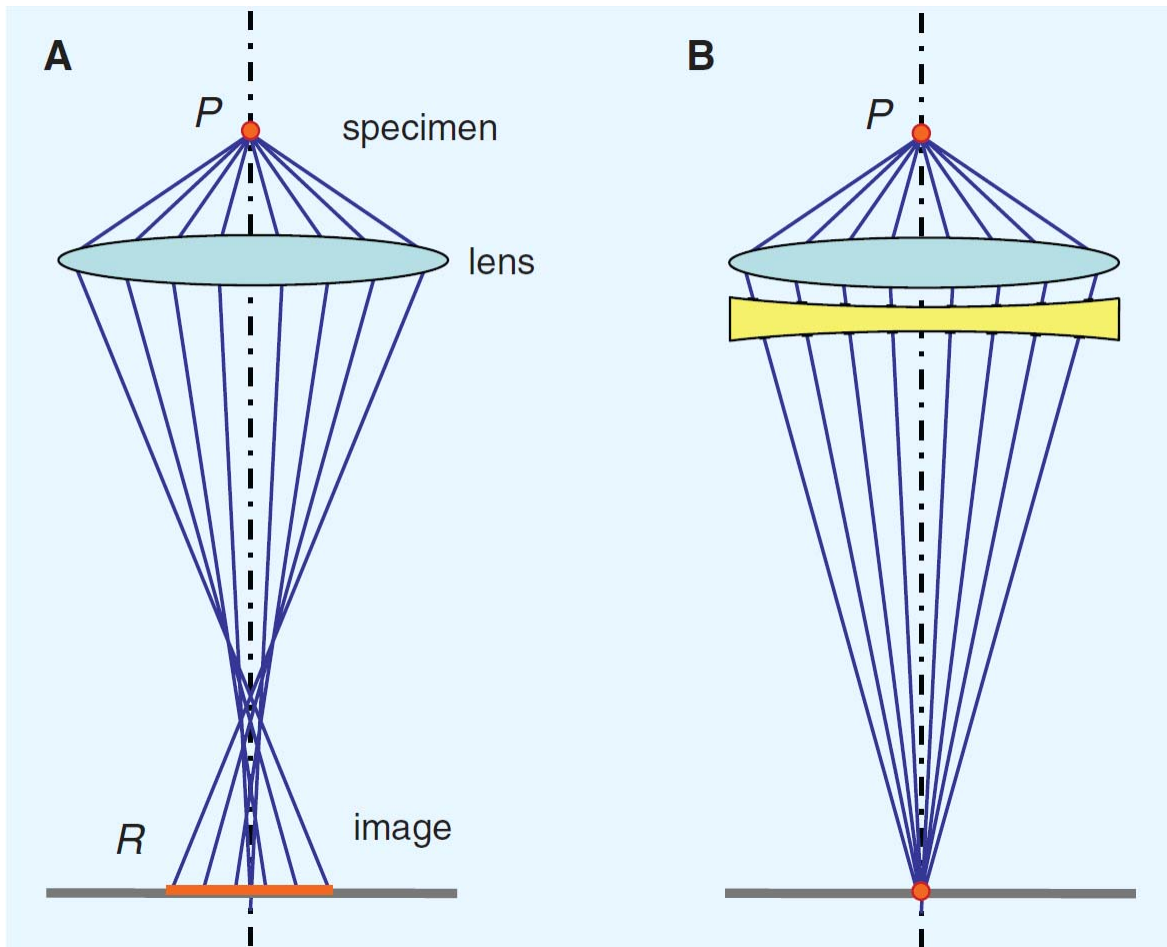


Figure 1-8 In light optics, spherical aberration can be corrected for by combining the converging lens with a suitable diverging lens.

1.3.2 Electron optics

Accelerated electrons scattered by the object generate image contrast by scattering absorption, treating electrons as particles for the description. When imaging thin objects with high resolution, phase contrast which can only be described by wave theory is the major effect. Scherzer has proved the important theorem that in rotational symmetric electron lenses, whether electrostatic, magnetic, or combined, the spherical aberration can never be eliminated as long as there are no space charges or currents in the space traversed by electrons (Scherzer 1936). There are other technique for realization of diverging lenses and thus correction for spherical and chromatic aberration. Diverging lenses can be realized by time-dependent lens fields (Scherzer 1947), mirror elements (Haider, Uhlemann et al. 1998), or the combination of multiple multipole lenses (Rose and Preikszas 1995; Rempfer, Desloge et al. 1997). Technically, all ways are very demanding and it was only very recently that the spherical aberration was successfully reduced by multipole elements.

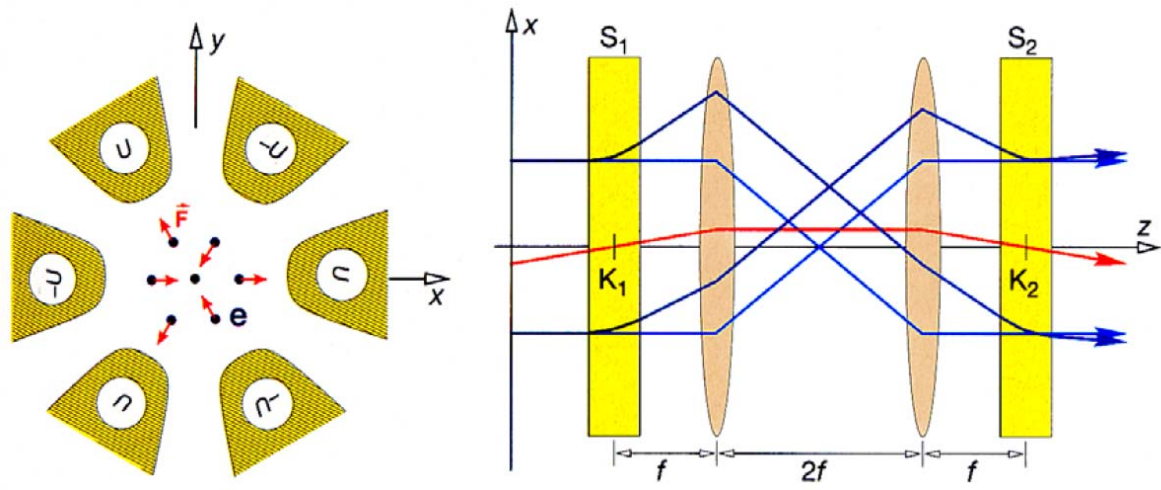


Figure 1-9 Spherical aberration correction in electron optics. A combination of 2 diverging hexapole lenses (left) arranged in a design depicted on the right, in combination with focusing lenses, where S1 and S2 are diverging hexapole lenses, can serve to correct for spherical aberrations. Figure modified from (Hawkes and Kasper 1996).

Additionally, it is known that even the worst lens approaches perfection, if its aperture is reduced to almost nothing. The high quality of electron microscopes with the spherical aberration not corrected for has been achieved by this simple artifice of using objectives with pinhole apertures or their equivalents. This is a line which light optics could never follow, as two phenomena would soon set a limit to it: diffraction at the aperture and insufficient light intensity. In electron optics, however, it was highly successful for two reasons. The first is the smallness of the diffraction effect, due to the extreme shortness of the de Broglie wavelength of the electrons; the second reason is that the intensities which can be realized in electron optics are enormously greater than those available in light optics. In today's Electron microscopes, all kinds of aberrations are corrected for thus not limiting the obtainable resolution.

1.3.3 The Fourier transform

Waves generated by a scattering object, propagating through a lens, project an image from the object plane into the focal plane. Wave fronts are plane after passing a lens and these plane waves of different directions are focused in the focal plane. Therefore, interference cannot occur in the focal plane. The resulting diffraction pattern in the focal plane is exactly the Fourier transform of the incident object waves. Therefore, microscopic images and the theory of microscopy can be described in Fourier space (Bracewell 1965). The unit of Fourier space is the so called spatial frequency which is – in analogy to the frequency defined as the reciprocal unit of time – defined as a reciprocal length or distance. Fourier transformation applied to image data (Champeny 1973) decomposes image information in the form of pixels into spatial frequencies. The image information is expressed as a linear

combination of periodic functions or harmonics, e.g. in a set of sine and cosine functions. Low spatial frequencies or Fourier coefficients represent coarse information like general shape and location. High spatial frequencies define fine signal or image details. For digital data, consisting of pixels, Discrete Fourier Transformation (DFT) can be applied. Its implementation for computing is termed Fast Fourier Transformation (FFT) (Walker 1991). The Nyquist criterion (Nyquist 1928; Pratt 1991) states that to adequately image the minimum resolvable distance between two objects, a minimum sampling frequency of 2 times is required. This means that for 2x sampling, 2 pixel units are required to adequately cover the distance d_{\min} . The sampling theorem (Nyquist 1928) states that a critical spatial frequency

$$f_c = \frac{1}{2}I$$

Equation 1-9

termed Nyquist frequency exists that band limits the maximum spatial frequency that may be represented within the interval I (Nyquist 1928). A sine curve for example represented by a sequence of alternating black and white pixels exhibits the critical Nyquist frequency. If a pixel of a data image corresponds to 1 Å, the high resolution information content of that image is principally limited to 2 Å. In the case of the discrete Fourier transform, real space data is represented as complex numbers. Every complex data point:

$$z = a[\cos(\theta) + i \sin(\theta)]$$

Equation 1-10

contains the phase and amplitude values of a wave function belonging to a discrete frequency. The real part can be described by a symmetrical cosine function, the imaginary part by an asymmetric sine function. Fourier transformation can thus describe any given symmetry in the input data in opposition to pure sine or cosine transformations. The Fourier transform requires data analyzed to be periodic which can be achieved by adequate padding or masking of the data to treat the upper left and the bottom right pixel as direct neighbors in the case of two-dimensional image data. However zero padding introduces so called Fourier artifacts that can be avoided by increasing the image frame by 30-50 % more than necessary or applying so called soft padding, a grateful increase or decrease from the last original images pixel value to the padding pixels usually zero value. Let x_0, \dots, x_{N-1} be the

input pixel values. The discrete one-dimensional Fourier transform is then defined by the following equation:

$$X_k = \sum_{n=0}^{N-1} x_n e^{-\frac{2\pi i}{N}nk} \quad k = 0, \dots, N - 1$$

Equation 1-11

where $e^{-\frac{2\pi i}{N}}$ is a primitive N 'th root of unity and the vectors $e^{-\frac{2\pi i}{N}nk}$ form an orthogonal basis over the set of N -dimensional complex vectors (Bronstein and Semendjajew 2004). In electron microscopic images the imaginary part of the input data is zero and therefore x_0, \dots, x_{N-1} are real numbers. Then the DFT obeys the symmetry:

$$X_k = X_{N-k}^*$$

Equation 1-12

where the star denotes complex conjugation and the subscripts are interpreted modulo N . The ordinary DFT computes the transform of a one-dimensional dataset, a sequence (or array) x_n that is a function of one discrete variable n . More generally, one can define the multidimensional DFT of a multidimensional array x_{n_1, n_2, \dots, n_d} that is a function of d discrete variables $n_l = 0, 1, \dots, N_l - 1$ for l in $1, 2, \dots, d$ in analogy to the one-dimensional case, the multidimensional Fourier transform can be expressed as:

$$X_{k_1, k_2, \dots, k_d} = \sum_{n_1=0}^{N_1-1} (\omega_{N_1}^{k_1 n_1} \sum_{n_2=0}^{N_2-1} (\omega_{N_2}^{k_2 n_2} \dots \sum_{n_d=0}^{N_d-1} \omega_{N_d}^{k_d n_d} \cdot x_{n_1, n_2, \dots, n_d}) \dots)$$

Equation 1-13

, where $\omega_{N_l} = e^{-\frac{2\pi i}{N_l}}$ and the d indices run from $k_l = 0, 1, \dots, N_l - 1$ (Bronstein and Semendjajew 2004).

The multidimensional DFT has a simple interpretation. Just as the one-dimensional DFT expresses the input x_n as a superposition of sinusoids, the multidimensional DFT expresses the input as a superposition of plane waves, or sinusoids oscillating along the direction $\frac{k}{N}$ in space and having amplitude X_k . Such a decomposition is of great importance for everything from digital image processing ($d = 2$) to solving partial differential equations in three dimensions ($d = 3$) by breaking the solution into plane waves.

Computationally, the multidimensional DFT is simply the composition of a sequence of one-dimensional DFTs along each dimension. For example, in the two-dimensional case x_{n_1, n_2} one can first compute the N_1 independent DFTs of the rows (i.e., along n_2) to form a new array y_{n_1, k_2} , and then compute the N_2 independent DFTs of y along the columns (along n_1) to form the final result X_{k_1, k_2} . Or, one can transform the columns and then the rows; the order is immaterial because the nested summations above commute (Bronstein and Semendjajew 2004).

Because of this, given a way to compute a one-dimensional DFT (e.g. an ordinary one-dimensional FFT algorithm) one immediately has a way to efficiently compute the multidimensional DFT. This is known as a row-column algorithm, although there are also intrinsically multidimensional FFT algorithms.

If the inputs x_{n_1, n_2, \dots, n_d} are real numbers, as they often are in practical applications, then the DFT outputs have a conjugate symmetry similar to the one-dimensional case above:

$X_{k_1, k_2, \dots, k_d} = X_{N_1 - k_1, N_2 - k_2, \dots, N_d - k_d}^*$, where the star denotes complex conjugation and the l -th subscript is interpreted modulo N_l (for $l = 1, 2, \dots, d$).

The squared amplitude of the Fourier transform is termed power spectrum and is equivalent to the optical diffraction pattern of the imaged object. Visualization of the power spectrum after shifting the Fourier transform by a full period results in a power spectral image with low spatial frequencies near the center and high spatial frequencies near the edge like in a true diffraction pattern. This is the case, because the human eye is sensitive for intensity differences and wave intensity is proportional to the squared wave amplitude.

1.3.4 Image formation

For image generation in an electron microscope, the beams' electrons have to interact with the object studied. To achieve intensity or amplitude contrast i.e. visual differences in adjacent image features, the interaction with the object has to change the incident electron wave amplitude. The simplest form of an interaction is blocking of electron transmission which results in a direct amplitude change but is of minor importance for transmission electron microscopy of biological samples. Stray amplitude contrast is generated by a scattering interaction with the object. This interaction can take place either with the objects atoms nuclei or electron shells. For image formation the coulomb interaction with the charged atomic nuclei is relevant, which is termed elastic scattering when no energy loss of

the beams' electrons occurs. An electron passing by the atomic nucleus undergoes a coulomb scattering where the coulomb forces strength, and thus scattering angle, depends on the distance to the nucleus the interaction takes place with and its atomic number Z , representing the nucleus charge. For high scattering angles, the electron will be deflected to hit the lens aperture and will not contribute to image intensity. The objects scattering power dispersion leads to intensity differences in the image, termed stray amplitude contrast. The image formed by beam electrons therefore contains the information about the objects atomic numbers distribution. Stray amplitude contrast accounts for 5-15 % of total contrast. The much more important mechanism for contrast generation is phase contrast.

1.3.5 Phase contrast

Phase contrast is a wave-optical phenomenon, well known in light microscopy. Transparent objects, with a refractive index different from that of the medium (for instance: thin glass fibers) are almost invisible if the objective is sharply focused on them; but they produce very strong contrast on defocusing, if the focal plane of the objective happens to coincide with the focal points or lines of the object. In other words, what the microscope will be able to see in such a case is not the object itself, but the disturbance caused by the object in the original, more-or-less plane wave-front. Very thin objects can act, at least partly, as regular refractors and retard electron waves by one quarter, or even one half wave without destroying their coherence. Phase contrast may occur upon elastic scattering of electrons by interaction with the specimen's electromagnetic field. The incoming wave is termed zero wave w_0 and can be described by the wave equation:

$$w_0 = a_0 \sin(\varphi_0)$$

Equation 1-14

Where a_0 are the wave amplitude and φ_0 the phase angle. When an interaction changing the zero wave takes place in the specimen, the emerging wave, termed the object wave w_1 can be described by the expression:

$$w_1 = a_0 \sin(\varphi_0 + \varphi_1)$$

Equation 1-15

in the elastic case where the amplitude is not changed, Equation 1-5 can be rewritten to:

$$w_1 = a_0 (\sin\varphi_0 \cos\varphi_1 + \cos\varphi_0 \sin\varphi_1)$$

Equation 1-16

For weak phase contrast objects like biological specimens, phase shifts are very small and thus $\cos\varphi_1 \approx 1$ and $\sin\varphi_1 \approx \varphi_1$ can be assumed. Therefore Equation 1-6 becomes:

$$w_1 = a_0 \sin \varphi_0 + a_0 \varphi_1 \cos \varphi_0$$

Equation 1-17

Equation 1-7 can be split up in two parts, the zero wave part w_0 and the diffraction wave part:

$$w_2 = a_0 \varphi_1 \cos \varphi_0$$

Equation 1-18

where $w_1 = w_0 + w_2$.

Electrons scattered by the specimen undergo a phase shift of $\frac{\pi}{2}$ in respect to the undiffracted zero beam. To detect this phase shift and utilize it for phase contrast formation, the diffracted wave has to be shifted another $\frac{n\pi}{2}$ to generate positive phase contrast or $-\frac{n\pi}{2}$ to generate negative phase contrast (see Figure 1-10). In light microscopy this transformation

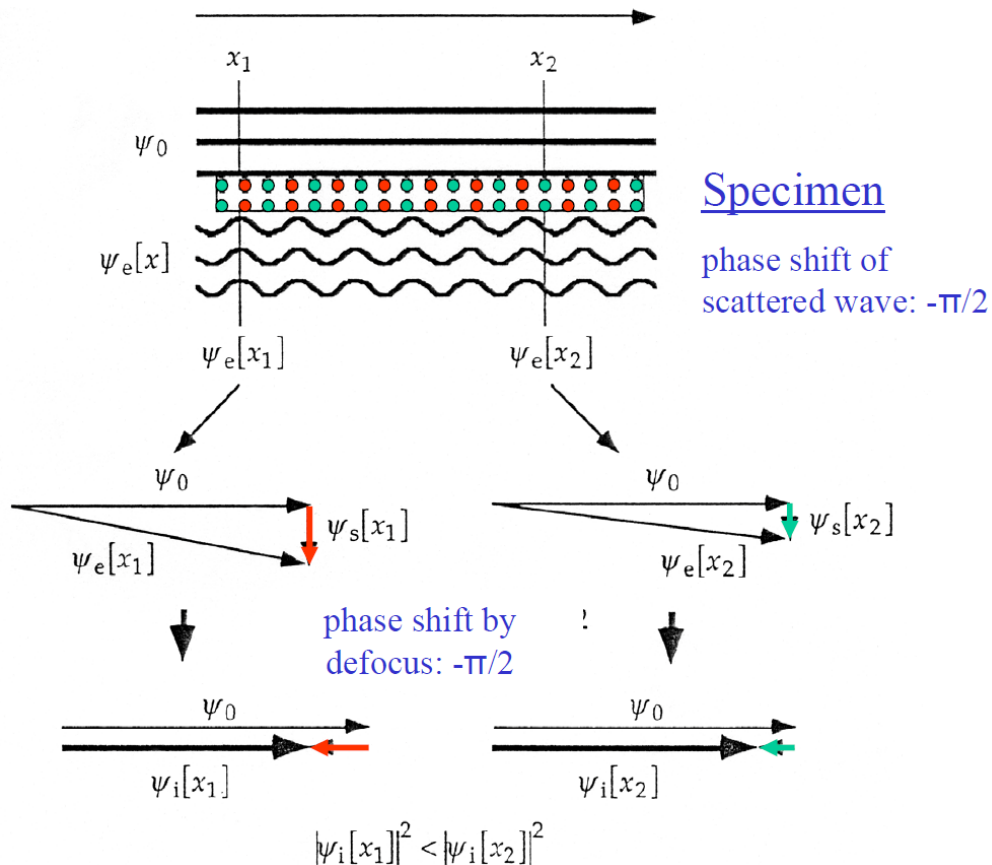


Figure 1-10 Illustration of transformation of phase contrast to amplitude contrast by defocusing.

of a phase difference into visible amplitude contrast is achieved by a ring like $\frac{\lambda}{4}$ or Zernike plate (Zernike 1942). In the last few years the use of carbon film for Zernike-type phase contrast in the TEM has led to an experimental solution in the form of a thin film with a hole in the center positioned in the back-focal plane of the objective lens (Danev and

Nagayama 2001). Several problems such as contamination and charging of the film and the complicated alignment procedure of the film lead to other technical solutions for obtaining phase contrast in TEM, in the form of an electric potential affecting the phases of electron waves which was first proposed by Boersch (Boersch 1947) and theoretically altered in a feasible way by Matsumoto and Tonomura (Matsumoto and Tonomura 1996). Recently two groups have succeeded to build such electrostatic phase plates in the form of an einzel lens (Majorovits, Barton et al. 2007) and a drift tube (Cambie, Downing et al. 2007), respectively, and have shown the first experimental proof of phase contrast mediated by an electric potential. One remaining problem with both published realizations of the electrostatic phase plate (Cambie, Downing et al. 2007; Majorovits, Barton et al. 2007) is the obstruction of electrons in the diffraction plane by structures that are necessary to form the correct, spatially confined electric fields. In case of the electrostatic einzel lens (Figure 1-11 A) such structures are the ring electrode of the lens itself and its supporting connectors. To avoid the obstruction, a novel electrostatic phase plate shown in Figure 1-11 B has been proposed (Schroder, Barton et al. 2007).

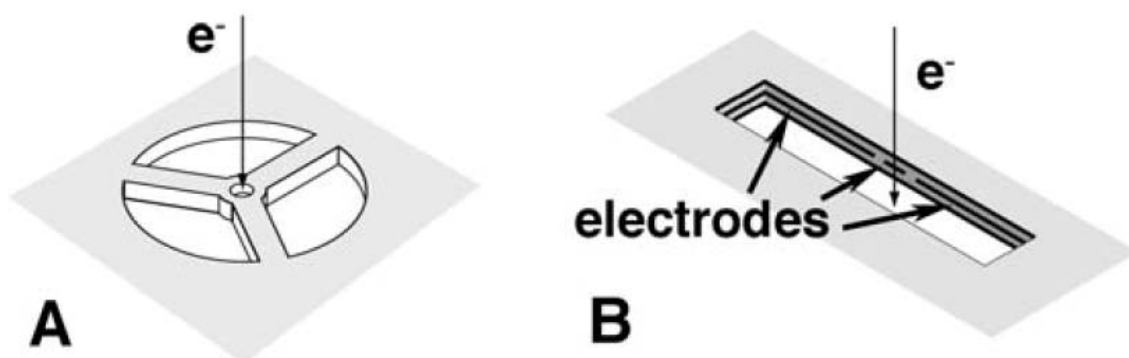


Figure 1-11 Zernike like phase plates in electron optics. In A) an Electrostatic einzel Lens phase plate as proposed by Boersch (Boersch 1947) is depicted. In B) an anamorphic phase plate for use in an aberration corrected TEM is depicted. Figure modified from (Schroder, Barton et al. 2007)

Instead of using special structures for confining the electric fields, a highly anisotropic field distribution, which is placed at an anamorphic image of the diffraction plane, i.e. in a plane where the diffraction image is compressed in one direction is proposed. The field shifts the phase of a thin stripe of the electron wave. By incorporating two phase plates, each of which is positioned at one of two crossed anamorphic diffraction planes, each phase plate shifts the phase by 45° for optimal phase contrast of a weak phase object (Schroder, Barton et al. 2007). All technical solutions for the generation of phase contrast in TEM are

still experimental. Currently, phase contrast is achieved by defocusing of the objective lens, introducing a deviation of the sample from the Gaussian focal plane.

As this effect is also dependant on the objective lenses spherical aberration constant C_S and the acceleration voltage of the electrons used for imaging, an optimum phase shift for all diffraction angles of the electron waves and therefore spatial frequencies cannot be achieved at the same time. As a result, only part of the spatial frequency components in the object exit wave are expressed in the image (Scherzer 1949). Maximum positive phase contrast is achieved at a very weak under focus of $\sqrt{C_S\lambda}$ which is termed Scherzer focus (Scherzer 1949). The phase contrast mechanism plays a major role in the high resolution observation of biological samples by transmission electron microscopy because biological samples are composed mainly of low atomic number elements (CHON) which makes them essentially transparent to high-energy electrons. The application of higher-acceleration voltages and techniques such as ice embedding worsens the contrast problem even further. Low spatial frequency components which are vital in biological observations are severely suppressed.

1.3.6 Phase-contrast-transmission function (PCTF)

The scattering of electrons by the central repulsive Coulomb force of nuclei leads to a hyperbolic trajectory and thus an angular deviation from the zero beam. This angular deviation is depending on the impact parameter b - the perpendicular distance from the center of the nucleus to the straight line path of the incoming electron - and its closest approach to the scattering nucleus - dependant on the electrons' kinetic energy and the scattering nuclei's atomic number and thus Coulomb potential. For scattered electrons focused by the magnetic field of the objective lens and small scattering angles this angular deviation generates a path difference $\Delta s(\theta, \lambda, b, Z)$. The spherical aberration of the objective lens can be described as a wave aberration function of angle $W(\theta)$. This can be rewritten to a function $W(\Delta s, \lambda, \theta, Z)$. In the Scherzer Formula (Scherzer 1949), Δs is expressed as a function of the spherical aberration C_S of the objective lens and the defocus Δz :

$$W(\theta) = \frac{2\pi}{\lambda} \Delta s$$

Equation 1-19

$$= \frac{\pi}{2\lambda} (C_S \theta^4 - 2\Delta z \theta^2)$$

Equation 1-20

this can be rewritten to a wave aberration function dependant on the spatial frequency $q = \frac{\theta}{\lambda}$ and the wave aberration $W(q)$ becomes:

$$W(q) = \frac{\pi}{2}(C_s\lambda^3q^4 - 2\Delta z\lambda q^2)$$

Equation 1-21

This equation can be used to derive the Phase Contrast Transfer Function $B(q)$:

$$B(q) = -2\sin W(q) = -2\sin\left[\frac{\pi}{2}(C_s\lambda^3q^4 - 2\Delta z\lambda q^2)\right]$$

Equation 1-22

As previously described, the introduction of phase shifts leads to changes in wave amplitudes and therefore generates contrast. The contrast in the image changes sinusoidally with varying phase shifts as described in the phase contrast transfer function (PCTF) (Reimer 1997). The PCTF at different defocus values is shown in Figure 1-12. It is zero at the origin and then increases slowly to its first maximum before it then alternates between positive and negative values. For high defocus values, the first zero crossing of the PCTF is reached at lower spatial frequencies than for low defocus values. Thus a high defocus leads to better transmission of low spatial frequencies but also to a shorter continuous and positive frequency band with more alternations. Spatial frequency regions where the PCTF equals zero contain no information. In regions where the PCTF is negative, the specimen information is transmitted in the form of negative phase contrast. If transferred information beyond the first zero point is discarded, the inverse of the spatial frequency of the first zero point is a distance and termed point resolution. Usually, the transfer bands for higher spatial frequencies can be utilized and by merging of data recorded at different defocus values allowing transfer gaps and zero crossings to be filled. This merging would extinguish the high resolution information contained in the alternating part of the PCTF by averaging. Therefore, the spatial frequency information for negative PCTF regions has to be inverted or flipped to be utilized for positive phase contrast information. An exponential decay of the PCTF can be observed with increasing spatial frequencies due to aberrations in the microscope, incoherence of the electron beam (Frank 1973; Wade and Frank 1977), mechanical instability of the sample holder in the microscope and modulation transfer functions of film materials and scanners (Sander, Golas et al. 2003a).

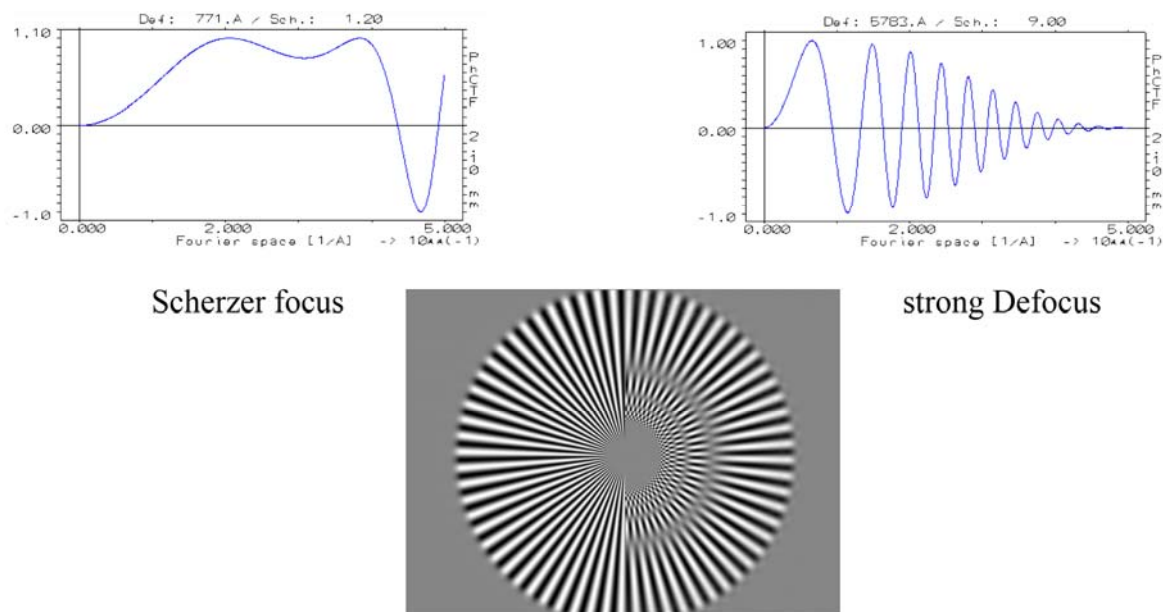


Figure 1-12 The PCTF at different defoci. At Schzerer focus (left), the transfer of high resolution information is brilliant but the low resolution contrast is insufficient to identify particles and distinguish them from noise. At a strong defocus setting (right) the contrast of low resolutions is good, particles can easily identified but the high resolution frequency bands are incomplete and PCTF is strongly decreasing for high frequency information. Figure modified from (van Heel 2008).

The influence of these various resolution-limiting factors can be summarized as an exponential factor e^{-Bq^2} , where B is the so called experimental B-factor (Glaeser and Downing 1992; Saad, Ludtke et al. 2001). In the bottom of Figure 1-12 the power spectra for Schzerer focus (left) and strong defocus (right) are shown, illustrating the decreasing transfer of high spatial frequencies. The rings visible in the power spectra are called Thon rings (Thon 1966) and represent phase reversals of the respective PCTF. The distance of the rings represents the maxima and minima of the corresponding PCTF in terms of spatial frequencies. By analyzing a recorded pictures power spectrum, the PCTF the image was generated with can be measured. In recorded pictures a radial symmetry of power spectra cannot be expected due to astigmatism. By measuring recorded power spectra and fitting them to theoretical power spectra of estimated PCTFs an automatic correction of images for PCTF by phase flipping is possible (Sander, Golas et al. 2003a). Additionally, power spectra and thus Thon rings can be used to rate image quality. Images of specimen areas containing no particles but only amorphous carbon support film or water surrounding particles produce an unspecific signal, modulated by PCTF. In case of specimen drift or charging, outer Thon rings representing high spatial frequency information are extinguished.

1.4 Single particle analysis

Single particle Electron Microscopy is the method of choice for structure determination of large macromolecular complexes that are difficult to purify in the amounts and quality needed for X-ray crystallization. In contrast to other structure determining techniques, single particle cryo-EM is not an ensemble technique. Images of individual macromolecular



Figure 1-13 A “biological macromolecule” in different conformations, here depicted by the amputated hand on some of the dinosaur models. The liquid sample and thus the specimen grid contain a plurality of particles in random orientations and possibly in multiple conformations. This cartoon-like model is used within this thesis for visualization of techniques and algorithms. It features all important properties of a real asymmetric particle. The model has a handedness and a broad spatial frequency range. The prongs on the back represent high spatial frequencies while the tail is a protruding feature, simplifying the recognition of overall orientation even at low resolution. Additionally, the model is not solid but has an internal structure that can be identified in projection views.

complexes are recorded that can potentially be used to detect structural variations within a single dataset that are highly important for structure determination of large and dynamic macromolecular assemblies.

Since the instrument used, a transmission electron microscope, records two-dimensional projection images of macromolecular complexes, computational methods have to be applied to reconstruct three-dimensional volumes from sets of two-dimensional projection images. In the ideal case of a large depth of field in combination with a magnification independent of the position within the imaged object, the TEM delivers “ideal”, geometrically correct 2D

projection images of thin 3D objects. Therefore, 3D-reconstruction aims at reversing the process of image formation and calculating the 3D volumes that generate the multiplicity of 2D projection images.

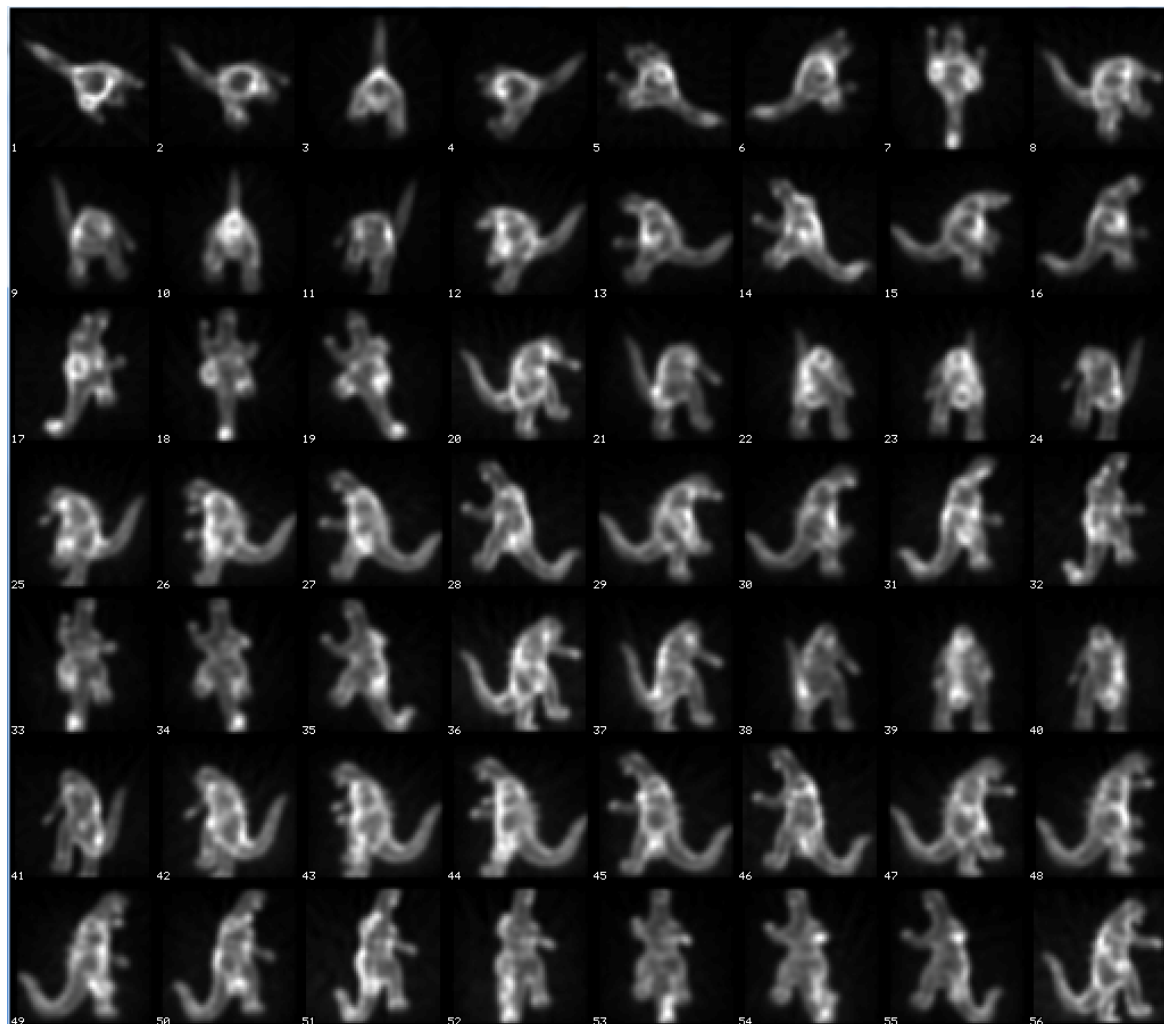


Figure 1-14 Projection views generated by “conformation 1”, the intact dinosaur, here depicted for noise-free imaging.

This is a challenging task because for each particle image there are six degrees of freedom (translations and rotations), an unknown number of conformations and a high level of noise that have to be considered simultaneously (see Figure 1-16). Figure 1-14 and Figure 1-15 show projection views of different “conformations” of the same “macromolecule”. These noise-free images already show that differences of 3D conformations are not easily detectable in 2D projection views and that their detectability furthermore differs with projection direction.

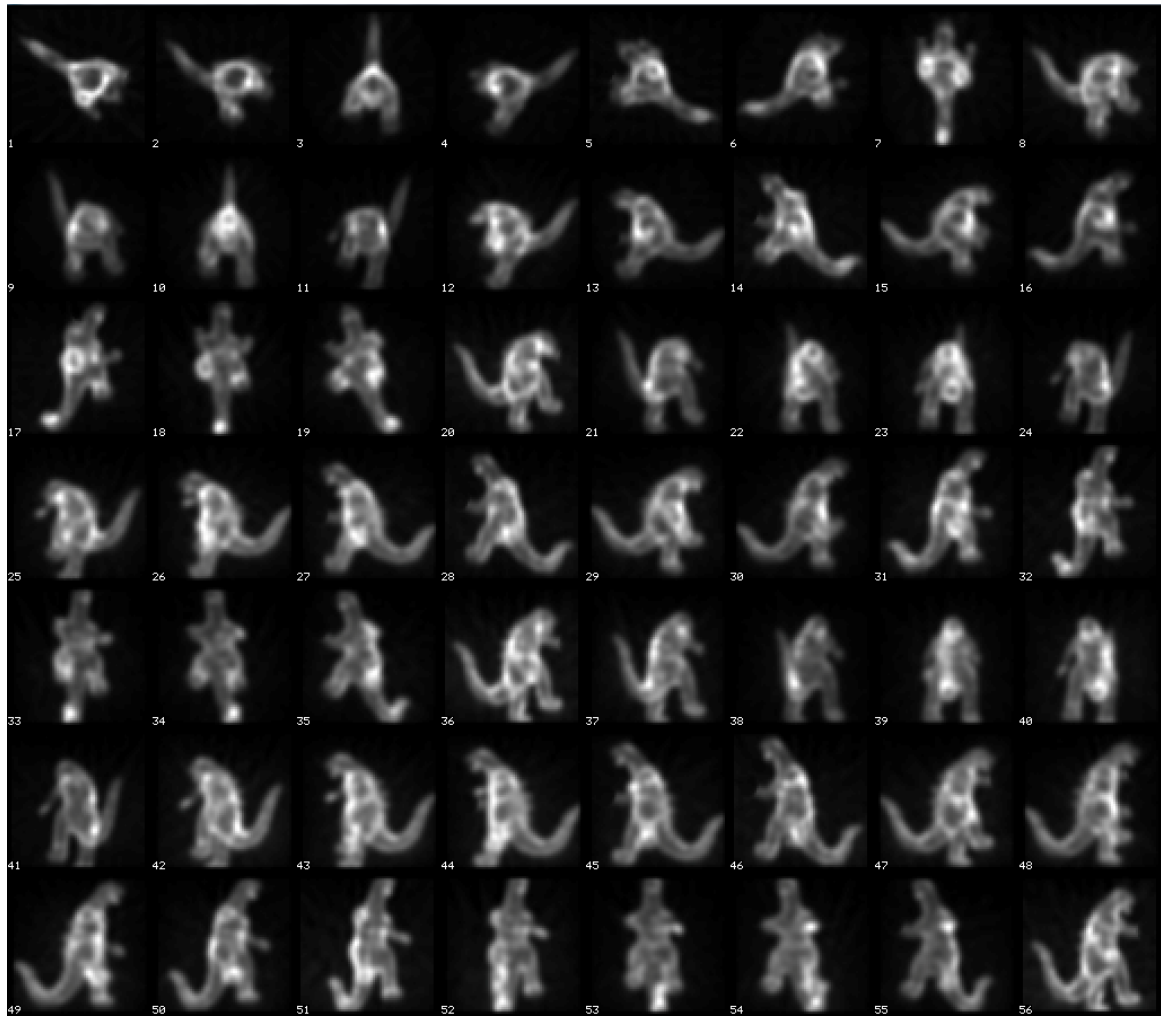


Figure 1-15 Projection views generated by “conformation 2”, the dinosaur with the amputated hand.

For 3D reconstruction, every 2D image’s projection direction in respect to the 3D object generating this view has to be identified. Assignment of projection directions to 2D views allows for back projection from 2D images to 3D volumes. Therefore the building blocks of all techniques for 3D image processing consist of identifying and aligning the particle views that are randomly distributed across the micrograph, sorting with respect to projection direction and back-projection of 2D projection views to 3D space.

This enables the main goal, the reconstruction of three-dimensional volumes from two-dimensional projection images by virtue of the random orientation of the macromolecules in the sample and thus different projection views of the same volume.

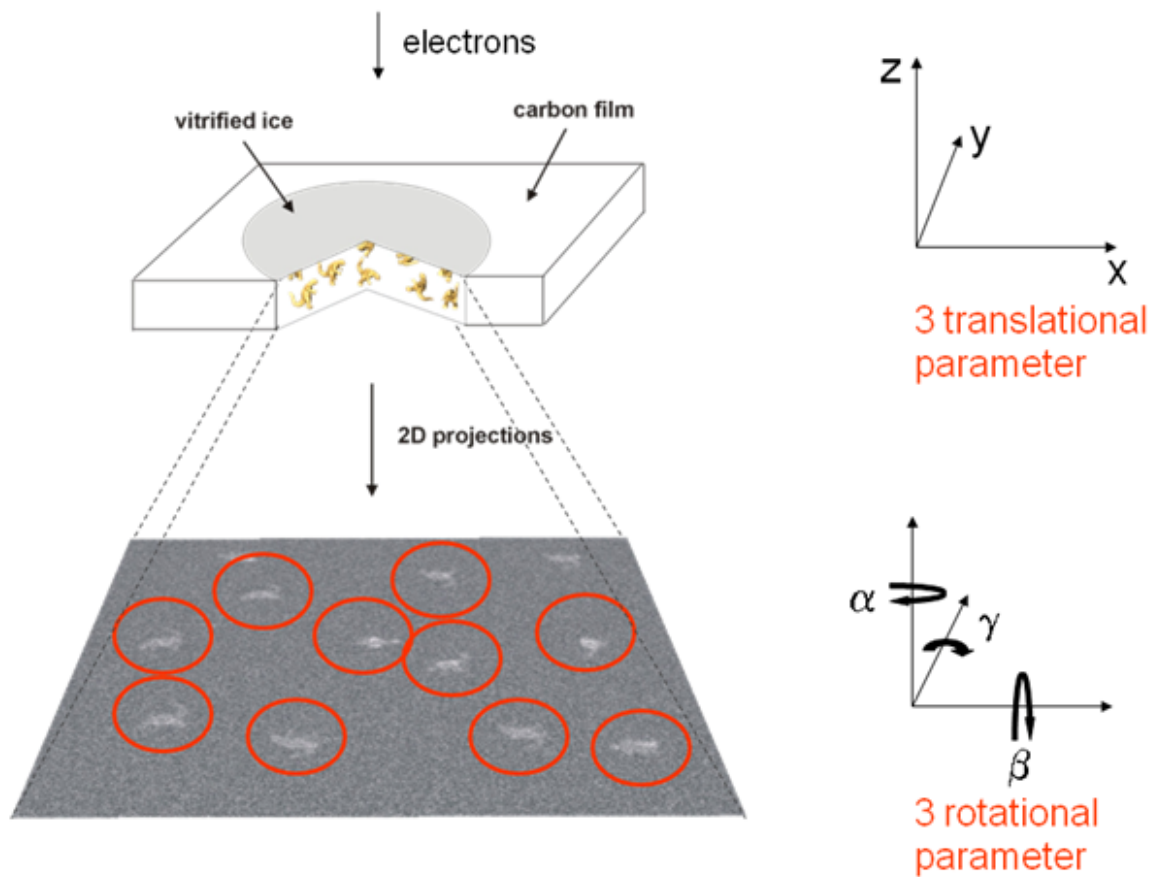


Figure 1-16 Particles in the specimen generated different projection views dependant on their random orientation, featuring six degrees of freedom.

Additionally, the signal to noise ratio of projection views can be improved by averaging of images sharing the same projection direction for back-projection in 3D space. Radiation sensitivity of biomolecules restricts imaging conditions to low electron doses (Stark, Zemlin et al. 1996). To avoid radiation damage, beam intensity is adjusted to a dose of maximally 20 electrons per \AA^2 , resulting in a poor signal to noise ratio of individual single projection views.

1.4.1 Image acquisition

TEM images, termed micrographs, can be recorded either on black and white film, based on silver halide technology, or by use of charged coupled device (CCD) detectors. In case of film recording, acquired micrographs have to be digitized by using professional high-resolution scanners to enable further digital image processing. Using this technique, the final digital high-resolution image depends on several parameters. These parameters are the sampling interval of the scanner, the modulation transfer function (MTF) of the scanner, describing an exponential decay of the original signal dependent on spatial frequency and the optical properties of the film. For a standard microscope magnification of 50,000x,

recording on film results in a pixel size on specimen level of 0.8-4 Å for a scanner sampling interval of 4-20 µm. Using the full film size of 8.3 x 10.2 cm facilitates the recording of large numbers of particles in a short time. Nowadays CCD detectors more and more replace black and white films, not only because the digitizing step can be abandoned. Performance of CCD detectors differs from film. Due to readout noise, low readout speed, and the small numbers of pixels, the speed and efficiency of data collection seems to be outperformed by photographic film – additionally, for very high resolution, photographic film is usually better than CCD detectors. Nevertheless, it has been shown that certain characteristics with respect to single-particle image processing have proven to contribute significantly to the correctness and accuracy of final 3D structures (Sander, Golas et al. 2005). The type of CCD camera used in electron microscopy is equipped with very efficient polycrystalline phosphor scintillators and cooled to approximately -30°C to minimize readout noise, offering a better signal to noise ratio (SNR) at low resolutions than film does (Booth, Jiang et al. 2004). Another important characteristic is the reliability of image phase transmission in case of low image contrast. By determining signal decay from power spectra of electron-microscopic images (Saad, Ludtke et al. 2001), the amplitude information is used to estimate the quality of signal transmission in terms of a B factor. Although the phase information is of great importance for digital image processing it is not possible to describe the quality of image phases for a given spatial frequency by the B factor (Sherman and Chiu 1997). Detailed analysis by Sander (Sander, Golas et al. 2005) show that especially in de-novo image processing – when particle details in the range of ~20 Å are to be revealed, CCD detectors outperform photographic film because the high spatial frequency noise recorded on film influences image processing and hinders enhancement of low-resolution particle characteristics.

1.4.2 Preparation of data sets for single particle analysis

Images recorded in a spot series using spot scan technique (Downing 1991) are combined (stitched) to form a large micrograph e.g. using TVIPS EM-MENU software (Tietz Video System, Gauting, Germany). Single particles are then selected from micrographs using e.g. the program BOXER from the EMAN suite (Ludtke, Baldwin et al. 1999). Boxer identifies particles within the spot scan images based upon correlation coefficient to a given, small number of reference densities. Selected particles are then visually inspected to guarantee sensitivity of the selection algorithm for all particle subsets and exclusion of artifacts not representing particle projection images like contaminants within the specimen, e.g. staining aggregates, ice and frozen ethane. Additionally, artifacts caused by the stitching procedure

and particles that are not fully imaged have to be excluded. Selected and verified particles are then extracted from the micrographs in the form of a set of small single images where the particle diameter is $\sim \frac{2}{3}$ of the total pixel frame.

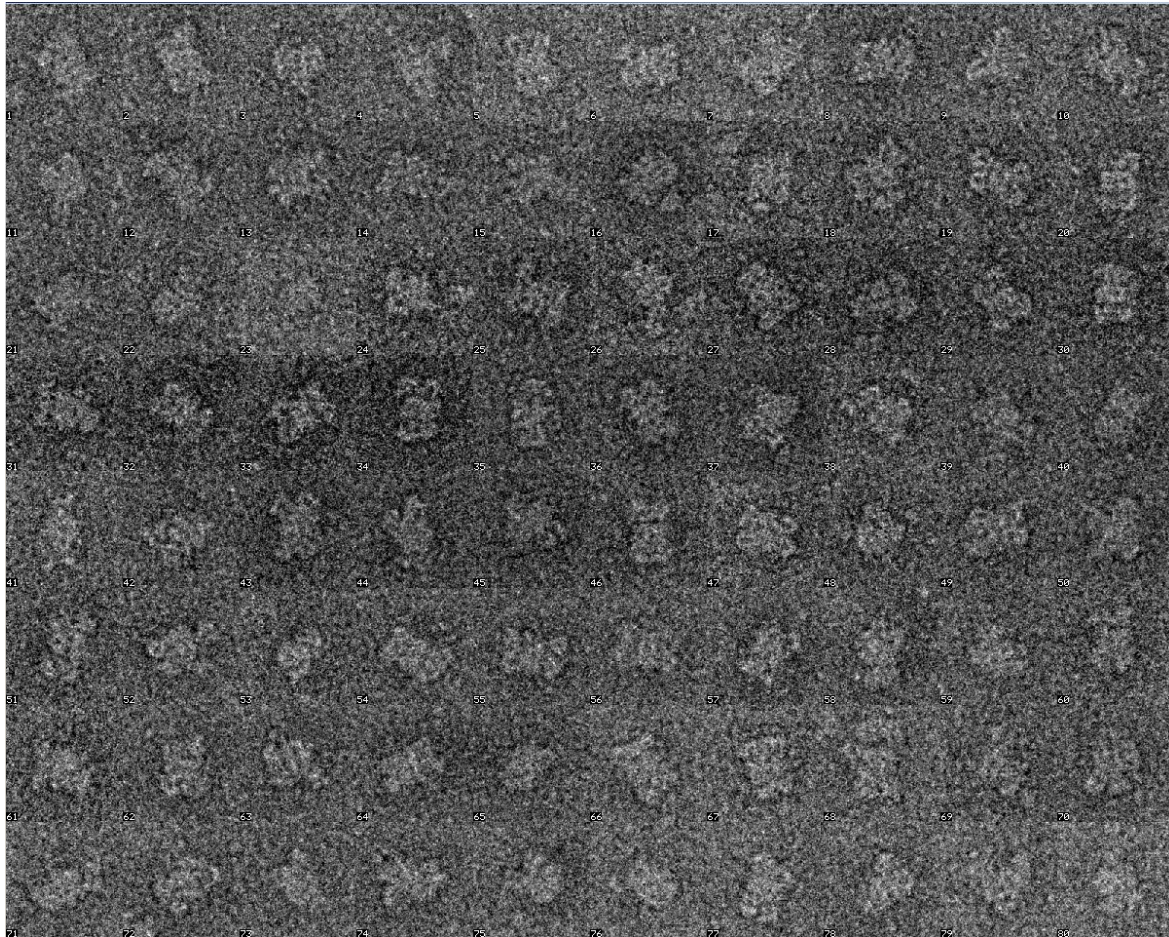


Figure 1-17 Typical example of raw data obtained by cutting out the particles out of the obtained micrographs. (In this case Acetyl CoA Carboxylase, prepared using the negative stain preparation technique.

Extracted particles are then prepared for further digital image processing. Image analysis in Fourier space requires band pass filtering of the extracted data sets. Very low spatial frequencies only representing image properties unrelated to the particle structure and very high spatial frequencies most sensitive to underlying noise are omitted. Additionally, a circular mask is applied thus reducing the information in the extracted square images to mostly particle information and rendering the information content less sensitive to image rotations, which is important for rotational alignment.

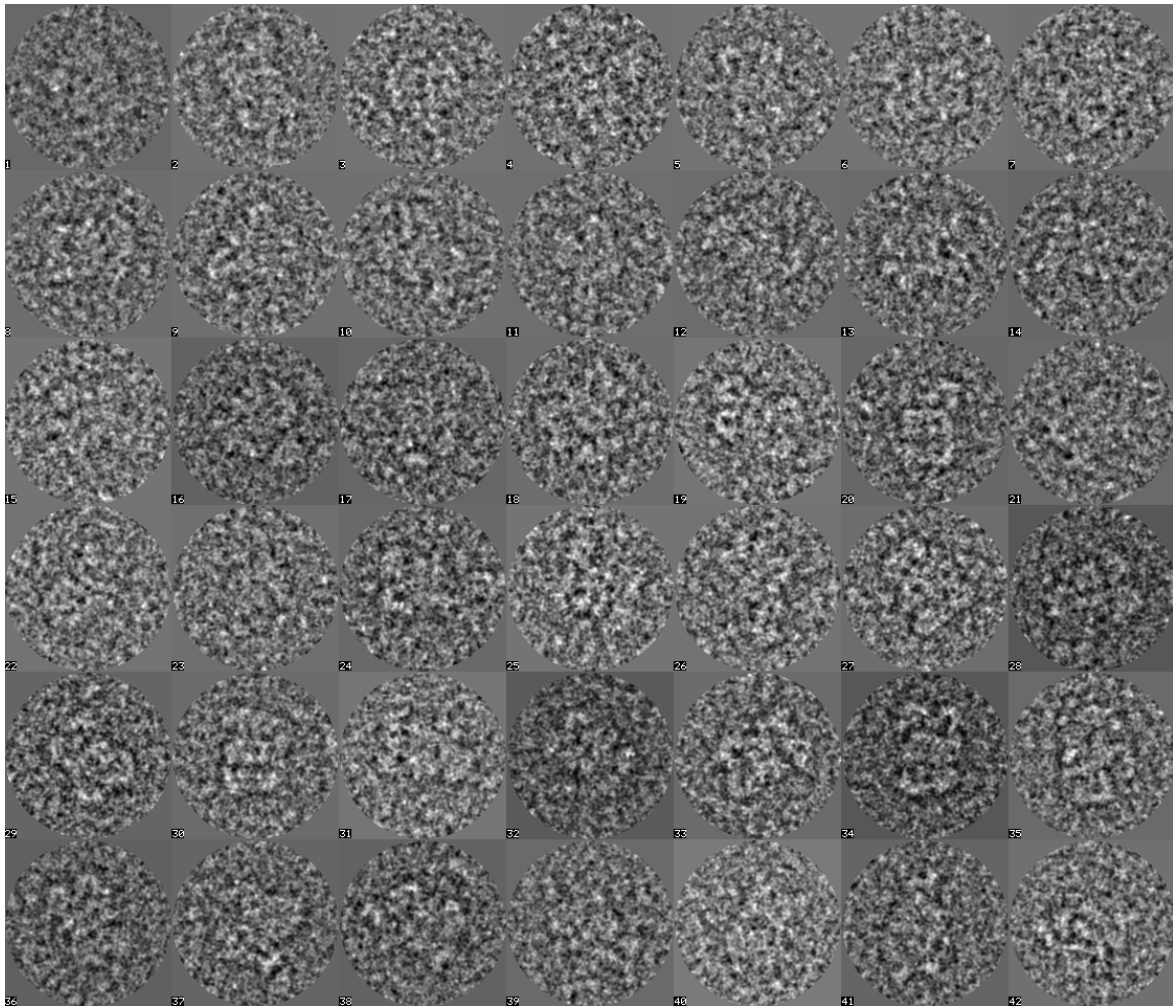


Figure 1-18 Schematic illustration of the preparation steps for further digital images processing. Particles were band pass filtered and a circular mask was applied.

1.4.3 Alignment

Extracted image data sets are expected to contain projection images of the same or very similar but randomly oriented macromolecules. Particles sharing the same orientation within the specimen generate similar projection images but at different locations resulting in translational degrees of freedom. Macromolecules basically oriented identically within the specimen except for a rotation around an axis perpendicular to the plane of the detector generate similar projection images with an additional in-plane rotation within the recorded image data sets. The aim of 2D alignment procedures is the identification of similar projection images within the data sets and thus identification of the translational and rotational parameters necessary to superimpose these similar views. This is solved computationally by the detection of a correlation maximum of images dependent on their translational and rotational parameters. Several flavors of such alignment algorithms are known. They have in common, a dataset usually containing only a small number of reference

images is compared to all the recorded projection images. The underlying algorithms evolved with computational power available. In early days rotational and translational alignment parameters were computed image by image subsequently, either by “direct alignment” algorithms, evaluating cross-correlation functions directly computing the translational and rotational parameters or in contrast, by indirect algorithms, evaluating auto correlation functions as reviewed by Frank (Frank 1996). Direct alignment algorithms are generally computationally more intense but also more accurate. The first implementation was a sequential algorithm using alternating rotational and translational searches (Steinkilberg and Schramm 1980) and direct computation of rotational and translational cross-correlation functions. The translational parameters leading to a correlation maximum of data image and reference image are computed upon 2D Fourier transformation of both images. Multiplication of the reference Fourier transform with the complex conjugated Fourier transform of a data image, followed by reverse Fourier transformation of the result leads to

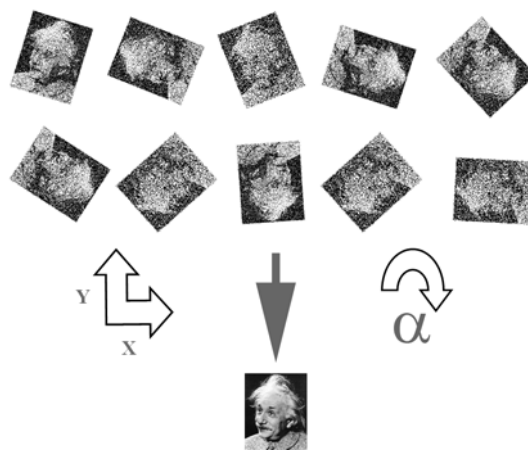


Figure 1-19 Schematic representation of translational and rotational degrees of freedom in 2D Alignment resulting in an “ali sum”, featuring improved signal to noise ratio.

the 2D cross correlation function of the aligned pair of images. The location of the highest value in the correlation function, determined by peak search, directly delivers the x and y shift to apply to the data image for translational alignment. The rotational alignment parameter can be obtained by first transformation of both data and reference images to polar coordinates resulting in 1D-lines per image. The 1D correlation function can be obtained by 1D Fourier transformation in analogy to the 2D case. A peak search in the 1D correlation function yields the rotation parameter for the alignment resulting in a maximum correlation value. Both rotational and translational alignments have to be performed multiple times subsequently until the solution is stable or a desired number of iterations is obtained. Because translation and rotation do not commute, the best possible solution may not be

obtained. In contrast to these approaches, carrying out translational and rotational alignment separately, a class of algorithms termed “exhaustive alignment” (Joyeux and Penczek 2002) test all possible combinations of rotational and translational alignment usually providing a better result but in parallel leading to higher computational demands.

The best results especially for data with a very low SNR are delivered by “exhaustive alignment by resampling to polar coordinates” (Joyeux and Penczek 2002). In this approach, for each possible centre of the particle within the desired translational alignment range, a sampling to polar coordinates is performed. For each of these translational alignment positions, a 1D rotational cross correlation has to be evaluated resulting in a possible alignment parameter. The following peak search, similar to the direct rotational alignment then directly yields translational and rotational alignment parameters without the need for evaluation of 2D cross correlation functions. The speed of direct alignments can be increased by using correlation images, termed “corrims” (Sander, Golas et al. 2003b) representing the correlation values of a previous alignment step e.g. using a coarse grained sampling of the input data. These corrims can then be used to restrict the translational and rotational parameters used for the exhaustive alignment to values represented by peaks in the corrims. In electron microscopy, alignment is normally performed relative to multiple references because in practice the aim is to identify the best match to a set of projection images. This approach is termed multi reference alignment (MRA) (Penczek, Grassucci et al. 1994a). Once the reference images yielding the best match to all the data images and their translational and rotational alignment parameters are obtained, these parameters are applied to the raw images. The raw images aligned to the different reference images can now be superimposed by summing them up pixel by pixel, followed by a normalization e.g. by the number of summed images to form so called alignment sums, termed “ali sums”. Since each projection image has a different level of uncorrelated noise, the ali sums feature an improved signal to noise ratio for the true correlated structure information. Additionally, single images summed up may have been recorded using a different defocus setting, such featuring different spatial frequency spectra resulting in a broader spatial frequency spectrum within the ali sums. To harvest this effect, the raw images have to be subjected to phase contrast transfer function correction first (compare section 1.3.6). Without inverted or flipped values for negative phase contrast transfer function regions, the information especially for high spatial frequencies would be extinguished.

1.4.4 Multivariate statistical analysis and clustering of aligned images

Alignment procedures described in the previous section require reference images relative to which the alignment is performed. To generate a first set of references, an approach termed “reference free” alignment scheme is used (Penczek, Radermacher et al. 1992; Dube, Tavares et al. 1993). The first reference used for alignment is obtained by summing up all raw images in the unaligned data set, followed by a rotational averaging.

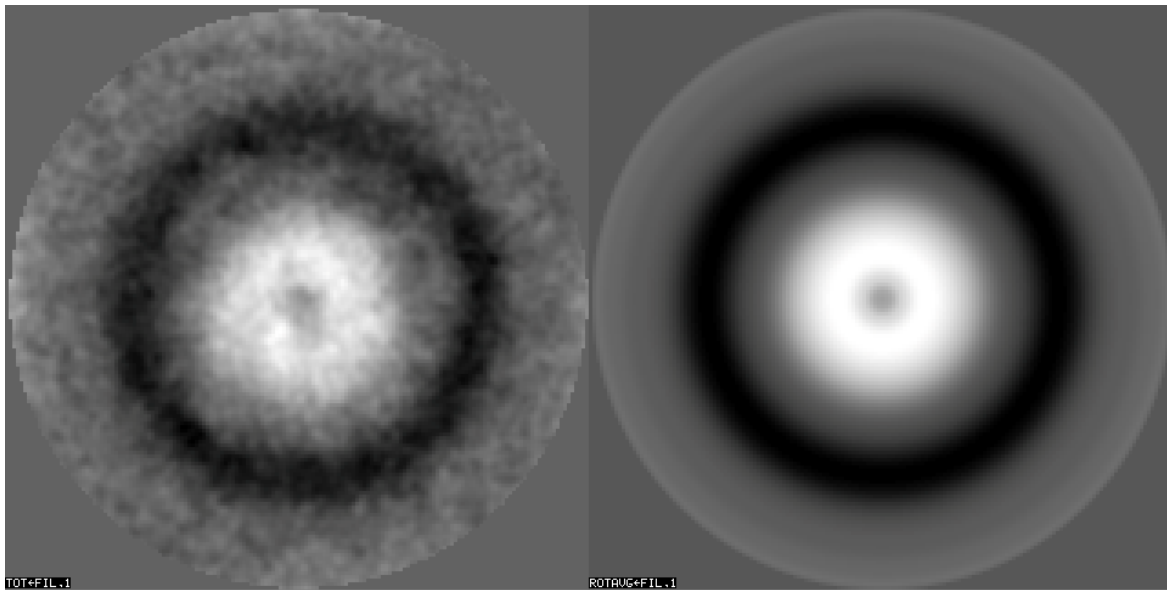


Figure 1-20 References for the "reference free" alignment scheme. The left image depicts the total sum of all randomly oriented particles in the data set (total sum). The right image is the result of a rotational averaging of the total sum and is used as the very first reference to achieve a centering of the particles by direct alignment.

The resulting image, containing bright pixels at the center and dark pixels at the edge has proven to be an ideal initial reference because it is virtually free of detail information that could bias the initial alignment and serves well to center the raw images by sole translational alignment. Once the raw images are centered, one aim of digital image processing is to separate the many different projection images into classes representing different projection views of the particle, ideally representing all different projection views, generated by the imaged particle. Algorithms identifying these similar views treat the data images with n pixels as vectors in an n -dimensional space.

Since it is computationally not possible to compare all raw images pixel by pixel, a reduction of dimensionality has to be applied. Several methods are known for the dimension reduction e.g. principal component analysis (PCA), independent component analysis (ICA) or multivariate statistical analysis (MSA). In the case of MSA, as implemented in the IMAGIC software suite (van Heel 1984; van Heel, Harauz et al. 1996) an orthogonal system of

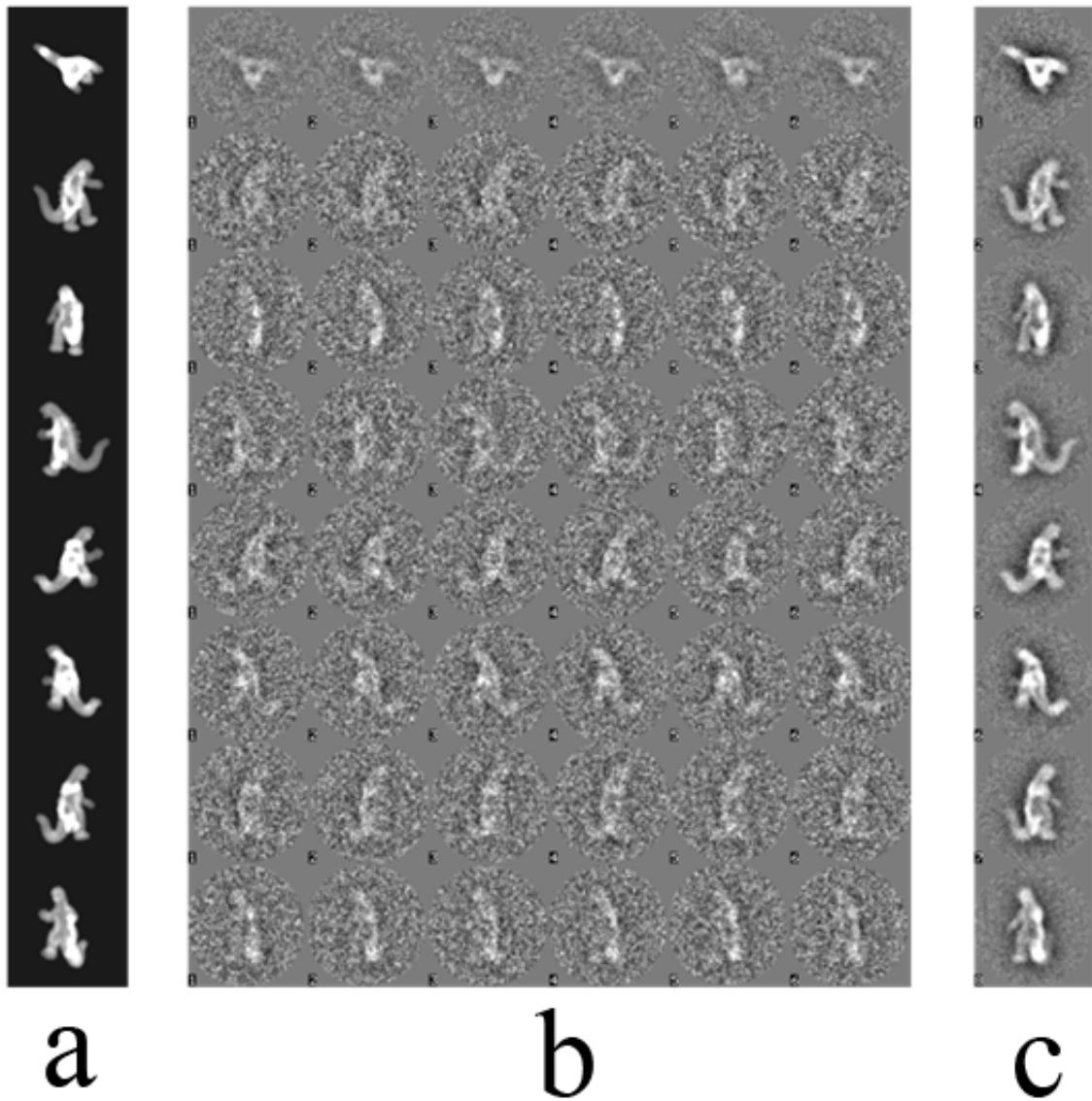


Figure 1-21 Noisy raw images identified to represent the same projection direction after alignment (b) can be summed up to form “class averages” (c) featuring improved signal to noise ratio. Obtained class averages (c) possibly band pass filtered and removed from surrounding noise can be used as references for a new round of alignment.

Eigenvectors (also called Eigenimages in the context of digital image processing) is computed. This system of Eigenimages is obtained by aligning its first axis along the direction of highest variance within the data set, followed by the second axis representing the direction of second highest variance and so on. The dimensionality of the fully orthogonal coordinate system is preset by the user. In the IMAGIC software system, a maximum number of 69 Eigenimages and thus a 69-dimensional, orthogonal coordinate system can be used. Once a stable coordinate system is obtained, it can be used to describe the data of images as linear combinations of these Eigenimages as accurately as possible. The images are projected onto the Eigenvectors resulting in a dramatic reduction of dimensionality, still preserving around 95% of the variance of the original image data set,

expressed by the Eigenvectors. Images can now be expressed as points within the coordinate system spawned by the Eigenvectors and thus clustered upon a distance metric e.g. Euclidian distance to form groups of images representing similar views. These images can then be combined to form class averages, improving the information content within the “class sums” in analogy to the formation of ali sums.

For iterative computation of the Eigenvectors, the n images of the data set, each consisting of m pixels are summarized in a $n \times m$ matrix X . New values for the coordinate system as described above are retrieved by solving the equation:

$$X^T N X M U = U \Lambda$$

Equation 1-23

where X^T is the transposed matrix of X , Λ is the matrix containing the Eigenvalues used to measure the variance described by each Eigenvector, M is a $m \times m$ and N a $n \times n$ weighting matrix defining the distance metric. The Eigenvector matrix U has to fulfill the orthonormalisation condition $U^t M U = I_p$ with I_p being the p -dimensional unit matrix (Lebart, Morineau et al. 1984). Once dimensionality reduction has been obtained, the data is classified using the hierarchical ascending classification method (HAC) with subsequent moving element refinement (van Heel 1984). Since Eigenimages obtained by MSA as described above are sorted according to Eigenvalues representing variance within the Eigenimages, higher order Eigenimages mostly containing noise only can be neglected for classification. The set of Eigenimages that HAC works on is such reduced to a number of ~ 50 images, resulting in a significant reduction of computational demands compared to the number of original pixels in the data set (which lies in the order 10^4 pixels). The HAC algorithm can now identify clusters within the pixel cloud representing the original data set. The number of desired clusters and therefore classes has to be preset by the user. When the algorithm starts, the number of classes equals the number of images in the data set resulting in one class per raw image. The algorithm now joins neighboring classes until the desired number of classes is obtained. The criteria for selecting raw images as members of classes are maximization of inter class variance and minimization of intra class variance. The following moving elements refinement (van Heel 1984) double checks every class members cluster membership and possibly moves it to another class. Other unsupervised classification methods applied in (cryo) EM single-particle studies are for example, K-means clustering (Penczek, Zhu et al. 1996), hierarchical hybrid (K-means and HAC) classification (Frank,

Brethaudiere et al. 1988), and self-organizing maps (Marabini and Carazo 1994; Zuzan, Holbrook et al. 1998). Often, unsupervised classification is being combined with multivariate data analysis such as correspondence analysis. In these studies, classification is either used to determine the projection orientations without regard to possible heterogeneity of the 3D structures, e.g. (Frank, Brethaudiere et al. 1988; Zuzan, Holbrook et al. 1998), or to divide projections representing a single view according to conformations (Marabini and Carazo 1994; De Haas, Taveau et al. 1996; Pascual-Montano, Donate et al. 2001). A method capable of classifying an entire projection set into different conformations is not yet available.

1.4.5 Iterative approach

The steps of MRA and MSA followed by classification are performed iteratively as depicted in Figure 1-22 until stable 2D class sums or ali sums with an improved signal to noise ratio are obtained. Selected class averages, obtained after MSA and classification treatment of initial raw data by reference free alignment are used as references for new alignment iteration. The cycle is then repeated until stable class averages are obtained, i.e. no improvement in respect to the previous iteration can be observed.

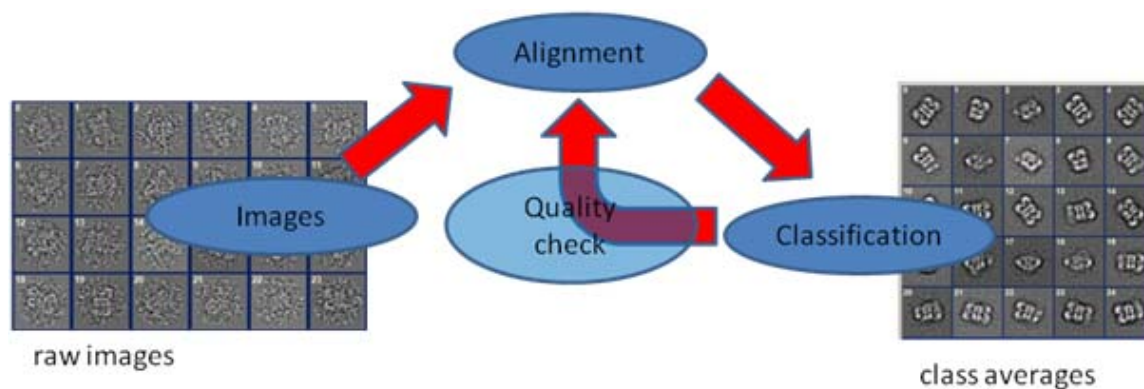


Figure 1-22 The steps of alignment and classification are performed iteratively until stable class sums are obtained. Class averages are used as reference images in the next alignment iteration.

After each iteration, the operator performs a manual quality check by separating meaningful class averages, representing typical projection views from classification artifacts, thus supporting an iterative self organization of the data set. The number of references in the alignment steps and the number of desired classes in the classification steps are subsequently increased.

1.5 Assignment of projection directions

1.5.1 Definition of Euler angles

Once stable 2D class averages are obtained, the task to complete before a three-dimensional reconstruction can be computed is the assignment of projection directions to the class averages. When this task is complete, the projection operation generating the raw images from three-dimensional objects can be reversed and a three-dimensional object can be reconstructed from the 2D projection images. In EM, the use of Euler angles for description of projection directions is a standard. Euler angles describe the orientation of a reference frame relative to another reference frame. In case of a Cartesian coordinate system (x,y,z) , following the Euler (z,x,z) convention, the relative orientation of a coordinate system (X,Y,Z) can be described by a set of three angles (α,β,γ) representing three rotations of the initial reference frame (x,y,z) around defined axis. The angle α corresponds to a rotation around the z axis, the angle β corresponds to a rotation around the x axis and the angle γ correspond to a rotation around the x' axis, the x axis obtained after applying α and β rotations.

$$R_{\text{Euler}} := R_{\text{Euler}}(\alpha, \beta, \gamma) := R(z, \alpha)R(x, \beta)R(z, \gamma)$$

Equation 1-24

where $R()$ denotes the respective rotational matrix.:

$$R(x, \theta) = \begin{bmatrix} 1 & 0 & 0 \\ 0 & \cos\theta & -\sin\theta \\ 0 & \sin\theta & \cos\theta \end{bmatrix}$$

Equation 1-25

$$R(y, \theta) = \begin{bmatrix} \cos\theta & 0 & \sin\theta \\ 0 & 1 & 0 \\ -\sin\theta & 0 & \cos\theta \end{bmatrix}$$

Equation 1-26

$$R(z, \theta) = \begin{bmatrix} \cos\theta & -\sin\theta & 0 \\ \sin\theta & \cos\theta & 0 \\ 0 & 0 & 1 \end{bmatrix}$$

Equation 1-27

Matrix multiplication of Equation 1-24 then leads to:

$$R_{Euler} = \begin{pmatrix} c\alpha c\beta c\gamma - s\alpha s\gamma & -c\alpha c\beta s\gamma - s\alpha c\gamma & c\alpha s\beta \\ s\alpha c\beta c\gamma + c\alpha s\gamma & -s\alpha c\beta s\gamma + c\alpha c\gamma & s\alpha s\beta \\ -s\beta c\gamma & s\beta s\gamma & c\beta \end{pmatrix}$$

Equation 1-28

With abbreviations $c\alpha := \cos(\alpha)$, $s\alpha := \sin(\alpha)$ and similar for β and γ .

Euler angles can be used to describe orientations relative to a given reference. They can be used to describe the orientations of bodies in a fixed reference frame (three-dimensional rotations) or they can be used to express directions within a reference frame as used in the case of the projection direction assignment. Euler angles can be obtained from the Rotation matrix R_{Euler} by the following relations:

$$\sin\beta = \sqrt{1 - R_{Euler,33}^2}$$

Equation 1-29

$$\alpha = \arctan\left(\frac{\pm R_{Euler,23}}{\pm R_{Euler,13}}\right)$$

Equation 1-30

$$\beta = \arctan\left(\frac{\pm \sin\beta}{\pm R_{Euler,33}}\right)$$

Equation 1-31

$$\gamma = \arctan\left(\frac{\pm R_{Euler,33}}{\pm R_{Euler,31}}\right)$$

Equation 1-32

Where $R_{Euler,ij}$ is the matrix element in the i 'th row and j 'th column of the matrix R_{Euler} . Euler angles are not unambiguous. Within the interval $[-\pi, \pi]$ two solutions exist, following the relation:

$$R_{Euler}(\alpha, \beta, \gamma) = R_{Euler}(\alpha - \pi, -\beta, \gamma - \pi)$$

Equation 1-33

A special case is the so called singularity for $\beta=0$. In this case a rotation around the z-axis is performed twice.

1.5.2 Established methods for assignment of projection directions

Several methods are established for the assignment of projection directions e.g. Euler angles, once stable class sums are obtained after several rounds of MSA and MRA. If a three-dimensional structure for an identical comparable macromolecular assembly is already available, it can be used for assignment of projection directions by projection matching. Depending on the likelihood homology modeling may be applied first.

1.5.3 Angular reconstitution

For macromolecular assemblies featuring intrinsic symmetry properties, the method of choice is the angular reconstitution method (van Heel 1987) working by peak search in combination with utilization of symmetry properties in sinogram correlation functions.

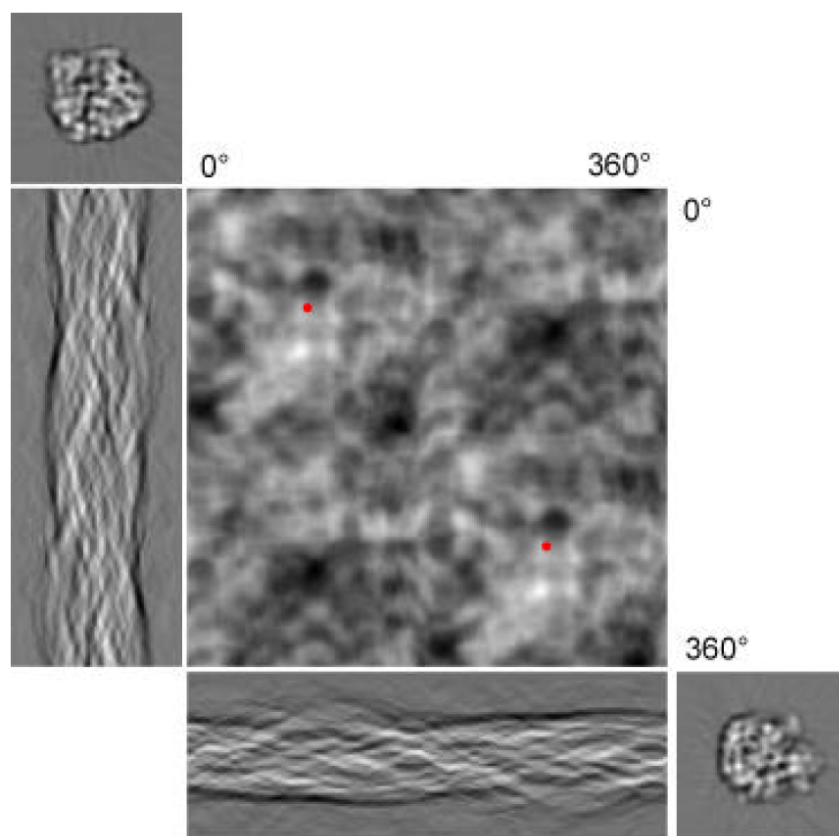


Figure 1-23 Angular reconstitution. The figure shows two asymmetric projections (upper left and lower right), their sinograms and the corresponding sinogram correlation function. The two maxima of the sinogram correlation function (red points) allow calculating the angular relationship of the two projections with the Euler algorithm (van Heel 1987).

This method is based on the Fourier central line theorem stating that the views generated by two different projections generated by the same three-dimensional objects share at least one

similar one-dimensional line. Once the similar lines and their relative positions are obtained, this property can be used to calculate the angular orientations of the projection views. An image containing all possible one-dimensional line projections, thus the result of a radon transform of a digital image is termed a sinogram. Sinograms can be correlated line by line resulting in a sinogram correlation function. A peak search within the sinogram correlation function in combination with trigonometric analysis then delivers the angular distance of the compared projection images.

1.5.4 Tilt series

When the particle of interest does not feature high internal symmetry, angular reconstitution can still be used by identification of orthogonal projection views of a homogeneous sample (Schatz, Orlova et al. 1997). Although this technique was successfully applied to asymmetric particles such as the 70S *E. coli* ribosome (Stark, Mueller et al. 1995; Stark, Orlova et al. 1997), it is challenging and requires a high amount of user interaction. To provide views from different projection directions, preferably with known angular relationships, the specimen can be tilted in the electron microscope and an image can be recorded at each tilt angle setting. Without any assumptions on the underlying structure i.e. symmetry properties, the reconstruction can then be calculated from the tilt series (Hoppe, Schramm et al. 1976a; Hoppe, Schramm et al. 1976b; Hoppe, Schramm et al. 1976c). Since all reconstruction techniques from electron micrographs encounter the major problems of damage to the specimen by exposure to the electron beam, the number of images acquired within one tilt series is limited. Conventional reconstruction techniques rely on the tilting of the same specimen by a small angular increment, resulting in a high number of exposures and thus a substantial electron dose. This technique can be applied to biological objects (Taylor, Tang et al. 1997), and nowadays is performed routinely e.g. in imaging of cell organelles. Using the single axis tilt geometry, a tilt range of 180° would be necessary to fully reconstruct the structure of interest. Due to mechanical limits, a range of 120° - 140° is available, leading to a missing wedge in the Fourier Transformation of the imaged object resulting from the angular range not covered (Frank 1996). Additionally, the imaging area has to be kept centered and eucentric during acquisition of a tilt series which usually requires shift and focus adjustments. In parallel, the overall electron dose has to be minimized. These challenges led to the development of reconstruction techniques requiring only one exposure per particle, which usually rely on the particle to feature symmetry properties or a three-dimensional starting structure to be available (compare section 1.5.3). To minimize the missing wedge of information, the specimen can be tilted by a fixed angle and additionally,

be rotated in plane by small angular increments, using special “conical” tilt stages. This leads to a conical geometry with the tilt angle as the cone opening angle, resulting in an increased angular range covered. Now a missing cone of information is present (Frank 1996), reducing reconstruction artifacts from the single axis tilt geometries missing wedge. However, this approach requires a much larger number of images to be used for the reconstruction (Radermacher and Hoppe 1978).

1.5.5 Random Conical Tilt (RCT)

The random conical tilt (RCT) method (Radermacher, Wagenknecht et al. 1987) depends on the analysis of tilted image pairs. Every specimen location is imaged exactly twice at different tilt angles of the specimen holder relative to the electron beam. The tilted pairs acquired by this approach have a known relative orientation with respect to the experimental tilt angle set by the operator. Usually tilted pairs are recorded with one untilted and one tilted orientation resulting in tilt angles of e.g. 0° and $+45^\circ$. When classification is performed on the untilted images, the alignment angle α of the untilted class members can be translated to an Euler angle γ of the respective “tilt mates”. The combination of information acquired by acquisition of tilted pairs in combination with MSA and MRA leads to a conical tilt geometry and tilt series in which every particle was only exposed two times. The cone opening angle which is again the experimental tilt angle set covers the angular range of missing information. The “tilt mates” of the aligned class members belonging to the untilted class sum of interest then form a halo on the cone with defined Euler angles relative to the untilted class sum as depicted in Figure 1-24. In real space, the reconstructions obtained using this method show a lower resolution in the direction perpendicular to the specimen in combination with additional artifacts. A structure can be reconstructed per two-dimensional class sum. The class sum based three-dimensional models obtained by the RCT approach have to be aligned in three-dimensional space i.e. using a rigid body registration algorithm. This alignment is aggravated by the missing cone of information, since the cross-correlation coefficients obtained during three-dimensional alignment of volumes strongly depend on the degree of overlap in Fourier space, most likely leading to an alignment of the missing cones (Penczek, Radermacher et al. 1992; Penczek, Grassucci et al. 1994b). This alignment challenge can be overcome by using a likelihood function instead of a cross correlation function (Sander, Golas et al. 2006) but merging of volumes may still be further complicated due to flattening of the sample (Carazo, Wagenknecht et al. 1989; Boisset, Taveau et al. 1990) which can be avoided by imaging under cryo conditions. Nevertheless, the RCT method applied to negatively stained data empirically proved to deliver reliable

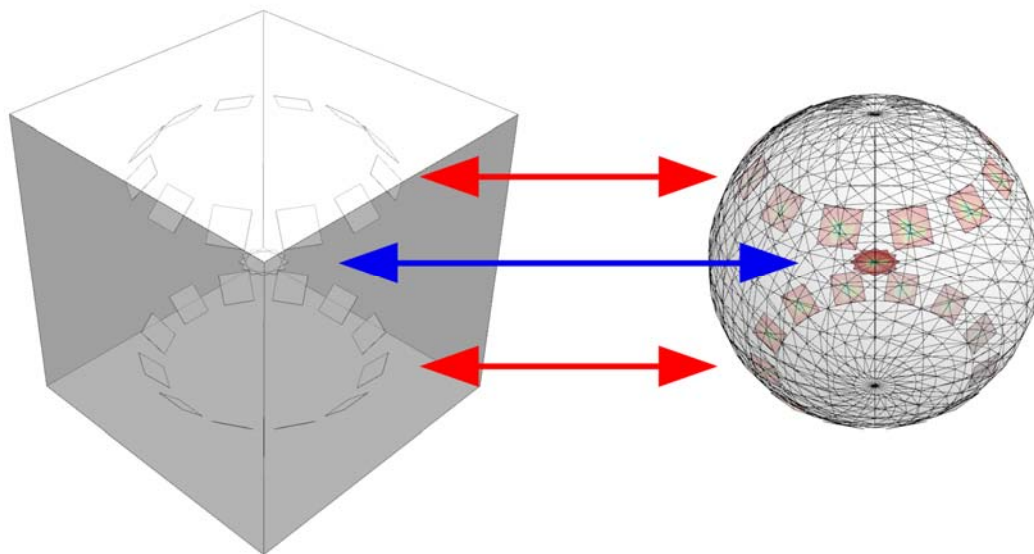


Figure 1-24 Schematic illustration of the Random Conical Tilt approach. The blue arrow in the Figure points at an untilted class sum, consisting of several class members aligned in plane by different angles α . Every single particle image belonging to this class sum has an experimental tilted mate (indicated by the red arrows). The angular relationship between the untilted class sum and the tilted single particle images are given by the experimental tilt angle β , here 45° and the in plane rotational alignment of the respective untilted tilt mate. The tilted mates can now be assigned with projection directions with respect to the untilted class sum. (In projection, two identical solutions exist per tilt mate.) The geometry leads to a “missing cone” of information.

three-dimensional starting models, when untilted class sums used for the reconstruction have ~ 30 members resulting in angular distances of the class members used for the reconstruction of $\sim 15^\circ$ if they are uniformly spaced on the cone (which is not always the case). The missing cone problem can only be overcome when the particles are really randomly oriented on the specimen grid. If a preferred particle orientation within the specimen and a missing cone in the reconstruction coincide, the missing cone cannot be filled in by averaging of several obtained three-dimensional models since the direction of the missing cone will then always be nearly the same. Although these problems are not insurmountable, they do make determination of an initial structure the challenge that it presently is.

1.5.6 Orthogonal tilt

An improvement over RCT featuring no missing cone is the orthogonal tilt reconstruction (OTR) method (Leschziner and Nogales 2006) only theoretically introduced and yet lacking experimental proof. In this approach, tilted pairs are recorded at tilt angles of -45° and $+45^\circ$ resulting in an effective tilt angle of 90° and thus free of a missing cone. The resulting geometry will then be cylindrical with the projections used for the reconstruction aligned on the equator of the cylinder as depicted in Figure 1-25.

For this approach, alignment and classification have to be performed on projection images recorded with a tilted specimen holder. Classification of tilted images can only be performed reliably under cryo conditions with unstained specimen and without a second carbon film sandwiching the sample (see Figure 2-2). Otherwise the classification will be aggravated because the specimen is flattened by $\sim 30^\circ$ between two carbon films and the “stain shadow” also affects classification. Additionally, the defocus has to be corrected for when images are recorded with a tilted specimen holder. Otherwise an image shift used for recording large areas of the specimen will result in a defocus gradient within the data set depending on the position of the individual particle in respect to the tilt axis of the specimen holder, also affecting alignment and classification. To record and classify projection views using a tilted specimen holder, thus a microscope with an extremely stable, computer controlled specimen holder (compustage) and dynamic focusing is required (Zemlin 1988). Similar to the RCT approach, in OTR, the computed three-dimensional models per class sum are randomly

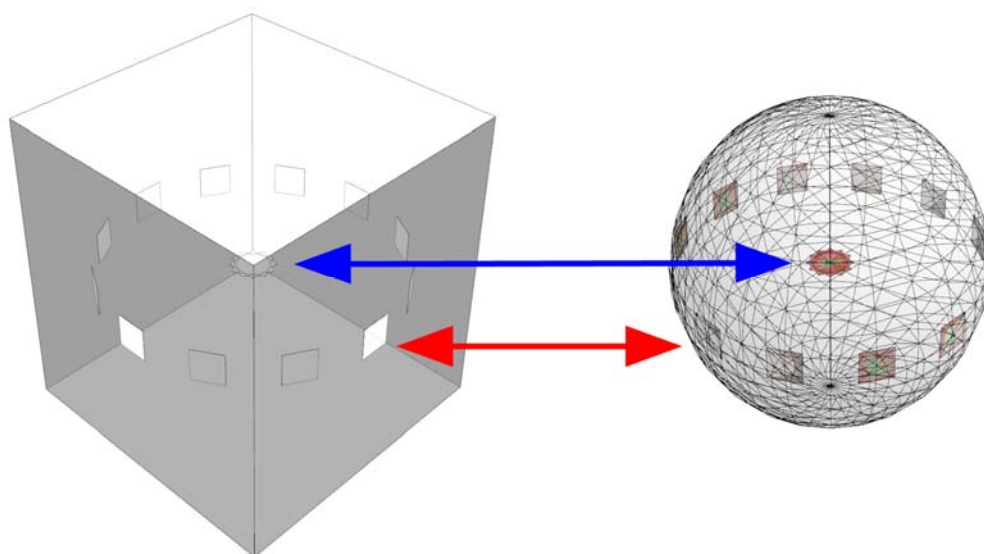


Figure 1-25 An obvious resort from the missing cone problem is to increase the tilt angle to 90° . Since tilting the specimen holder to 90° is not possible this can be achieved by acquiring tilt pairs at -45° and $+45^\circ$ resulting in an effective tilt angle of 90° . This is only feasible under cryogenic conditions with a very stable specimen holder and the defocus corrected for. Now the blue arrow points at a -45° class sum and the red arrow to its corresponding tilt mates according to their angular relationships. Since the planes are perpendicular to each other, there is no missing cone, no area of projection directions without information.

oriented and have to be aligned in three-dimensional space for further analysis.

1.6 Reconstruction techniques

Once projection directions are assigned to projection images, a three-dimensional structure can be calculated. A variety of reconstruction algorithms have been developed based on the

Radon transform (Radon 1917). Radon's theorem states that any real function in an n -dimensional Euclidean space, obeying certain regularity conditions, can be uniquely expressed by its integrals over all $(n-1)$ -dimensional hyper planes. Basically this means that a function defined on a two-dimensional plane can be reconstructed from its one-dimensional projections and a function defined in three dimensions from its two-dimensional projections. This property can be used to inverse the process generating projection images from three-dimensional objects to implement a back-projection algorithm by inverting the Radon transform.

1.6.1 Fourier based methods

Fourier methods, make use of the projection theorem stating that the Fourier Transform of a projection is a central section of the Fourier Transform of the object generating the projection (Mersereau and Oppenheim 1974; Stark, Woods et al. 1981). This is the same theorem applied in the angular reconstitution approach (compare 1.5.3) now in three dimensions. The origin of the Fourier Transform of the object and the Fourier Transform of the individual projection image (section) coincide. The orientation of the individual section is given by the projection directions assigned to the respective projection image. Using multiple two-dimensional Fourier sections, the three-dimensional object Fourier transform can thus be resampled. An inverse Fourier transformation then leads to a three-dimensional real space representation of the imaged object. Different Fourier reconstruction methods differ in the type of Fourier interpolation and the system of functions used.

1.6.2 Direct methods

The direct reconstruction methods are also termed back projection or summation techniques (Vainshtein 1971). Each pixel of the projection image is used as the source of a ray, the pixel values are "smeared" out perpendicular to the plane of the respective projection image. The individual projection images are previously oriented in three dimensions to a common center according to their projection directions or Euler angles. The projection body, consisting of all obtained rays is then summed up, resulting in a three-dimensional representation of the underlying structure. Back projection algorithms mainly differ in the filter and weighing functions as well as interpolation methods used. The most common back projection algorithm used in EM is the "exact" filtered back projection method (van Heel and Harauz 1986), addressing the discrete character of the set of projection orientations. In contrast to analytic filtering, where a filter function - derived from an idealized situation of infinitely many projections, uniformly distributed over a well defined angular range - is applied to all

projection images, the “exact” filters, generated by a heuristic approach are different for each individual projection.

1.6.3 Iterative methods

The performance of back projection algorithms can be improved by applying them iteratively. The object is first reconstructed by a simple back-projection and then used to recalculate projections from this object by forward re projecting the object in the direction of the individual input projections. The deviations between input and output projections are then used to correct the reconstructed object. Several established methods exist mainly differing in the underlying error assessment and correction functions. The Algebraic Reconstruction Technique (ART) (Gordon, Bender et al. 1970) corrects the pixel differences in input and output projections by either evenly distributing and adding the absolute pixel difference to all voxels (the 3D analog of pixels) along the individual ray (additive ART) or by multiplying every voxel along the ray with the error ratio between input and output projections (multiplicative ART). In contrast to ART techniques, where every projection image is treated subsequently, the Simultaneous Reconstruction Technique (SIRT) (Gilbert 1972) applies error correction and determination for all Projection images simultaneously.

1.6.4 Refinement via projection matching once a start structure is determined

Once a 3D structure is available a forward projection algorithm can be used to generate a set of projection views, evenly spaced over the Euler unit sphere that can be used as references for a new round of MRA. References generated from a 3D volume contain information from all 2D class averages used for the three-dimensional reconstruction and therefore exhibit a much better signal to noise ratio than 2D class averages.

Additionally, these references can serve to detect underrepresented projection directions within the 2D data set. After MSA and MRA using the references generated from the forward projection of the 3D Volume, Euler angle assignment can also be refined using the angular reconstitution approach, and a new 3D volume featuring an improved resolution can be obtained. The iterative cycle depicted in Figure 1-26 is repeated until a stable 3D volume is reached.

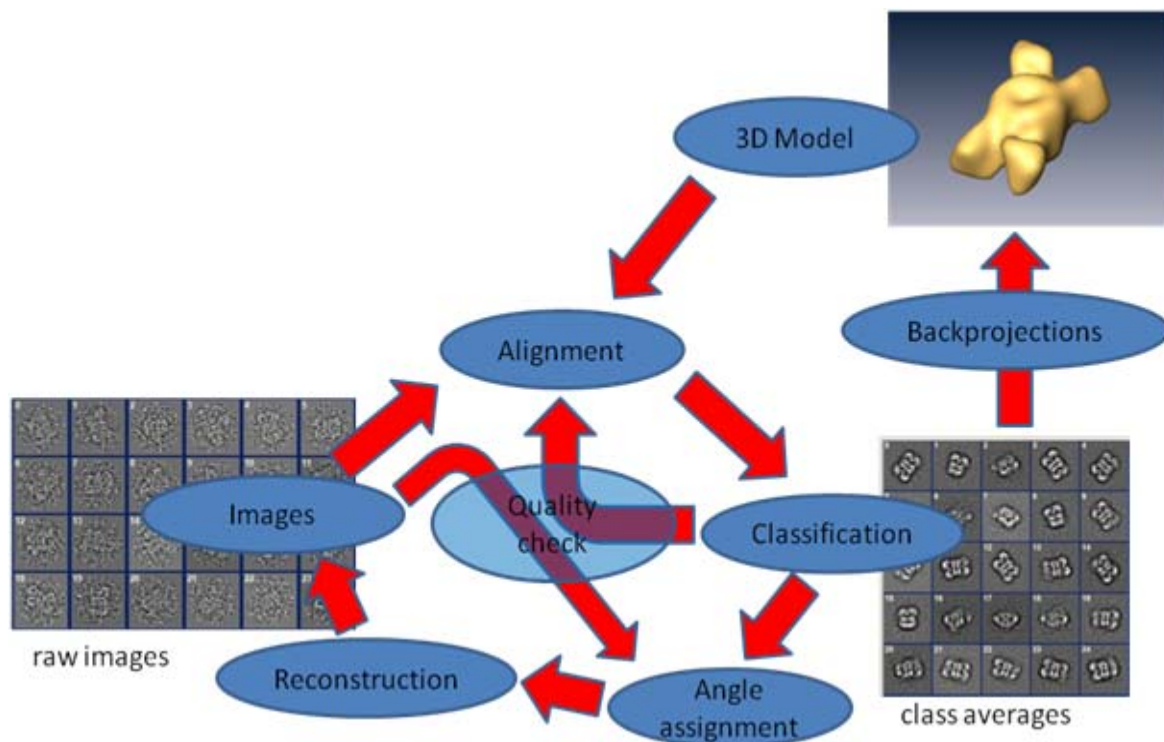


Figure 1-26 Once an initial 3D model is obtained it can be used to generate reference images for alignment and classification by forward projection. These reference images can be used to refine the 3D model via projection matching.

Since projection matching can be used for classification, by building classes upon the highest correlation value obtained by MRA, the MSA and classification steps can be omitted. This classification method is termed “supervised classification” (Penczek, Grassucci et al. 1994b) if different sets of independent reference data are used. This classification approach requires sets of reference images in contrast to classification by MSA and HAC, also termed “unsupervised classification”. The step of angular reconstitution can also be omitted by using the sets of Euler angles assigned to the set of reference images by the forward projection algorithm. For resolution improvement of an already reliable three-dimensional starting structure, projection matching is the method of choice while MSA and HAC in combination with angular reconstitution or RCT are the methods of choice for computation of initial starting models for later refinement.

Due to the optical and imaging properties, refinement of starting models images recorded with an untilted specimen holder are used, mainly because the defocus variance will be much smaller and a flattening effect of the particles by sandwich preparation techniques is much less influencing because the electron beam is perpendicular to the embedding carbon layers.

1.7 Determination of obtained resolution by Fourier-Shell-Correlation (FSC)

The resolution of a three-dimensional model is defined by the highest spatial frequencies in the dataset exhibiting structural information and not noise. In EM, resolution is measured upon the Fourier-Shell-Correlation (FSC) (Saxton and Baumeister 1982; van Heel and Stoffler-Meilicke 1985) based on the 2D equivalent Fourier Ring Correlation (FRC) (Harauz and van Heel 1986). The data set is split into two subsets, and two independent three-dimensional structures are computed using the techniques described above. The correlation of the two three-dimensional structures is then assessed in 3D Fourier space as a function of the shell radius S :

$$FSC(S) = \frac{\sum_{R=S} F_1(R) F_2^*(R)}{\sqrt{\sum_{R=S} |F_1(R)|^2 \sum_{R=S} |F_2(R)|^2}}$$

Equation 1-34

where F_1 is defined as the 3D Fourier transform of the first 3D structure, F_2 as the three-dimensional Fourier transform of the second 3D structure and $*$ denotes the complex conjugated Fourier transform. Typical FSC-curves and their interpretation are depicted in Figure 1-27 and Figure 1-28. Even if a “healthy” FSC can be obtained (see Figure 1-27), a positive value for a specific spatial frequency is no criterion for obtained resolution. A threshold criterion has to be introduced to separate correlated structural information from uncorrelated noise. The first criterion introduced was the 3σ -criterion which individually defines a Gaussian significance level as a function of underlying particle symmetry resulting in a threshold curve, taking into account the statistical properties of underlying, principally uncorrelated noise (van Heel and Harauz 1986). Even voxel volumes, consisting of random noise only, might lead to positive correlation values for random spatial frequencies. Nevertheless, 99% of uncorrelated 3D models will not lead to correlation values higher than the 3σ threshold curve. Therefore, the intersection of the FSC and the 3σ -threshold can be used to define resolution. In contrast to this dynamic approach, taking into account the number of voxels in a given Fourier shell, fixed-value criterions exist, e.g. the fixed $FSC_{0.5}$ criterion (Beckmann, Bubeck et al. 1997). This is a very conservative criterion, whose application will most likely not lead to an overestimation of resolution achieved (if over fitting is neglected). In contrast to the $FSC_{0.5}$ criterion, which is based on experience only, the $FSC_{0.143}$ criterion (Rosenthal and Henderson 2003) is based on information theory. Fixed resolution criteria do not take into account the underlying particle symmetry and the number

of voxels in a shell and are thus argued not to be reproducible (van Heel and Schatz 2005). Apart from the determination of resolution obtained, the FSC can serve to identify systematic errors within the reconstructed volumes. In Figure 1-27 a “healthy” FSC and the application of the $FSC_{0.5}$ criterion is depicted. The low spatial frequencies remain at one, followed by a semi Gaussian slope around $\frac{2}{3}$ of maximum frequency. In high frequencies, dominated by uncorrelated noise, the FSC oscillates around zero.

In Figure 1-28 a) to d) “unhealthy” FSC plots are depicted. In Figure 1-28 a), the FSC increases again in high frequencies. This FSC indicates that either the data was harshly low-pass filtered, interpolation during image processing caused artifacts in the form of artificial high frequencies, or that all images were rotated by the same angle leading to an alignment of noise. This type of FSC curve can also be observed, when the compared 3D models were masked. The FSC in Figure 1-28 b) never drops to zero in the whole frequency range. This means that either the data was severely under sampled or the noise in the data was

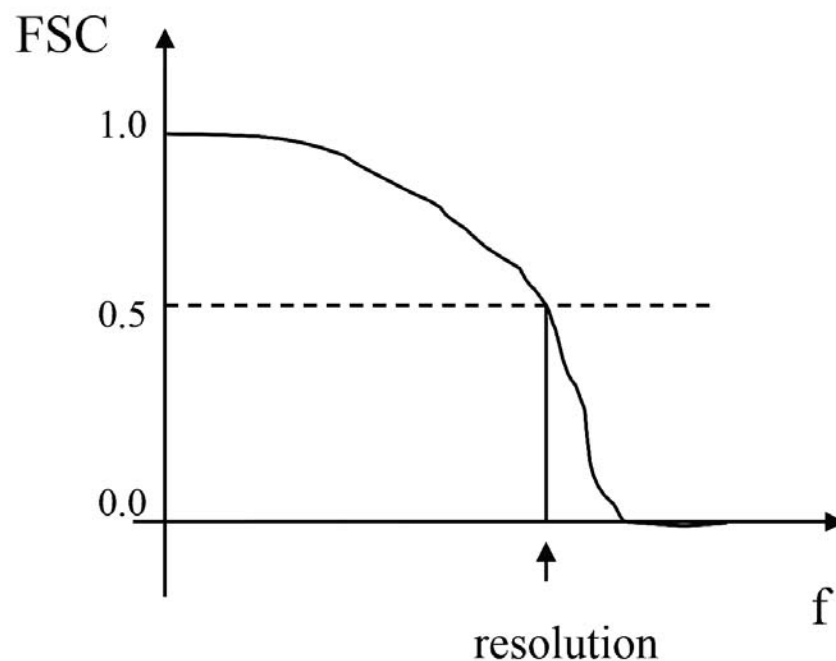


Figure 1-27 A “healthy” FSC and the application of the $FSC_{0.5}$ criterion. Low spatial frequencies remain at one, followed by a semi-Gaussian fall-off at around $\frac{2}{3}$ of maximum frequency. In high frequencies, dominated by uncorrelated noise, the FSC oscillates around zero.

aligned. In Figure 1-28 c) the fall-of is not semi-Gaussian, but a sharp drop-off occurs. The most likely cause for this type of FSC plot is a very sharp filtration leading to an alignment of remaining noise. Figure 1-28 d) depicts an FSC obtained from data with no or inaccurate defocus correction. The resolution cannot be determined and artifacts are to be expected in the model.

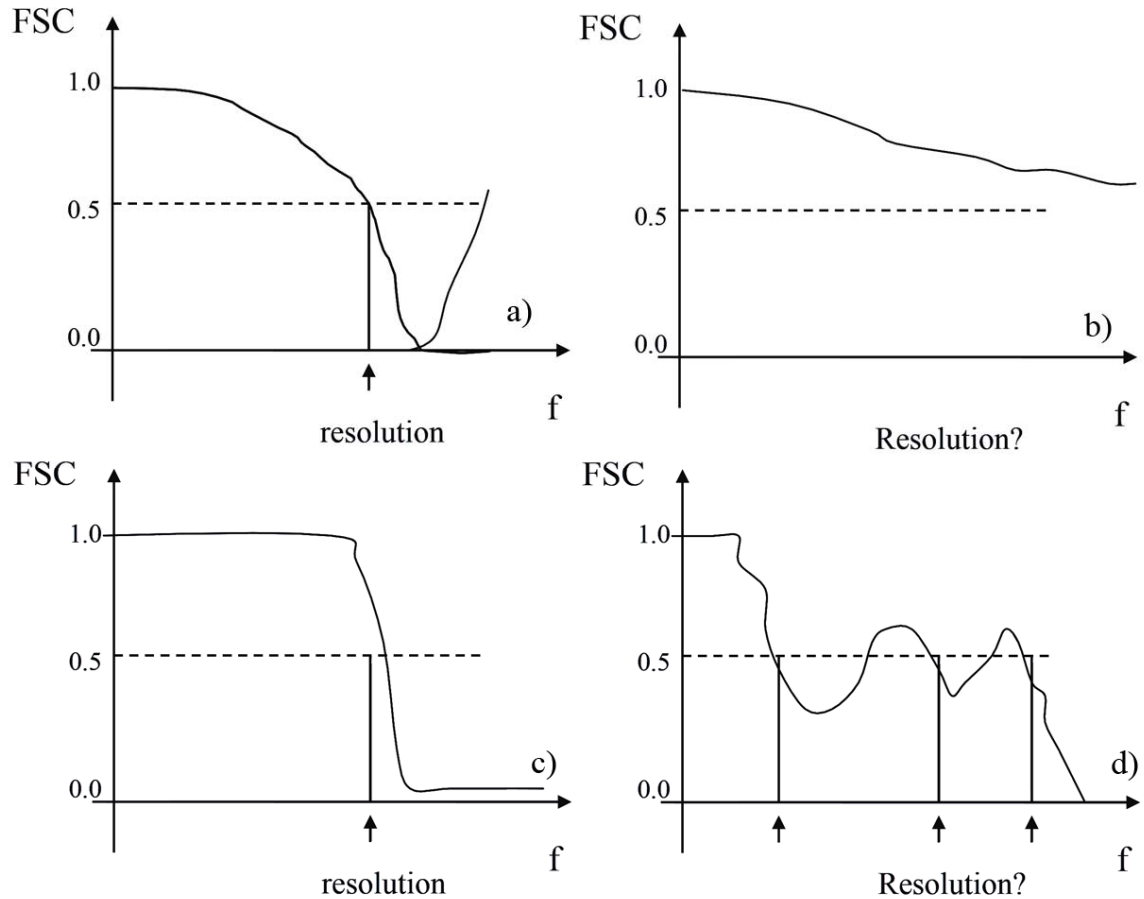


Figure 1-28 Examples of „unhealthy“ FSC plots and their interpretation. In a) the increase in high frequency after the zero crossing indicates a sharp masking of three dimensional volumes compared, an interpolation error in image processing algorithms used or an alignment of noise. The missing zero crossing and the slow decay in b) indicates a severe undersampling of the data or an alignment of the noise component. The sharp drop-off in c) indicates a very sharp filtration of data during alignment process and thus an alignment of remaining, filtered noise. The FSC behavior in d) indicates that either no or erratic defocus correction was performed. Figure modified from (Penczek 2005)

1.8 Improvement of processing speed for algorithms used in EM

1.8.1 Need for speed

Due to the ever-increasing data collection speed and thus the increasing number of images available for further analysis, computational performance plays a central role in three-dimensional single particle electron (cryo) microscopy. Computational demands are especially large for high-resolution structure determination because an ever-increasing number of images is currently being used to improve the resolution limits of this technique. There is certainly some linear computational speed increase in CPU technology that can be expected in the future, however, most of today's actual speed increase is already based on multi-core CPU architecture. Certain applications, such as the alignment of large amounts of single particle cryo-EM images and the three-dimensional reconstruction of these, will

require significantly more computational power than current improvement in CPU technology can offer. In some areas future applications will become possible only if the computational power can be increased by at least two orders of magnitude. The increase in computational power is thus essential to keep up with many modern scientific technologies.

1.8.2 How to improve computational speed?

For many standard applications, programmers did not have to worry about performance because the Central Processing Unit (CPU) manufacturers improved the hardware speed sufficiently over the last decades. In those cases it was a valid approach for many years to simply wait for the hardware to become faster. Moore's Law (Moore 1965) which states that processing power doubles every 18 months, turned out to be correct for the entire decade of the 1990s. Improvements in gates-per-die count or transistors per area (the main attribute of CPUs on which Moore based his law), the number of instructions executed per time unit (clock speed) and so called instruction level parallelism (ILP), lead to the possibility of performing more than just a single operation within the same clock cycle (for example summing up two registers and copying the result to another register). Today this gratuitous “free lunch” (Sutter 2005; Sutter and Larus 2005) of performance gain is over. Already for a few years, since 2003, CPU manufacturers have started selling CPUs with more computational cores instead of faster CPUs because the laws of physics put an end to the increase in clock speed. One simple explanation for that is that twice the clock speed also means half the distance traveled by the electrical signal per clock cycle, which requires the physical size of the CPU to be twice as small. Reducing the physical dimensions of CPUs is, however, limited at least by the diffraction limits of lithographic methods used for chip manufacturing. Other methods are used to increase performance that can at least partially compensate for the now limited increase in clock speed. These are for example sophisticated ILP schemes, speculative execution and branch prediction that nowadays are the only remaining basis for performance improvement apart from gate count (Schaller 1997). These methods are what manufacturers focus on today, resulting in feature rich CPUs, that are additionally equipped with an increasing number of computational cores. While an increased clock cycle automatically speeds up an existing application, this is not the case for additional CPUs or cores. Here it depends on the computational problem, the algorithm used to solve it and the application architecture (to what extent the application can benefit from additional cores). Performance improvement is then totally dependent on the programmer who has to develop optimized code to get the maximum possible speedup. For the next decade the limiting factor in performance will be the ability to write and rewrite

applications to scale at a rate that keeps up with the rate of core count. Outlining applications for concurrency may be the “new free lunch” (Wrin 2007), the new way of utilizing even higher core counts in the future without having to rewrite the code over and over again.

1.8.3 Divide et impera

To what extent an algorithm can benefit from multiple CPU cores to be speeded up using distributed or parallel processing depends on several conditions. In the first place, it must be possible to break down the problem itself into smaller sub problems. This divide and conquer approach is the main paradigm underlying parallel and distributed computing. The main question is how many independent chunks of work are ready to be computed at any time and what is the amount of CPUs or computational cores that can be harnessed. Usually, a problem or algorithm will consist of a fraction that is serial and cannot be processed in parallel, i.e. when a computation depends on a previous computational result. The class of problems termed “embarrassingly parallel” describes the ideal case, when all the computations can be performed independently.

1.8.4 Hardware architectures and their implications for parallel processing

The building block of all given computers is von Neumann architecture. (von Neumann 1946) (Figure 1-29.) The main principle is that the memory the CPU works on contains both program instructions and data to process. This design was known to be theoretically limited from the very beginning. The connection system between data and program instructions, the so-called Data- and instruction bus, can become a communication bottleneck between processor and memory. No problems existed as long as processing an instruction was slower than the speed of providing data to process. In reality up to the 1990s CPUs used to be the slowest unit in the computer while the bus speed was still sufficient. The so-called von Neumann Bottleneck was a mere theoretical problem at that time. Starting in the mid 1990s, CPU clock speed improvement outran random access memory (RAM) speed, making actual execution faster than the data feed. The combination of memory and bus therefore nowadays forms the von Neumann bottleneck, which is mostly overcome or attenuated by caching, basically meaning integrating a fast but small memory directly into the CPU. That explains why the CPU speed increases usually in parallel to the length of the cache lines. The single-threaded processing leading to multiple processes running through the same single-threaded pipe, accessing all their data through a single

memory interface led to today's processors having more cache than they do logic in order to keep the high-speed sequential processors fed.

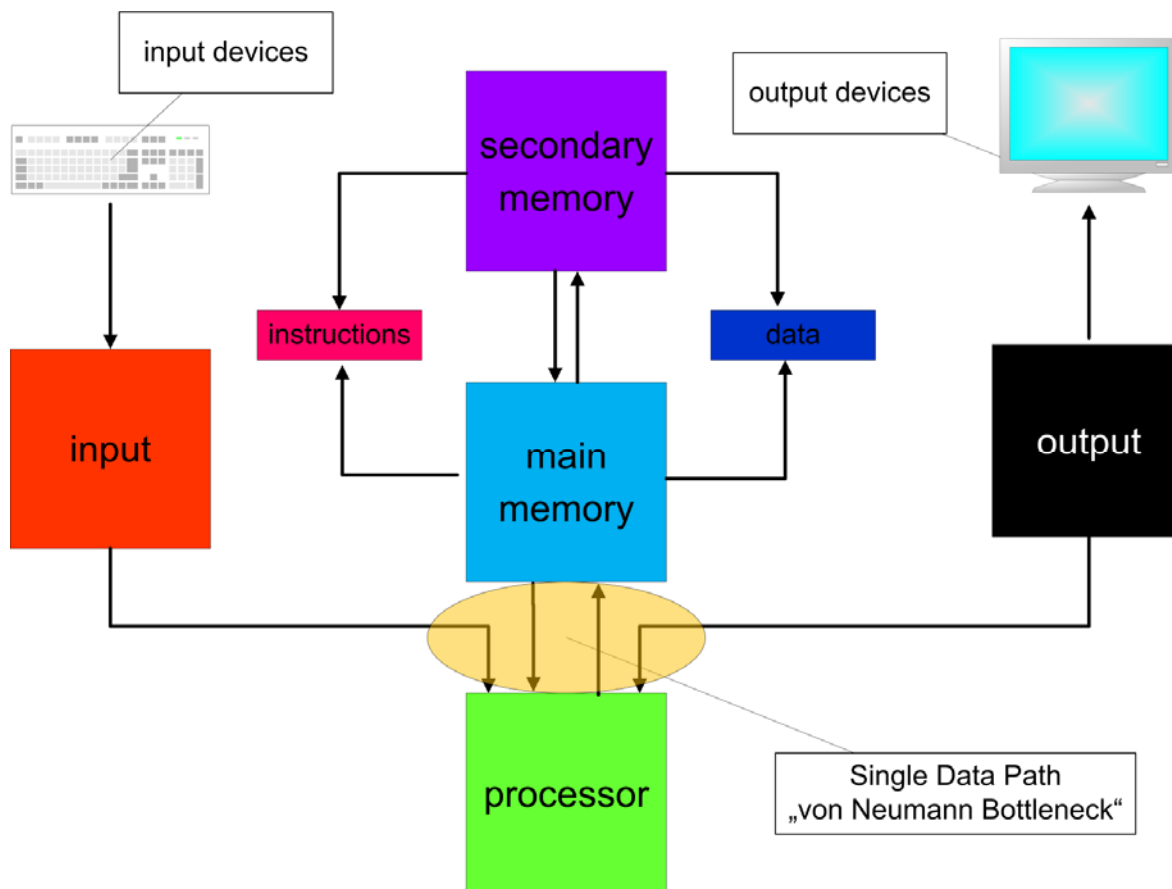


Figure 1-29 The von Neumann Architecture is the reference model for programmable computing machines. The memory contains both data to process and program instructions to execute. This architecture was revolutionary in times where the program was either hard-wired or present in the form of punch cards. This architecture is the foundation for most known computers today. The interconnection system is called bus and forms the von Neumann Bottleneck.

Another technique to speed up computations without increasing clock speed is so called vector computing. While a regular instruction like an addition or multiplication usually only affects scalars, vector registers and vector instructions were introduced that perform the same operation on multiple scalars or on vectors within one clock cycle.

1.8.5 If you can't have a faster CPU use more of them

Using more than one CPU within one computer is less trivial than it sounds. All of the other components such as RAM and busses have to be fit for multiple CPU demands. All theoretically explored or practically established computer architectures can be classified by Flynn's taxonomy (Flynn 1972). Here the given number of instruction streams and data streams classifies architectures (See Figure 1-30). The classical von Neumann approach belongs to the class of single instruction stream, single data stream (SISD) architectures. All

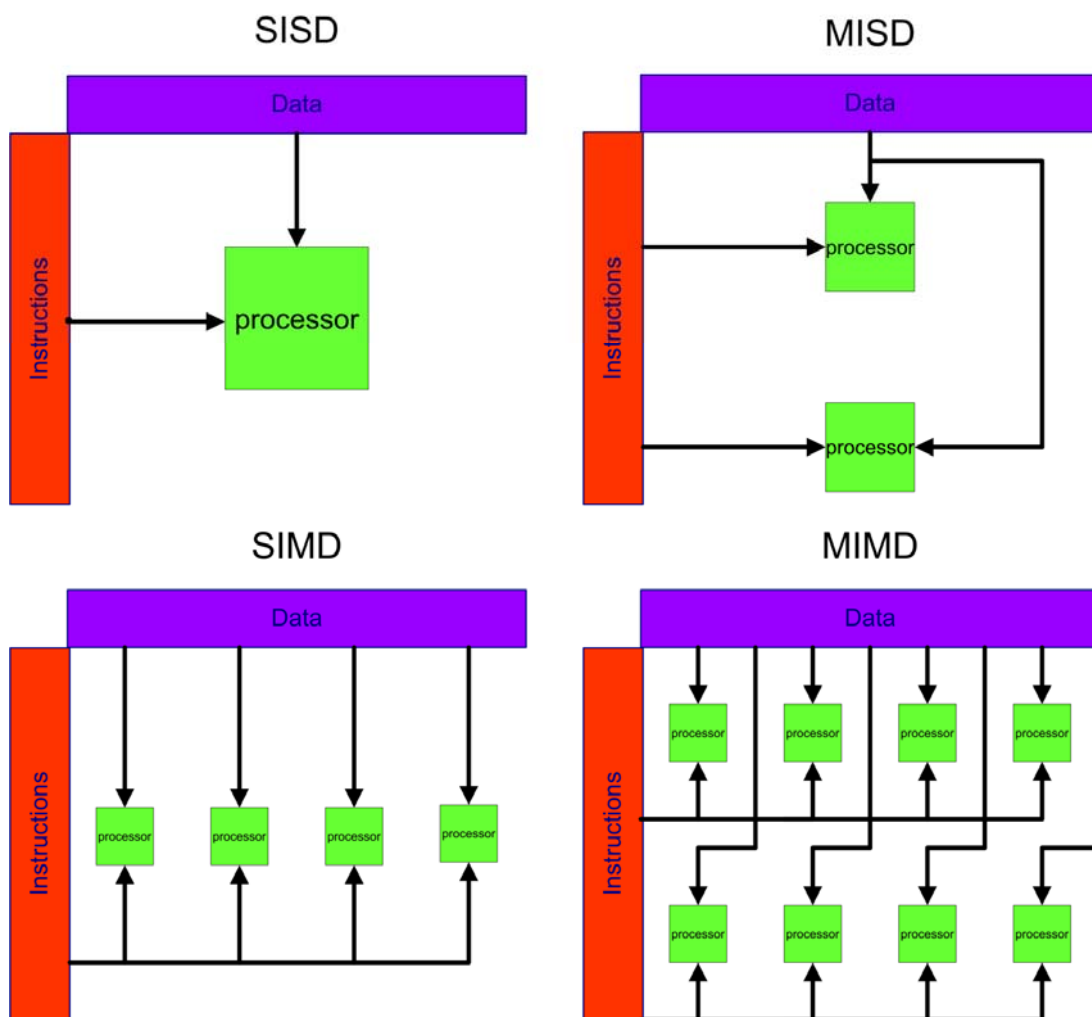


Figure 1-30 Flynn's Taxonomy classifies computing architectures by the given number of instruction and data streams. The number of processing elements can exceed the number shown in the figure except for the SISD case. SISD is the classical von Neumann architecture and the classic single processor system. SIMD computers are also known as array or vector-computers executing the same instruction on a vector of data elements. Examples for MIMD are either local shared memory system or distributed systems where several processors execute different instructions on different data streams. MISD is more theoretical; it can be used for redundant calculations on more than one data stream for error detection.

other architectures combine many von Neumann building blocks. The first class of hardware exploiting parallelism and concurrency were hardware shared memory machines. This means more than one CPU resides inside the same physical machine, working on the same-shared

memory. Most common today are the Single Program, Multiple Data streams (SPMD) architecture where multiple autonomous processors simultaneously execute the same program at independent points, rather than in the lockstep that Single Instruction, Multiple Data (SIMD) imposes on different data. SPMD is, also referred to as Single Process, Multiple Data, which is still the most common style of parallel programming especially for shared memory machines within the same hardware node. Another common approach is the Multiple Program, Multiple Data (MPMD) model where multiple autonomous processors simultaneously run independent programs. Typically such systems pick one node to be the "host" ("the explicit host/node programming model") or "manager" (the "Manager/Worker" strategy), which runs one program that farms out data to all the other nodes which all run a second program. Those other nodes then return their results directly to the manager.

1.8.6 Shared memory computing

Extensive research was performed on exploiting different computer architectures in the past. The main paradigm here is so called shared memory (SM) computing where many CPUs share the same RAM. This approach can further be divided into symmetric multiprocessor (SMP) systems. In this case the memory address space is the same for all the CPUs, and so called non-uniform memory access (NUMA) where every CPU has an own address space results in local memory being accessible faster than remote memory.

1.8.7 Farming

The next logical step is to scale out to many physical computers, so called nodes. This technique is also known as farming. Farming is not really stand-alone hardware architecture but a way of clustering several computers, called nodes, to simulate NUMA architecture by passing messages between individual nodes across a network connection using a number of different approaches. Dedicated, homogeneous clustering combines a fixed number of nodes of the exact same hardware and thus computational power that are dedicated for the cluster computations. Here, every computational node can be trusted to be permanently available, to have the same processing resources and that all nodes are connected via high speed networking to enable point to point communication. The other extreme is a completely heterogeneous, non-dedicated environment, where no resource can be trusted to be available and communication is only possible between individual nodes and a managing server or master node. The most prominent examples for the latter are projects like SETI@Home or Folding@Home using BOINC framework (Anderson 2004) from the realm of volunteer computing.

1.8.8 GPU computing

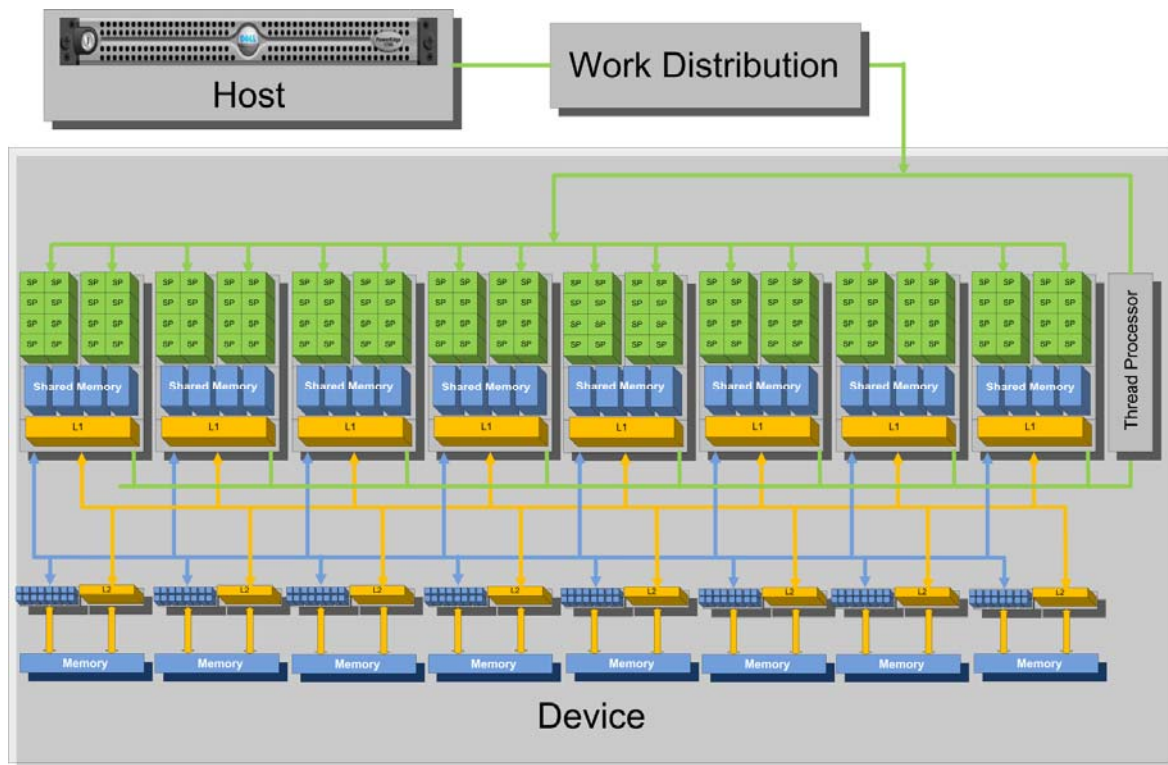


Figure 1-31 Example of a modern GPU Hardware Architecture. (Modified from (Luebke 2008).) The von Neumann Bottleneck formed by a single memory interface is eliminated. Each green square represents a scalar processor grouped within an array of streaming multiprocessors. Memory is arranged in three logical levels. Global memory (the lowest level in Figure) can be accessed by all streaming multiprocessors through individual memory interfaces. Different types of memory exist representing the CUDA programming model: thread-local, intra-thread-block-shared, and globally shared memory. This logical hierarchy is mapped to hardware design. Thread local memory is implemented in registers residing within the MP, which are mapped to individual SP's (not shown). Additionally, dynamic random access memory (DRAM) can be allocated as private local memory per thread. Intra-thread block-shared memory is implemented as a fast parallel data cache, integrated in the multiprocessors. Global memory is implemented as dynamic random access memory (DRAM), separated in read only and read/write regions. Two levels of caching accelerate access to global memory. L1 is a read only cache that is shared by all SP's and speeds up reads from the constant memory space L2 that is a read only region of global device memory. The caching mechanism is implemented per multiprocessor to eliminate von Neumann Bottleneck. A hardware mechanism, the SIMT controller for the creation of threads and the context switching between threads (work distribution), makes the single instruction multiple threads – SIMT approach feasible. Currently up to 12K threads can be executed with virtually no overhead.

Apart from the Multicore Revolution (Herlihy and Luchangco 2008), the Graphical Processing Units (GPU) recently became more than hardware for displaying graphics but a massive parallel processor for general purpose computing (Buck 2007b). Most observers agree that the GPU is gaining on the CPU as the single most important piece of silicon inside the PC. Moore's law that states that computing performance doubles every 18 months for CPUs is cubed today, for GPUs. The reason GPUs beat Moore's Law and will continue to beat Moore's law is the fact that CPUs follow the von Neumann hardware model. The architecture of a single GPU compute unit has a completely different structure, which is called a stream processor in super computing (See Figure 1-31). Multiple stream

processors get their input from other stream processors via dedicated pipes. Concurrent input/output (IO) is history on the chip and there is no waiting for data to process. Moore's law also lags the speed at which silicon gets faster by a considerable margin. With today's advanced fabrication processes, the amount of transistors on a chip doubles every fourteen months. Additionally, the processing speed is doubled about every twenty months. Combined with architectural or algorithmic content a doubling of speed occurs every six months for GPUs. The hardware architecture of the GPU is designed to eliminate von Neumann bottleneck by devoting more transistors to data processing. Every stream processor has an individual memory interface. Memory access latency can additionally be hidden by calculations. The same program can thus execute on many data elements in parallel, unhindered by a single memory interface. The GPU is especially suited for problems that can be expressed as data parallel computations, where the same program is executed on many data elements in parallel with high ratio of arithmetic operations over global memory operations. Because of the parallel execution on multiple data elements, there is low requirement for flow control. Algorithms that process large data sets that can be treated in parallel can be sped up. Algorithms that cannot be expressed in parallel, especially those relying on sophisticated flow control, are not suitable for GPU processing.

1.8.9 Historical - Limitations alleged by Amdahl's law

Until the 1990s everything but the single instruction stream approach was mostly scientific and experimental because even the scaling capabilities of embarrassingly parallel applications were thought to be limited by Amdahl's law (Amdahl 1967) (Figure 1-32). This law seemed like a fundamental limit on how much concurrent code can be sped up. Applied to parallel computing, this law describes the change of total speedup, given different numbers of processing cores. Following Amdahl's conclusion, the theoretical maximum speedup is limited by the portion of the program that cannot be made parallel (i.e. the serial part). If p is the amount of time spent (by a serial processor) on parts of the program that can be computed in parallel, the maximum speed up using N processing cores is:

$$speedup_{Amdahl} = \frac{1}{s + \frac{p}{N}}, \text{ where } s = 1 - p, \text{ assuming a total execution time of 1. Briefly, this}$$

law renders the usage of ever increasing numbers of processors useless, as soon as p is significantly smaller than 1. If for example p is 0.95 then (s) is 0.05 and the maximum speed up that theoretically could be achieved is limited to 20 (even with an infinite number of processors).

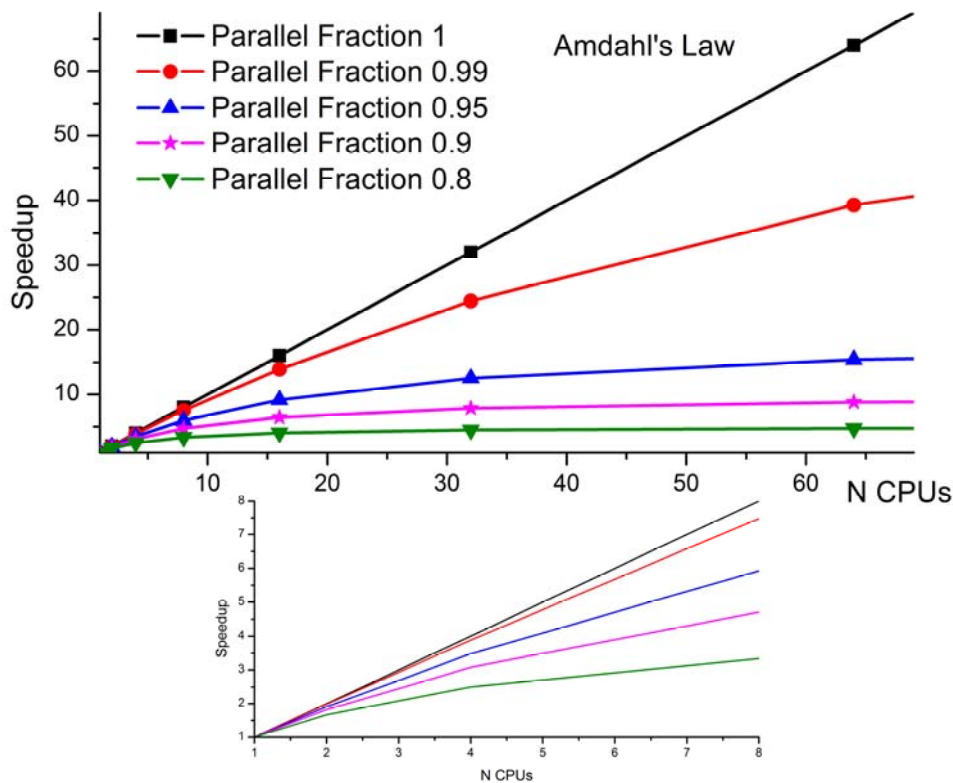


Figure 1-32 Amdahl's law (established in 1967) seemed to be a fundamental limit on the maximum speed up or performance gain achievable by parallelization of an algorithm to multiple CPUs. The fraction of parallelizable code drives this law. The law was formulated under the assumption of fixed problem size. This assumption means that the ratio between serial and parallel code fraction is constant. Under this assumption the efficiency of parallelization is constantly decreasing with growing number of CPUs. In the range between 2 and 8 CPUs until recently this was still accepted. But when increasing the problem size while not linearly increasing the serial fraction of the algorithm, Amdahl's law has to be re-evaluated and a much higher, scalable speedup or performance gain can be achieved.

Fortunately, this law does not hold true in practice, mainly because the implicit assumption that p is independent of N is often violated. In practice, the problem size is often scaled with N . The s component itself consists of multiple parts. On the one hand, the amount of time spent on program startup, serial bottlenecks, etc., which contributes to the s component, does not necessarily grow linearly with problem size. On the other hand, the communication between and synchronization of multiple processors (parallelization overhead), also making up part of s , usually does increase with N . Thus increasing the problem size for a given runtime effectively results in an increased value for p . Based on the assumptions of constant runtime (not problem size) and lack of parallelization overhead, Gustafson states that the total speedup of a parallel program is given by Gustafson-Barsis law: $scaledspeedup_{Gustafson} = N + (1 - N)s$ (Gustafson 1988) (See Figure 1-33). As N increases to infinity, the total work that can be accomplished also increases to infinity. Amdahl's law can be considered as the lower- and Gustafson-Barsis law as the upper-

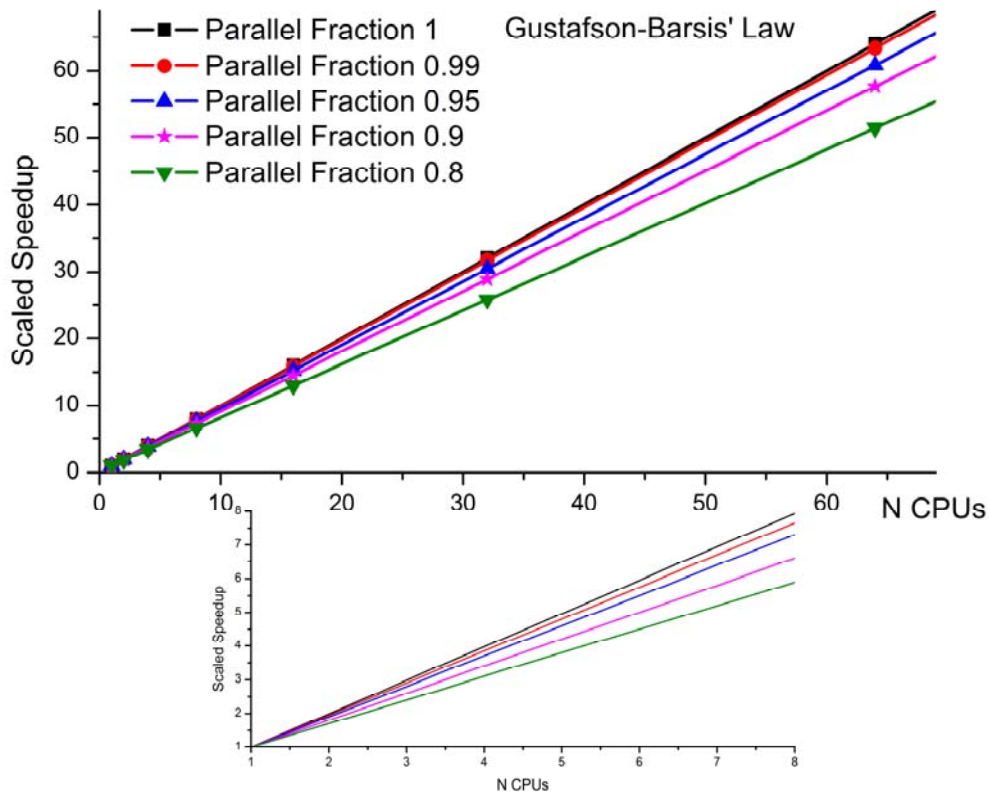


Figure 1-33 Scaled speedup predicted by Gustafson-Barsis law. Gustafson argued that the sequential portion of a problem is not fixed and does not necessarily grow with problem size. For example, if the serial phase is only an initialization phase and the main calculations can run independently in parallel; By increasing the problem size the sequential fraction can effectively be reduced to get a much larger speedup than predicted by Amdahl's law.

speedup-boundary. Depending on the problem itself, its implementation, and the hardware infrastructure used, the effective speedup will lie somewhere between Amdahl's and Gustafson's predictions. The bigger the size of the problem, the closer the speedup will be to the number of processors.

1.8.10 Data parallel programming

Traditional parallel programming methods often have limited scaling capabilities. The serialization and de-serialization phases required produce a linear growth in serial code if each core has to synchronize with a single core. For point-to-point synchronization between multiple cores, the overhead can even increase as a combinatorial of core count. To prevent future core counts from exceeding the level of parallelism an application can scale to, meaning having more processing cores than threads, a paradigm which scales with core count without the need of restructuring existing code would be very useful. Therefore, a finer level of granularity has to be identified for parallelism. In the near future the only type of element that will be available in the same amounts as cores will be data elements (Boyd 2008). Therefore the data parallel approach looks for fine-grained inner loops within each

computational step and parallelizes those with the goal of having one logical core for processing each data element. Ideally, this should take place automatically by the combination of the compiler and the runtime system. There are several programming languages or language extensions to do this such as High Performance Fortran or Co-Array, but these hide unique aspects of data parallel programming or the processor hardware. Array based languages such as Microsoft Research Accelerator (Tarditi, Puri et al. 2005; Tarditi, Puri et al. 2006) need a very high level of abstraction and are rarely portable or even available for more than one specific platform. The graphics hardware manufacturers involved are developing new data parallel languages for their individual hardware ATI: CAL , Brook+ (Hensley 2007); NVIDIA: CUDA (Nickolls, Buck et al. 2008). The syntax of these languages provides a direct mapping to hardware that enables specific optimizations and access to hardware features that no other approach allows. The main disadvantage is once again the dependency on the (graphics-) platform until hardware and operating system manufacturers eventually agree on a unified application programmer's interface (API) for GPUs which might even become available within the near future. For Microsoft Windows systems, proprietary due to the introduction of DirectX 11 featuring compute-shaders (an API for GPU computing independent of the hardware manufacturer) and additionally, a completely new C/C++ extension called BSGP that has just recently been released (Hou, Zhou et al. 2008). These systems can create and execute parallel kernels graphics hardware independently for all operating systems due to OpenCL (Munshi 2008). Another option might be MCUDA, a CUDA extension that can efficiently run CUDA kernels on any given multicore hardware (Stratton, Stone et al. 2008).

1.9 Change your code

1.9.1 Software standards for shared memory and distributed computing

None of the previously mentioned architectures will speed up any algorithm that is not designed to benefit from concurrent hardware as it is the case for most scientific applications. Generally speaking, extra layers of programming code are needed for the synchronization and communication of many cores or CPUs within one physical computer, the synchronization and communication of different nodes among each other, and last but not least for using parallel co-processors like GPUs.

In practice, for any kind of shared memory programming a reliable locking infrastructure is necessary to prevent uncontrolled concurrent access to the same data. Otherwise, memory conflicts will arise that will lead to deadlocks or race conditions. For example if a shared

counter value is increased, it has to be read first. The new now increased value has to be computed and then finally written back to the shared memory location. If this is allowed concurrently, unpredictable results will occur, termed race conditions, because the task of increasing is not "atomic". It consists of three operations that must not be interrupted. Locking the counter until the whole task is completed can prevent race conditions. This may lead to dead locks where one task waits for the other and vice versa. The programmer thus needs to rely on combinations of "locks" and conditions such as "semaphores" or "monitors" to prevent concurrent access on the same-shared data. This approach enables the developer to treat sections of code as "atomic", uninterruptible instructions to simplify reasoning about instruction interactions.

One of the shortcomings is the decision whether coarse-grained locking or fine-grained locking should be used is totally up to the developer. Coarse-grained locking means that a single lock protects a whole data structure. This is simple to implement but permits little or no concurrency. By contrast fine-grained locking, where a lock is associated with each component of the data structure is complicated to implement and might lead to larger parallelization overhead. The best possible solution will only be valid for a single problem and hardware, making it very difficult to write scalable and portable code at the same time. Fortunately, there are various subtle non-blocking algorithms for standard problems and data structures (Herlihy 1991). These facilitate standard applications without the risk of dead locks or race conditions.

Another paradigm that entered distributed computing is termed transactional memory approach (Herlihy and Moss 1993). Here the possible clashes of shared memory computing are overcome by the so-called transaction paradigm that is originated in the field of database system design. It enables the developer to mark a designated region of code as a transaction that is then executed atomically by a part of the system. A distributed transaction controller is in control of locks, monitors and semaphores. A transaction that cannot be executed is rolled back and its effects are discarded. The underlying system will probably also use locks or non-blocking algorithms for the implementation of transactions, but the complexity is encapsulated and remains invisible to the application programmer.

For the different levels of concurrency, industry standard solution libraries exist. For shared memory computing within one node today's de facto standard is Open Multi Processing or OpenMP (Dagum and Menon 1998) which is a framework for parallelization of C/C++ and Fortran at compiler level. It allows the programmer to mark sections as parallelizable. The

compiler and runtime will then be able to unroll a loop and distribute it across given CPUs or cores for parallel execution. For message passing between nodes there is also a de facto standard, which is called message passing interface (MPI) (Park and Hariri 1997). This is a fast method for copying data between computational nodes or aggregating results from computational nodes. MPI's predecessor with common goals was PVM: Parallel Virtual Machine (Beguelin, Dongarra et al. 1991). Of course, MPI and OpenMP can be mixed to parallelize across multiple CPUs within multiple nodes (Smith and Bull 2001). For the programming of GPUs, several frameworks exist that differ regarding the hardware manufacturer of the GPU used.

1.9.2 Software standards for GPU programming

As already mentioned, the GPU by now is a massive Multicore parallel or streaming processor and can be used for general purpose computing. Especially in image processing and 3D reconstruction, a tremendous amount of effort was spent to speed up common problems (Bilbao-Castro, Carazo et al. 2004) and by now several libraries exist that exploit parallel processing features for common tasks. The most prominent example is the discrete Fast Fourier transformation (FFT) that can by now be sped-up up to 40 times on the GPU in comparison to CPUs (Govindaraju, Lloyd et al. 2008). An illustrative summary of performance gain on image processing algorithms that will be especially interesting for crystallographers can be found in (Castaño-Díez, Moser et al. 2008). In the early days programming the GPU meant, “abusing” graphics primitives for general purpose computing (Moreland and Angel 2003). Since GPUs are originally peripheral devices, computations have to be initialized and controlled by the device driver software (Mark, Glanville et al. 2003) and the graphics hardware producer defines the application programmer interfaces (Pharr and Fernando 2005). Since today's graphics card market consists of mainly two companies, ATI and NVIDIA, there are unfortunately two frameworks depending on the GPU brand used. NVIDIA: CUDA (Buck 2007a) ATI: CTM/Brook+ (Hensley 2007). In the future a standard interface for using the GPU for general-purpose computations will hopefully be part of the operating system, or compilers will be able to generate the necessary code automatically as it is done with OpenMP language extensions. Apple announced that its next operation system will support OpenCL, a C/C++ extension similar to CUDA as an essential building block which facilitates execution on any given multicore CPU or GPU hardware, in 2009 (Munshi 2008). OpenCL will also be available as an open standard for other platforms including Linux and Windows. Additionally, Microsoft Research, also steering towards hardware independent solutions recently conveyed a parallel programming

language called BSGP that is likely to replace graphics hardware manufacturer-dependent solutions at least for the Windows platform (Hou, Zhou et al. 2008). Another break from hardware dependency might also be MCUDA (Stratton, Stone et al. 2008) which also enables code written for the graphics hardware to be efficiently executed on any given multicore hardware.

1.10 Aim of the work

The most promising method to investigate the 3D structure of large macromolecular assemblies today is cryo EM in combination with single-particle 3D image processing. For analysis of heterogeneous samples due to dynamic or biochemical conformational changes, conformational heterogeneity has to be recognized and the data has to be split up to allow for snapshot analysis of dynamic processes. The computational tools for dealing with conformational heterogeneity are just now emerging. Especially, methods for generation of reliable 3D starting models representing conformational states are basically lacking. Additionally, mechanisms to process very large data sets necessary for image data to be split up in subsets representing different conformational states are needed. The work presented here aimed at speeding up established image processing algorithms used in EM by state of the art hardware and software paradigms. Additionally, methodical improvements had to be established to make computation of new 3D starting models of dynamic asymmetrical macromolecules more reliable and allow for determination of conformational differences. The results chapter is therefore divided into three parts. In the first part, the 3D structure of Acetyl-CoA Carboxylase from *Cornyebacterium glutamicum* - which proved to be an extremely heterogeneous sample - obtained using established EM methods, is presented. In the second part, methodical developments to prepare EM image processing algorithms to exploit the full power of state of the art parallel and distributed computing techniques are presented. Finally, in the third part, a newly developed method for processing of projection images and computation of reliable, missing cone free starting models, representing different conformational states in the specimen is presented.

2 Materials and methods

2.1 Software

Software	Source
TVIPS EM-MENU	Tietz Video System, Gauting, Germany
IMAGIC-5 (single-particle analysis)	Image Science, Berlin, Germany
AmiraDev 4.1	TGS Europe, Merignac Cedex, France
Visual Studio 2005	Microsoft Corporation, Redmond, WA, USA
Visual Studio 2008	Microsoft Corporation, Redmond, WA, USA
SQL Server 2005	Microsoft Corporation, Redmond, WA, USA
BOXER from EMAN Suite	(Ludtke, Baldwin et al. 1999)

Table 2-1 Software used within this thesis.

2.2 Biochemical methods

2.2.1 Chemicals

Chemical	Source
Adenosintriphosphat (ATP)	Amersham Biosciences, Piscataway, NJ, USA
Acetic acid ethyl ester, Ultrapure grade	Fluka-Riedel-de-Haen, Seelze, Germany
Acetyl Coenzyme A Sodium Salt	Sigma-Aldrich, Seelze, Germany
“Complete” Protease Inhibitor Cocktail	Roche, Mannheim, Germany
Dithiothreitol (DTT)	Roth, Karlsruhe, Germany
Ethylenediaminetetraacetic acid (EDTA)	Sigma-Aldrich, Seelze, Germany
Ethanol	Merck, Darmstadt, Germany
Glutaraldehyde	Electron Microscopy Sciences, Hattfield, PA, USA
Glycerol	Merck, Darmstadt, Germany
HEPES	Sigma-Aldrich, Seelze, Germany
Histidine	Sigma-Aldrich, Seelze, Germany
Hydrofluoric acid	Fluka-Riedel-de-Haen, Seelze, Germany
Imidazole	Sigma-Aldrich, Seelze, Germany
Magnesium chloride	Merck, Darmstadt, Germany
Millipore water	Millipore GmbH, Schwalbach, Germany
osvan solution (alkylbenzyltrimethylammonium 0.5%)	Sigma-Aldrich, Seelze, Germany
Sodium chloride	Merck, Darmstadt, Germany
Triafol (acetobutyrate cellulose)	Sigma-Aldrich, Seelze, Germany
Uranyl formate	Polyscience Inc., Warrington, PA, USA

Table 2-2 Chemicals used within this thesis.

2.2.2 Buffers and solutions

Solution	Composition
ACo Lysis Buffer 1	50 mM HEPES pH 8.0, 150 mM NaCl, 2.5 mM MgCl ₂ , 0,5 mM DTT, 5 mM ATP
ACo Equilibration Buffer 1	50 mM HEPES pH 8.0, 150 mM NaCl, 2.5 mM MgCl ₂ , 0,5 mM DTT, 5 mM ATP, 10 mM Imidazole
ACo Wash Buffer 1	50 mM HEPES pH 8.0, 150 mM NaCl, 2.5 mM MgCl ₂ , 0,5 mM DTT, 5 mM ATP, 20 mM Imidazole
ACo Elution Buffer 1	50 mM HEPES pH 8.0, 150 mM NaCl, 2.5 mM MgCl ₂ , 0,5 mM DTT, 5 mM ATP, 150 mM Imidazole
ACo Lysis Buffer 2	50 mM HEPES pH 7.5, 150 mM NaCl, 1 mM CoA Sodium Salt, 1 tablet "Complete" / 50 ml, 0.1 mM EDTA
ACo Equilibration Buffer 2	50 mM HEPES pH 7.5, 150 mM NaCl, 1 mM CoA Sodium Salt, 1 tablet "Complete" / 50 ml, 10 mM Histidine, 0.1 mM EDTA
ACo Wash Buffer 2	50 mM HEPES pH 7.5, 150 mM NaCl, 1 mM CoA Sodium Salt, 1 tablet "Complete" / 50 ml, 20 mM Histidine, 0.1 mM EDTA
ACo Elution Buffer 2	50 mM HEPES pH 7.5, 150 mM NaCl, 1 mM CoA Sodium Salt, 1 tablet "Complete" / 50 ml, 150 mM Histidine, 0.1 mM EDTA
Grafix Buffer 1	50 mM HEPES pH 7.5, 150 mM NaCl, 10 % Glycerol, 0,05% Glutaraldehyde
Grafix Buffer 2	50 mM HEPES pH 7.5, 150 mM NaCl, 30 % Glycerol, 0,5% Glutaraldehyde
ACo Cryo Buffer	50 mM HEPES pH 7.5, 150 mM NaCl

Table 2-3 Buffers and solutions used within this thesis.

2.2.3 Laboratory materials

Item	Source
Carbon rods, highest grade	Ringsdorff Werke GmbH, Bonn, Germany
Copper EM grids, 3.05 mm, 300 mesh, square	Plano, Wetzlar, Germany
Ethane (liquid)	Messer, Sulzbach, Germany
Filter paper 90 mm, No. 4 and 5	Whatmann, Dassel, Germany
Glass slides (76 x 26 mm)	Gerhard Menzel GmbH + Co. KG, Braunschweig, Germany
Mica, 75 x 25 mm	Plano, Wetzlar, Germany
Nitrogen (liquid)	Messer, Sulzbach, Germany
Teflon preparation block (volume: 25µl – 200µl)	Manufactured by the precision engineering team, MPI Göttingen
Ni-NTA Superflow Columns (1.5 ml)	Quiagen, Hilden, Germany
Gelfiltration Column HiLoad 26/60 Superdex 200 prep grade	Amersham Pharmacia Biotech, Freiburg, Germany

Table 2-4 Laboratory materials used within this thesis.

2.2.4 Special equipment

Item	Source
Cryo electron microscope CM200 FEG	Philips, Eindhoven, The Netherlands
TemCam F415 (slow scan 4K x 4K CCD camera)	Tietz Video Systems, Gauting, Germany
Room temperature EM specimen holder	Philips, Eindhoven, The Netherlands
Cryo EM specimen holder	Gatan GmbH, München, Germany
Sorvall Ultracentrifuge Discovery 90	Thermo Electron, Langenselbold, Germany
Sorvall Centrifuge Evolution RC	Thermo Electron, Langenselbold, Germany
Sorvall Rotor SA-300	Thermo Electron, Langenselbold, Germany
Sorvall Rotor TH660	Thermo Electron, Langenselbold, Germany
Peristaltic Pump LKB-Pump P-1	Amersham Pharmacia Biotech, Freiburg, Germany
Fraction Collector FRAC-200	Amersham Pharmacia Biotech, Freiburg, Germany
Chart Recorder Bromma 2210	Amersham Pharmacia Biotech, Freiburg, Germany
Heraeus Desk Centrifuge Biofuge Fresco	Heraeus Sepatech GmbH, Osterode, Germany
Digital Sonifier W-250 D	Branson, Danbury, CT, USA
Microtip Sonode	Branson, Danbury, CT, USA
Centrifuge Tubes	Beckmann, Palo Alto, CA, USA
Windows computer cluster consisting of 32 computer nodes of the following configuration:	Sysgen GmbH, Bremen, Germany
Mainboard Tyan Thunder S2877G2NR	
-2x AMD OPTERON 270 2.0 GHz, Dual Core	
19" Rackmount-Case: Chenbro RM117-02, 1HE	
-400 Watt Power Supply EPS P1M-6400P	
-2GB Memory, Kingston DDRAM / PC400	
(4x512MB) ECC reg.	
-80GB Harddisk Seagate BARRACUDA 7200.7	
7200 rpm	
Graphics Board Nvidia Quadro FX 450	PNY Technologies Europe, Mergnac Cedex, France
Dekstop Computer Dell Dimension 8400	Dell GmbH, Frankfurt, Germany
FPLC System ÄKTA Explorer 100	Amersham Pharmacia Biotech, Freiburg, Germany
Molecular Weight Gel Filtration Kit	Amersham Pharmacia Biotech, Freiburg, Germany
Pierce Centrifuge Column (0.8 ml)	Thermo Fisher Scientific Inc., Rockford, IL, USA

Table 2-5 Special equipment used within this thesis.

2.2.5 Bacterial samples and plasmids

Strain or plasmid	Relevant characteristic or use	Reference or source
<i>C. glutamicum</i> strains		
Δ pyc strain	<i>C. glutamicum</i> deleted of biotinylated pyruvate carboxylase	(Peters-Wendisch, Schiel et al. 2001)
Δ pyc paacBC p-H6D1 strain	<i>C. glutamicum</i> Δ pyc with pJC1accBC and pEKEEx3-H6D1	(Tilg 2002)
Plasmids		
pJC1accBC	Over expression of biotinylated α -subunit	(Jager, Peters-Wendisch et al. 1996)
pEKEEx3-H6D1	Over expression of H6-accD1	(Gande 2005)

Table 2-6. Bacterial samples and plasmids used within this thesis. All samples were kindly provided by Prof. L. Eggeling, Jülich.

C. glutamicum strain Δ pyc paacBC p-H6D1 was kindly provided by Prof. L. Eggeling, Institute for Biotechnology, Research Center Juelich. The base strain Δ pyc is devoid of the nonessential pyruvate Carboxylase representing, besides AccBC, the second biotinylated protein present in this bacterium (Jager, Peters-Wendisch et al. 1996). The strain Δ pyc paacBC p-H6D1 used for co-over-expression of AccBC-AccD1 and thus Acetyl-CoA Carboxylase complex additionally introduces a His-tag to the biotinylated α -subunit AccBC for affinity purification.

2.3 EM imaging conditions



Figure 2-1 Cryo microscope CM200 FEG, Philips, Eindhoven, The Netherlands.

Magnification	Post Magnification	Effective Magnification
88000	1.4	123200
115000	1.4	161000

Table 2-7 Magnification settings used for recording of data sets with the Philips CM 200 FEG.

Magnification	Δ Mag [%]	Δ post-mag [%]	Δ effective Mag
88000	2	2.86	5984
115000	2	2.86	7820

Table 2-8 Magnifications errors for magnifications from Table 2-7 resulting from post magnification error and intrinsic microscope magnification error (manufacturer information).

TemCam F415 (slow scan 4K x 4K CCD camera)

Effective Mag	CCD Pixel Size [Å]	pixel size specimen level (2x2 binning) [Å]	Δ pixel size specimen level 2x2 binning [Å]
123200	150000	2.44	0.12
161000	150000	1.86	0.09

Table 2-9. Effective magnifications resulting from Table 2 7 in combination with the used detector TemCam 415.

All EM exposures were recorded using an acceleration voltage of 160 kV at low dose conditions with the electron dose adjusted to $\sim 20 \text{ e } \text{Å}^{-2}$. The electron dose was kept constant by adjustment of exposure times in the range of 300-500 ms resulting in an average detector electron count of 8000. The under focus range used for exposures was 1.2 – 3.0 μm .

2.4 Preparation of EM samples

2.4.1 Preparation of holey carbon film coated EM grids

Copper EM grids, 3.05 mm, 300 square meshes, were coated with a holey carbon film by Prakash Dube. Light microscopy object slides were cleaned with ethanol and incubated in osvan solution. The now hydrophobic slides were immersed into Millipore water and removed avoiding residual water on the surface. By incubation in an atmosphere of increased air humidity on a cooled aluminum block, condensation of small water droplets was induced before 1ml of triafol in acetic acid ethyl ester (0.5%) was applied on the microscopic slides. After evaporation of acetic acid ethyl ester, a thin triafol film, featuring small holes where water droplets condensed before, remained on the glass slides. By immersion of the slides in hydrofluoric acid for 30 seconds, the triafol film was detached from the slides and then floated on Millipore water. Continuous carbon film was obtained by direct carbon coating of freshly cleaved mica by vacuum evaporation.

2.4.2 Preparation of EM samples for negative stain electron microscopy

Specimen preparation of negatively stained EM grids was performed following the “sandwich technique” (Valentine, Shapiro et al. 1968; Tischendorf, Zeichhardt et al. 1974; Kastner 1998) as illustrated in Figure 2-2. A carbon film evaporated on freshly cleaved mica was floated on a well of a Teflon preparation block containing the specimen solution and kept there to allow adsorption of the specimen. The time for the adsorption was dependent on the protein concentration in the specimen solution. Another well of the preparation block

was filled with 2% Uranyl formate staining solution and the carbon film with adsorbed specimen incubated in for 2 minutes. The carbon film now carrying stained specimen was attached to a clean EM copper grid, coated with holey carbon film. Another carbon film floated on another well filled with the staining solution was now mounted on the EM grid, forming a “sandwich”, enclosing the specimen in staining solution enclosed between two carbon films. The high atomic number of the stain surrounding the biological specimen leads to “negative” contrast since sample areas containing specimen will have less Coulomb scattering power than areas containing stain only.

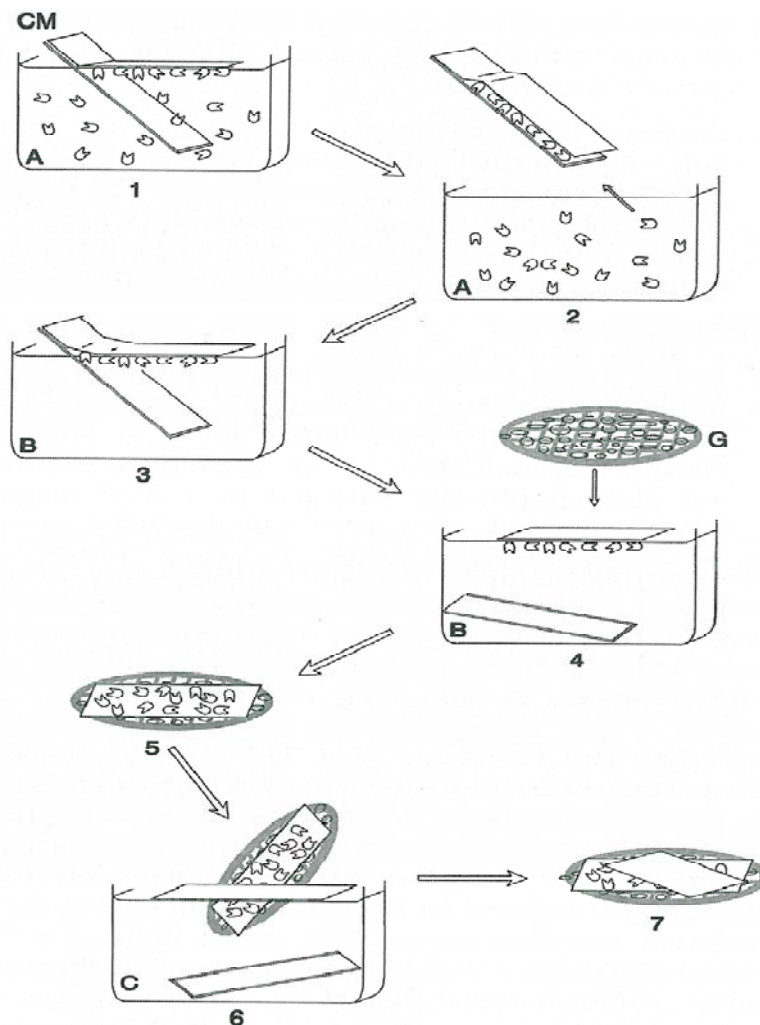


Figure 2-2 Illustration of the "Sandwich" technique for preparation of samples for negative stain electron microscopy. A carbon film evaporated on freshly cleaved mica is floated on a well of a Teflon preparation block containing the specimen solution and kept there to allow adsorption of the specimen (1). The carbon film with adsorbed specimen is incubated in another well of the preparation block, filled with 2% Uranyl formate staining solution (3). The carbon film now carrying stained specimen is attached to a clean EM copper grid, coated with holey carbon film (4). Another carbon film floated on another well filled with the staining solution (6) is now mounted on the EM grid, forming a “sandwich”, enclosing the specimen in staining solution enclosed between two carbon films (7). Figure modified from (Kastner 1998)

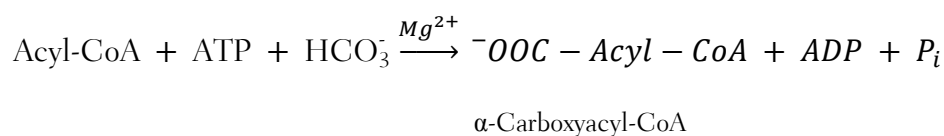
2.4.3 Preparation of cryo EM samples

Preparation of cryo samples was performed following an established method (Adrian, Dubochet et al. 1984). A solution containing the specimen of interest is applied to perforated carbon grids and rapidly frozen in liquid ethane by mounting the specimen grid held by a forceps in a guillotine-like device and dropping it in a container filled with liquid ethane. The specimen grids prepared following this technique were then kept in liquid nitrogen until imaged using the Gatan cryostage also at liquid nitrogen temperature. Cooling down, keeping, and imaging the sample at liquid nitrogen temperature (~ 110 K) reduces the damage caused by electron irradiation significantly (Stark, Zemlin et al. 1996), mainly because the mobility and speed of reaction of free radicals generated by ionization within the specimen is reduced. Additionally, when using perforated grids, the particles embedded in vitreous ice only, do not bind to a carbon support layer and thus are thought to be more randomly oriented. Additionally, artifacts resulting from negative stain preparation, caused by staining, drying and flattening by sandwiching between two carbon films are eliminated (Taylor and Glaeser 1974). For cryo preparation the requirements regarding particle concentration and stability are much higher than for the negative stain approach.

3 Results

3.1 Towards 3D structure determination of Acetyl-CoA Carboxylase from *Corynebacterium glutamicum*

Acyl-CoA Carboxylases catalyze the irreversible carboxylation of Acyl-CoA derivatives e.g. Acetyl-CoA into Malonyl-CoA in the presence of ATP and HCO_3^- :



Studies on Acyl-CoA Carboxylases isolated from *M. tuberculosis* (Rainwater and Kolattukudy 1982) and *E. coli* (Wood and Barden 1977; Knowles 1989) revealed Carboxylases to be multi-protein complexes consisting of at least two subunits. The bigger α -subunits (~88 kDa) of all known Carboxylases carry biotin as a cofactor that is necessary for the reversible binding and transmission of CO_2 (Samols, Thornton et al. 1988; Chapman-Smith and Cronan 1999) while the smaller β -subunits (~66 kDa) have a function in the actual substrate carboxylation (Sutton, Fall et al. 1977; Kondo, Shiratsuchi et al. 1991). While Acetyl-CoA Carboxylase in *E. Coli* consists of 4 subunits (Guchhait, Polakis et al. 1974), the Acetyl-CoA Carboxylase of *C. glutamicum* was thought to consist of only 2 subunits AccD1 and AccBC, when studies on 3D structure started: AccD1 (58.5 kDa) and AccBC (63.4 kDa) with an apparent molecular weight of 714 kDa, making a stoichiometry of $\alpha_6\beta_6$ highly likely (Heseler 2005). By in-vitro enzyme assays with raw extracts of different strains of *C. glutamicum*, synthesis of Malonyl-CoA could be verified based on the discontinual enzyme-test method published in (Kimura, Kojyo et al. 1998). Over-expression of accD1 alone leads to a doubling of specific Acetyl-CoA Carboxylase activity. Co-over-expression of accD1 and accBC together results in a further increase of Malonyl-CoA synthesis by a factor of 8. This property facilitates the conclusion that AccBC in combination with AccD1 forms the Acetyl-CoA Carboxylase complex of *C. glutamicum*. The complex can be stably isolated and is structural and functionally comparable to other Acyl-CoA Carboxylases (Guchhait, Polakis et al. 1974). Thus *C. glutamicum* is an ideal expression system to study the yet unknown 3D structure of such an enzyme.

3.1.1 Purification of AccBC-AccD1 complex from *C. glutamicum* strain Δ pyc paacBC p-H6D1

First EM analysis was performed on AccBC-AccD1 protein solution purified by the protocol used for the discontinual enzyme-test following the method published in (Gande 2005).

A pellet of a volume of 2 ml of bacterial raw extract from Δ pyc paacBC p-H6D1 strain, harvested in the log phase, was resuspended in lysis buffer to a total volume of 7 ml. The suspension was then transferred to a 10 ml beaker which was kept in a 100 ml beaker filled with blue ice. Bacterial cells were lysed by ultrasonification using a total sound duration of 4 min, 20% amplitude and a 15 s sound / 5 s intermission sequence. The raw extract treated by ultrasonification was centrifuged at 15.000 rpm for 30 min for exclusion of large cell fragments and intact cells. The supernatant harvested after centrifugation was further processed by 6xHis-Ni-NTA chromatography (Crowe, Dobeli et al. 1994; Qiagen 2003). Fresh Ni-NTA gravity flow columns with a resin volume of 1.5 ml were cleaned of ethanol by first decanting and then rinsing with 5ml of Millipore water. The columns were subsequently equilibrated using 5 ml of “ACo-Equilibration-Buffer 1”, loaded with raw extract, and washed with 10 ml of “ACo Wash Buffer 1”. For elution, 200 μ l of “ACo Elution Buffer 1” was applied to compensate for the column dead volume, and finally the bound protein was eluted and collected using 1 ml of “ACo Elution Buffer 1”. The eluate was then treated by size exclusion chromatography (Lathe and Ruthven 1955) using a Superdex 200 column, isocratically with a flow of 1.5 ml/min collecting fractions of 3-4 ml, resulting in an

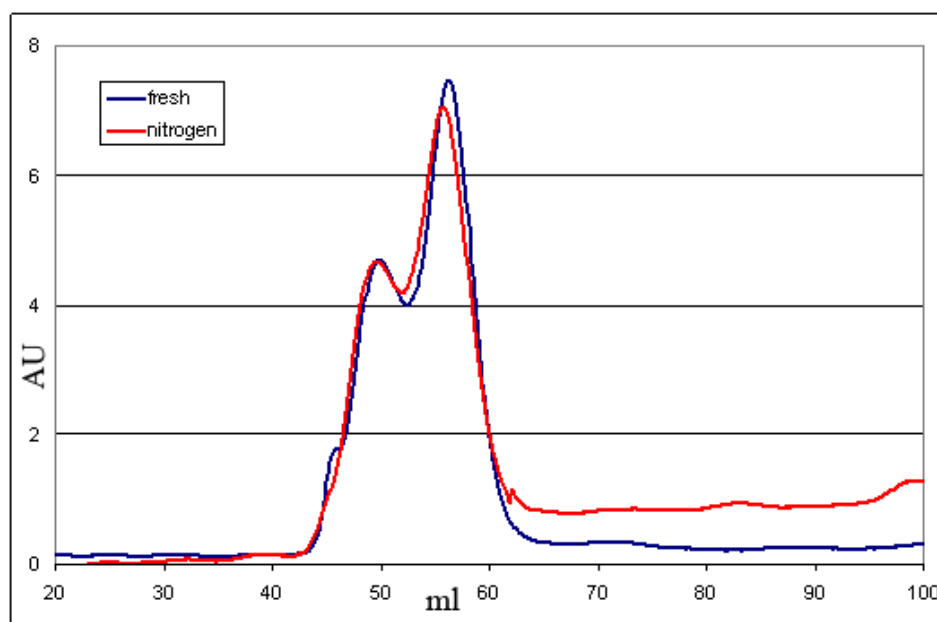


Figure 3-1 Addition of glycerol to the raw extract results in nearly identical profiles for the frozen and the fresh raw extract.

elution profile as depicted in Figure 3-1. The red curve shows the elution profile for fresh raw extract and the blue profile for raw extract that was frozen using liquid nitrogen and then stored at -80° before undergoing size exclusion chromatography. Adjustment of raw extract to a concentration of 5% glycerol, resulted in nearly identical elution profiles for frozen and fresh raw extract as depicted in Figure 3-1. Western Blot analysis (Burnette 1981), enzyme activity tests and molecular weight determination by polyacrylamide gel electrophoresis (Weber and Osborn 1969) in comparison to standard proteins, showed that both the peaks consist of both Acetyl-CoA Carboxylase complex components, but in different stoichiometric amounts. However the shoulder on the right of the main peaks consists of AccD1 hexamers only, without detectable biotinylated component AccBC (Tilg 2002; Gande 2005). Protein concentration in the raw extract, determined by Bradford-assay (Bradford 1976) was in the range of 300-500 ng/ μ l and in the range of 30-50 ng/ μ l in the highest peak fraction.

3.1.2 Negative stain EM of Acetyl CoA-Carboxylase complex AccBC-AccD1

Fractions of size exclusion between 40 and 70 ml were subjected to EM analysis using the negative stain “sandwich” preparation technique as described above. The time for adsorption of specimen to carbon foil was 10 min. Fractions eluting up to \sim 45 ml contained unspecific aggregates (data not shown), peak fractions between 45 and 55 ml proved to contain a mixed particle population consisting of particles of \sim 210 Å along the principal axis length (Figure 3-2). Fractions between 55 ml and 65 ml contained a particle population of \sim 105 Å along the principal axis length (Figure 3-5) and fractions $>$ 65 ml contained smaller globular debris of \sim 50 Å diameter. Peak fractions containing proteins of \sim 210 Å longest principal axis lengths were further analyzed. Image data sets were recorded on CCD camera by the spot scanning technique (Downing 1991) with 5x5 spots using imaging conditions, as described in section 2.3, and the particles were extracted. Data sets consisting of 5165 – 15900 extracted particle images were subjected to 2D de novo analysis as described in chapter 1.4.5. After 4-6 rounds of the “reference-free” alignment scheme as described in section 1.4.5, in combination with exhaustive MRA via resampling to polar coordinates (compare section 1.4.3), class sums consisting of \sim 30 class members were computed. Subsequently, an increasing number of class sums was manually selected for further processing and used as references in a new round of exhaustive MRA followed by another round of MSA, finally resulting in 50 class averages, 44 of which are depicted in Figure 3-3. On spot scan level a homogeneous protein size seems to be present.

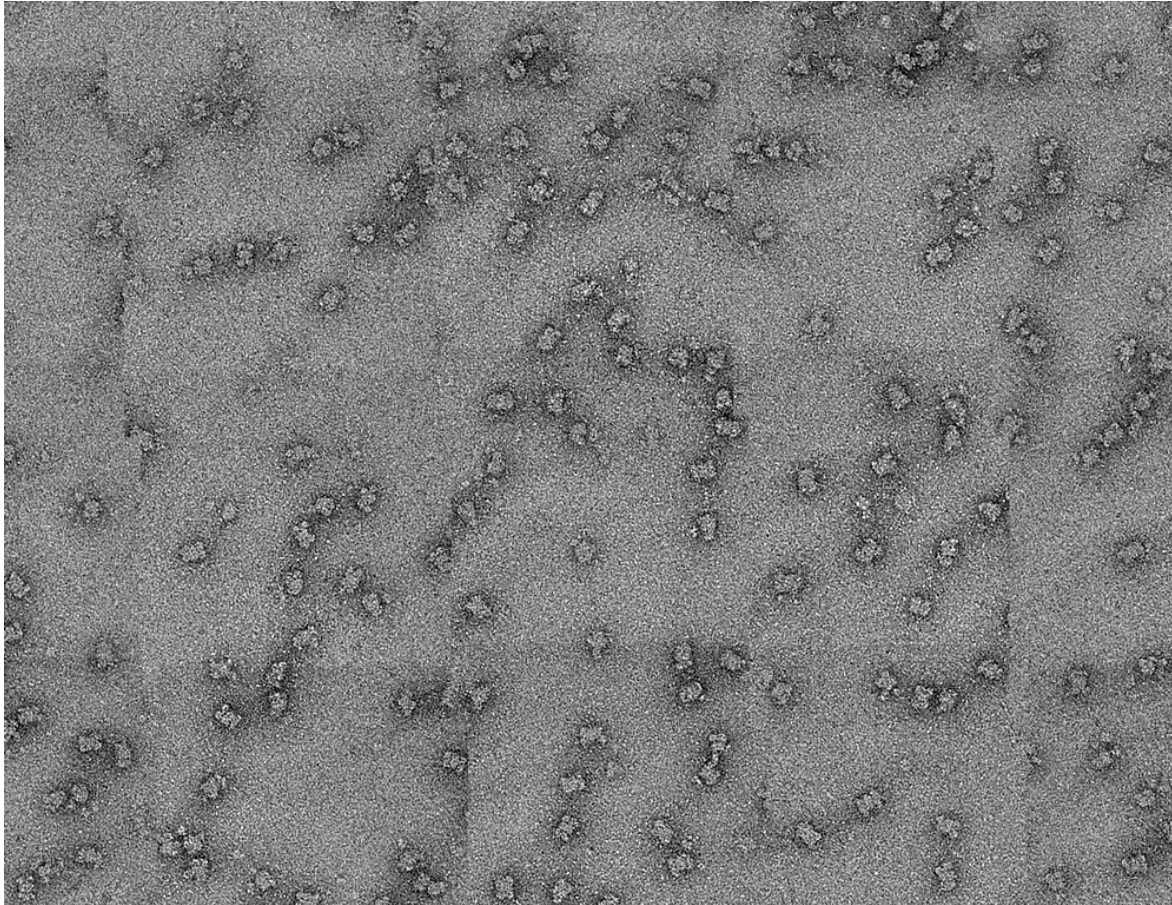


Figure 3-2 Typical Spot Scan of fractions between 45 and 55 ml. On spot scan level a homogeneous protein size seems to be present.

Further analysis of the acquired class averages reveals that (i) the protein of interest is not homogeneous but present in different structural states in the sample already detectable on 2D level and (ii) the particles take up a preferred orientation on the support film. In Figure 3-4 typical class sums are compared and attributed with a scale bar. The particle consist of a central core of $\sim 105 \text{ \AA}$ along the principal axis, to which 0 up to 4 “ear” -subunits are connected. The fraction of particles decorated with all 4 “ears” was found to be very low in the given sample and in the range of 5% compared to particles with less than 4 ears.

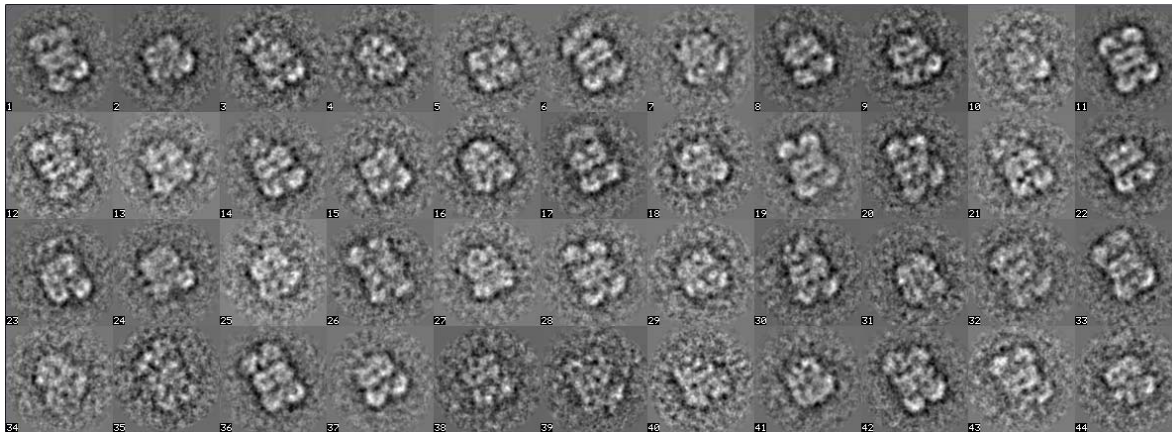


Figure 3-3 Typical 2D MSA based class averages reveal intrinsic heterogeneity.

Further analysis of gel filtration fractions between 55 and 65 ml indicated that it consists of the central core only, without any “ears” (a typical spot-scan of this condition is depicted in Figure 3-5). Since the peak height and the protein concentration of the fraction without “ears” is much higher, it was found likely that the purification protocol used did not reliably preserve the whole particle, at least not in a sufficient ratio for 3D de novo analysis.

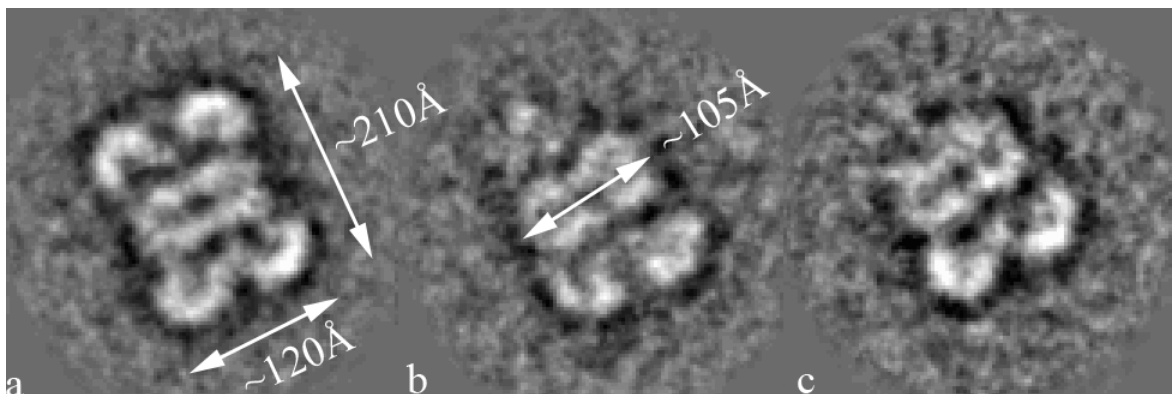


Figure 3-4 Comparison of typical 2D class sums. The particle is present in the sample in different states of integrity. The central core ($\sim 105 \text{ \AA}$) has up to 4 attached “ear”-like subunits. (a) Shows the state with 4 subunits, (b) shows the state with one missing “ear” and (c) depicts the state with 2 missing ears. Further states exist with 0-4 “ears” in all possible permutations.

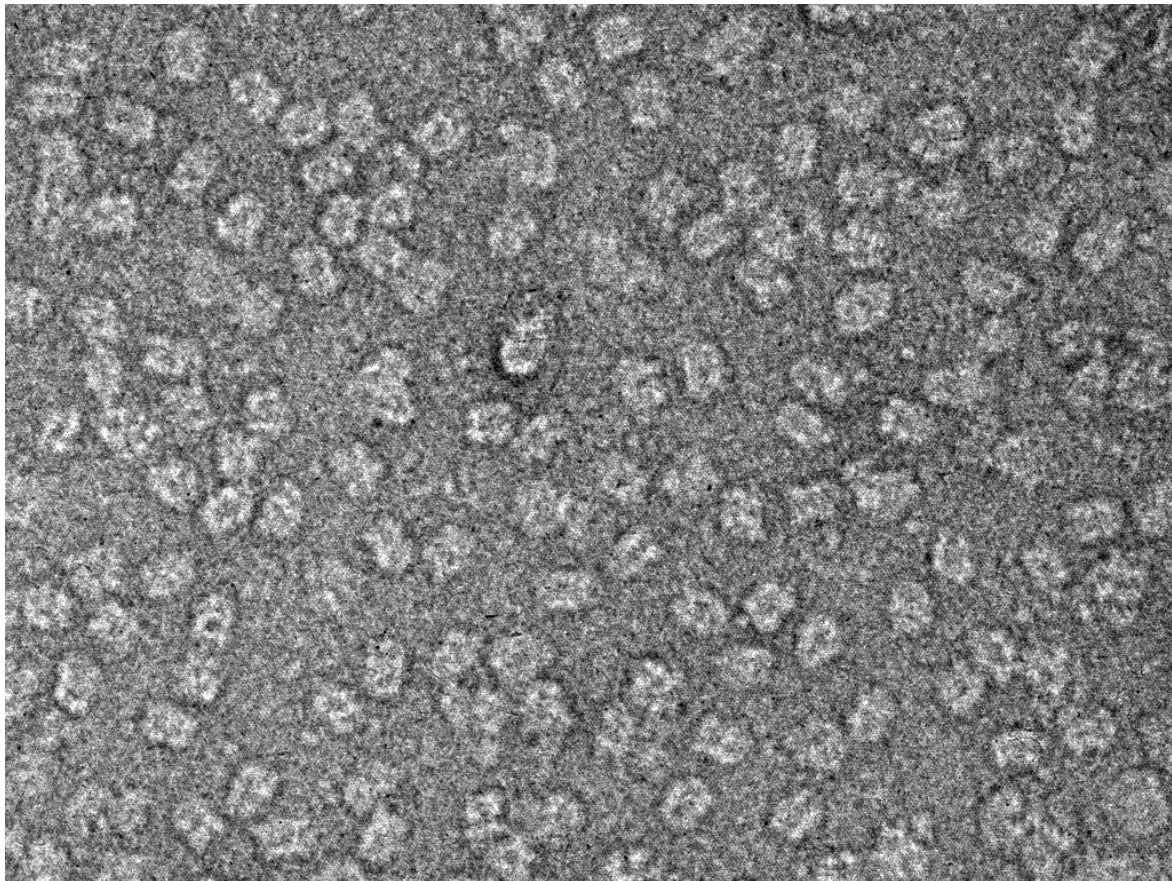


Figure 3-5 Typical spot scan of the highest gel filtration peak (55 – 65 ml). In this fraction the central core only is present, without any connected “ear”-like subunits.

3.1.3 Optimization of purification of AccBC-AccD1 complex from *C. glutamicum* strain Δ pyc paacBC p-H6D1 for EM

All steps of the purification protocol as described above were systematically tested for effects on the integrity of the particle of interest, resulting in a completely new protocol. First of all, the method for lysing bacterial cells by ultrasonification was investigated. Aliquots of raw extract, taken subsequently after each ultrasonic pulse, were purified following the original protocol and analyzed by EM. This analysis revealed already that after the first ultrasonic pulse, intact particles and particles lacking ears could be detected in a very low concentration. The application of further ultrasonic pulses did indeed increase total protein concentration but in parallel the fraction of intact particles was constantly reduced. Therefore, the method for cell lysis was changed from ultrasonification to the liquid nitrogen mortar technique as described by (Umen and Guthrie 1995; Gottschalk, Neubauer et al. 1999). The resuspended bacterial cells adjusted to a glycerol concentration of 5 % were slowly trickled into a ceramic mortar filled with and kept in liquid nitrogen, such forming small frozen beads. These beads were then ground using a ceramic piston and manual force

until a white colored powder was formed out of the originally yellowish resuspended bacterial cells. This powder was now slowly defrosted on blue ice in a 4 °C fridge and then further subjected to the original purification protocol starting with exclusion of cell fragments and intact cells as described above. EM analysis before gel filtration proved a much higher concentration of intact particles but also that a size exclusion step is indispensable for single particle analysis. Therefore the original size exclusion by gel filtration was replaced by first glycerol gradient centrifugation and finally gradient centrifugation in combination with gradient fixation following the “GraFix” protocol from (Kastner, Fischer et al. 2008). Glycerol concentrations of 10-30 % and fixative concentrations of 0.05 – 0.5% were used to form a gradient, followed by centrifugation at 30K rpm for 18h at a temperature of 4° C. Further optimization of the purification protocol finally resulted in the buffer conditions numbered 2 in section 2.2.2. The main changes improving concentration of intact particles were addition of protease inhibitors and EDTA, addition of CoA sodium salt to the buffers, and replacement of imidazole by histidine for elution of 6xHis tagged protein from Ni-NTA columns. With this optimized purification protocol, the concentration of intact particles featuring 4 “ears” could be improved to ~20%. The homogeneity and integrity of this sample - even using the improved purification protocol- was thus not high enough to facilitate 3D-structure determination using classical single particle techniques. Nevertheless, this enzyme was an ideal model for method development aiming at structure determination of highly heterogeneous specimen.

3.1.4 RCT negative stain EM of Acetyl CoA-Carboxylase complex AccBC-AccD1 after optimized purification

Fractions from “GraFix” size exclusion and fixation were prepared for electron microscopy using the negative stain “sandwich” technique as described above and screened for the highest concentration of intact particles by EM visual inspection. Tilted pairs were recorded on CCD camera by the small spot scanning technique (see section 1.4.1) using imaging conditions as described in section 2.3 at specimen holder tilt angles of 0° and 45°. Data sets of 5165-8856 tilted pairs were acquired at an effective magnification of 123200 using imaging conditions described in section 2.3. Selection and extraction of particles was performed pair wise, conserving the relation between untilted and tilted view of the particles using a software developed in the Stark department (see Figure 3-6 (unpublished work)).

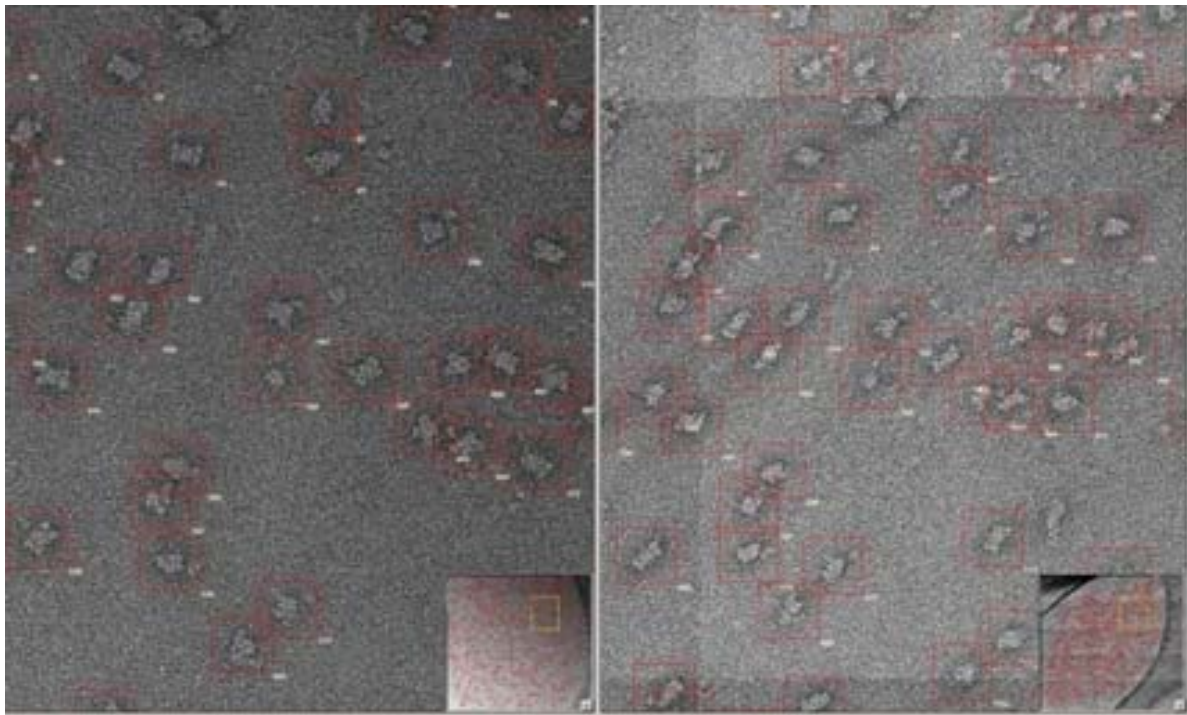


Figure 3-6 Micrographs of the same area of sample recorded with untilted specimen holder (left) and specimen holder tilted by 45° (right). Particle selection and extraction is done pair wise to preserve “tilt-mate” relation between untilted and tilted view.

The untilted data sets were first treated by 4-6 rounds of reference free alignment followed by MSA in combination with exhaustive MRA using a resampling to polar coordinates. Class averages consisting of ~30 class members were computed and subsequently an increasing number was manually selected for further processing and used as references in a new round of exhaustive MRA followed by another round of MSA, finally resulting in 50 class averages, 44 of which are depicted in Figure 3-7. The improved fraction of intact particles is reflected in the class sums.

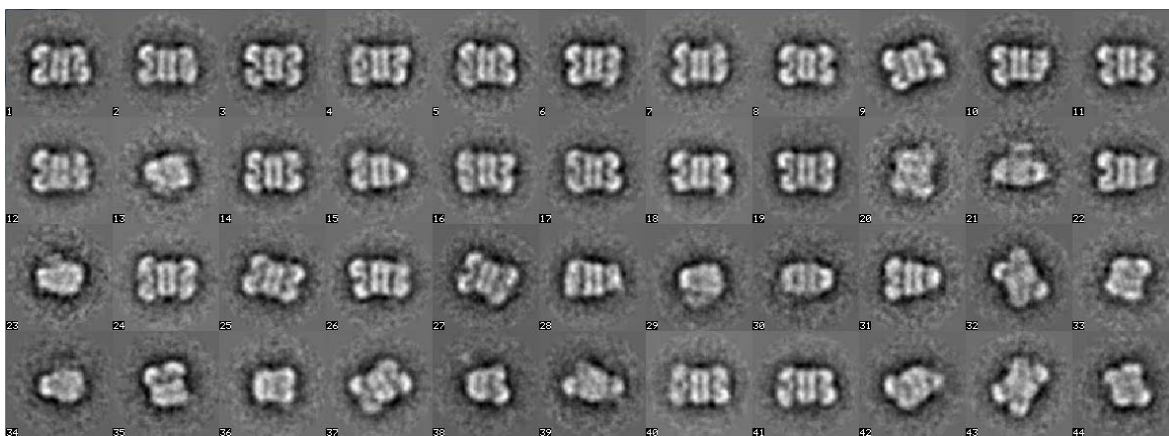


Figure 3-7 Typical class sums obtained after 2D de novo analysis of specimen purified, following the optimized purification protocol including GraFix. The fraction of particles featuring 4 “ear”-like subunits is increased.

From the untilted class sums, the best 30 were selected and 30 3D structures were calculated using the RCT method as described earlier. In Figure 3-8 four 3D structures, calculated from 4 different class sums are shown.

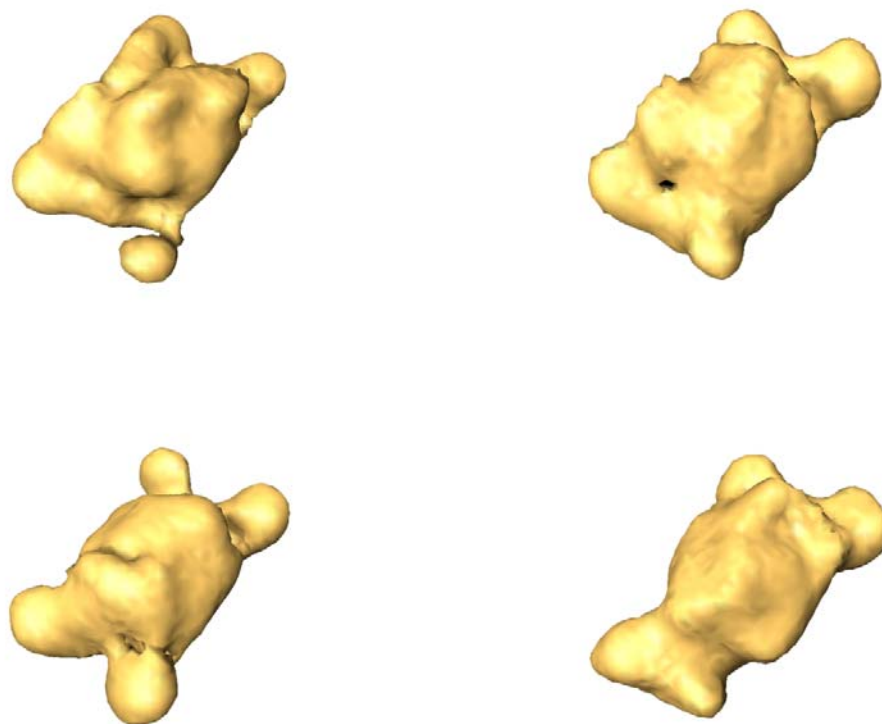


Figure 3-8 From the 30 2D class sums, 30 3D structures (not all shown) were calculated using the RCT method. The 3D structures reflect, what was observable on 2D level. The “ear”-like subunit is not present in all the class members and smeared out due to flexibility.

For generation of a reliable 3D starting structure for resolution refinement and further analysis, the 3D models obtained by RCT were aligned and summed up to form a consensus model of all generated RCT starting structures. Due to the combination of missing cone and preferred orientation in the data sets, the quality and reliability of the consensus model cannot be trusted to be reliable enough to use it as starting model for refinement and separation of conformational states. To get a general idea of the possible shape of AccBC-AccD1 complex, the consensus model was further imposed with two fold symmetry as indicated by 2D analysis. Since three-dimensional symmetry properties cannot be analyzed on a 2D level, a model imposed with C2 symmetry and a model imposed with D2 symmetry (Schoenflies notation) were generated as depicted in Figure 3-9.

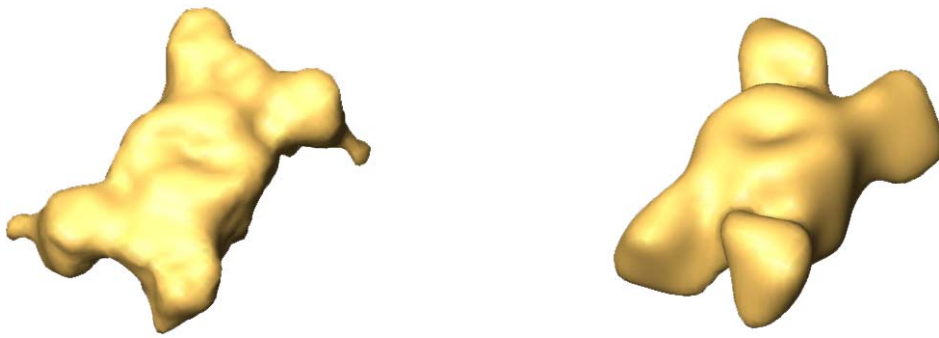


Figure 3-9 Artificial 3D models, generated by imposing C2 symmetry (left) and D2 symmetry (right) on the consensus model generated by averaging of 30 3D structures generated by RCT reconstruction.

To further study the symmetry properties and the overall composition of AccBC-AccD1 complex, 2D references were generated by forward projection of the artificial 3D models. Supervised concurrent alignment (Klaholz, Pape et al. 2003) in combination with supervised classification (Bohm, Frangakis et al. 2000; Valle, Sengupta et al. 2002; Gao, Valle et al. 2004; Heymann, Conway et al. 2004; Gao, Zavialov et al. 2005) of experimentally acquired particle images against two groups of artificial reference images was then performed. In this method, the 2D projections are compared with several reference density maps, and the similarities of the 2D images to these references are measured by their cross-correlation coefficients. The images are then divided into classes according to the references they best resemble. Comparison of correlation coefficients showed that for a fraction > 90% of the raw data, correlation with artificial references generated from the artificial model with imposed D2 symmetry was higher than for the ones generated from the model with C2 symmetry imposed. The D2 model was then further used to generate 6 artificial models with all possible numbers and permutations of attached “ears” to the core, as depicted in Figure 3-10. These are not well defined 3D structures but likely models representing the overall organization of AccBC-AccD1 complex from *C. glutamicum* after purification.

Projections generated from these 6 3D models reflect 2D class sums very well. Due to the loss of subunits during purification and sample preparation, leading to 6 different states in which the “ear”-like subunit appears to be additionally flexible in combination with the preferred orientation of the particles on the carbon support film, determination of a reliable 3D structure is not possible using RCT on negatively stained samples.

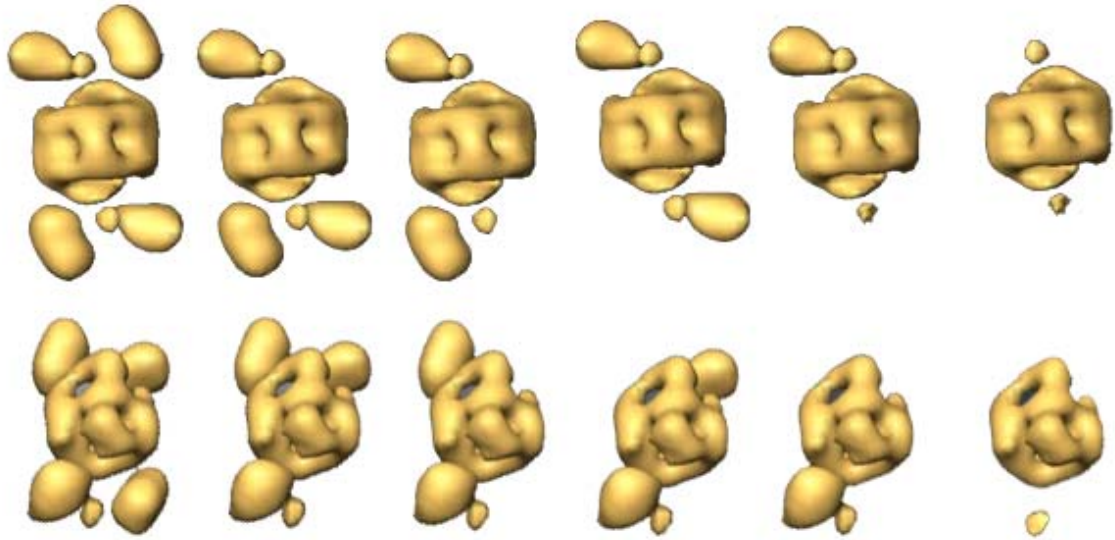


Figure 3-10 Artificial models of the likely overall organization of AccBC-AccD1 complex and the different states of integrity well matched to 2D projections found in the raw data.

To correct for the preferred orientation on the support film, the samples were prepared following the “cryo in holes” technique (Adrian, ten Heggeler-Bordier et al. 1990) where the particles are embedded in vitrified ice without supporting carbon film. Attempts to prepare the samples under cryo-conditions resulted in a complete loss of all “ear”-like subunits during the final buffer exchange step that is necessary to remove the glycerol after gradient centrifugation. Buffer containing glycerol after GraFix was exchanged against ACo Cryo Buffer using Pierce centrifuge columns. The results of the 2D analysis of the resulting samples are depicted in Figure 3-11 (gray values flipped). The measured size of the class sums (not all shown) obtained from 15900 extracted raw images is in good agreement to the size measured for the central core during negative stain analysis of the particles featuring the “ear”-like subunit.

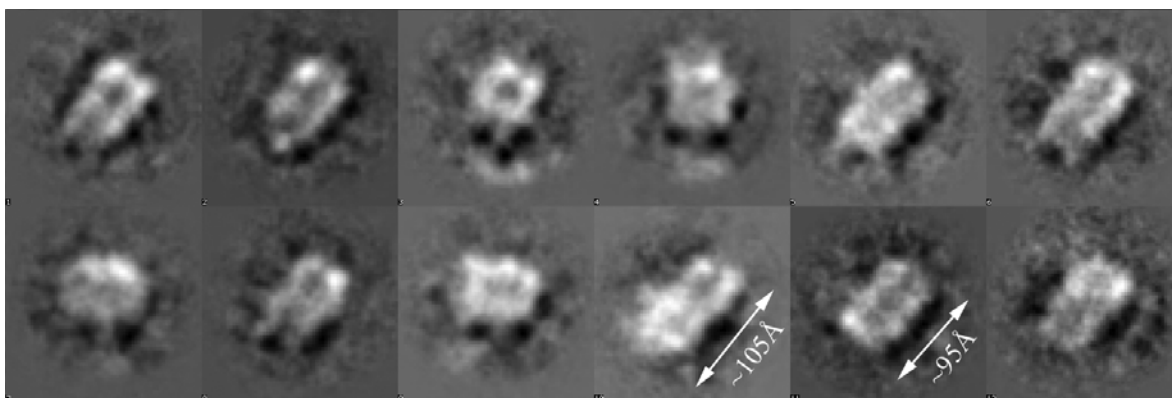


Figure 3-11 Class sums generated from 15900 raw images, prepared using the “cryo in holes” method and therefore treated by buffer exchange using desalting spin columns. The result is the naked central core, observed using negative stain preparation.

Observations regarding low initial fraction of intact particles and instability leading to sensitivity to mechanical stress during purification were communicated to the collaboration partner providing the sample. The findings from the EM studies were also discussed that fractions from the gel filtration, which had tested positively for enzymatic activity actually did not contain mostly intact particles. These findings led to further biochemical studies. These studies recently revealed that the Acetyl CoA Carboxylase of *C. glutamicum* does not consist of only two but of at least three subunits (Gande, Dover et al. 2007). The third ϵ -subunit AccE, that was never co-over-expressed in the samples studied, was reported to have a size of ~ 9 kD, while the molecular weight of the Acetyl CoA Carboxylase Complex was now reported to be 812 ± 35 kDa. Enzymatic tests, combined with the results of EM analysis indicate that the central core with a longest principal axis length of ~ 105 Å is performing the actual carboxylation and thus likely contains copies of the α subunit. The recently isolated ϵ subunit seems to play a role in linking the “ear” subunit (which is likely to be functional essential for substrate specificity and thus likely to contain copies of the β subunit), to the central core complex. Over expression of all three subunits is thus important for formation of particles decorated with all 4 “ear” subunits.

3.2 Getting ready for the next hardware generation

To study heterogeneous specimen like the Acetyl CoA Carboxylase Complex from *C. glutamicum*, the data set has to be split up into subsets representing different conformational states. This approach implies that the number of raw image data is increased and further processing has to take into account a plurality of 3D models. To prepare for the computational demands resulting from this new strategy, hardware and software technologies capable of speeding up algorithms were analyzed and applied to e.g. alignment and 3D reconstruction methods used in cryo EM.

3.2.1 The SmartTray

Standard EM software e.g. (Frank, Radermacher et al. 1996; van Heel, Harauz et al. 1996; Ludtke, Baldwin et al. 1999) traditionally consists of a set of applications, usually written in the FORTRAN programming language. The design and architecture of this software is not targeted at parallel processing at all. Despite of this intrinsic limitation, extensions and solutions exist that parallelize these applications for multicore processing by starting one instance per computational core available or by using MPI to do the same across multiple computers. The scheduling setup of the MPI approach via a "machines file" where all the nodes included in the calculations need to be listed severely limit the usability, especially for

a working group. Another of the MPI drawbacks is the insufficient failover model, which is a basic requirement when several people share the same computing resources with very long running calculations that should not stop in the case of a single node's failure. Thus there was a need for more dynamic resource allocation than the one provided by MPI. Some of the most wanted features were (i) the possibility to pause a long running job for the benefit of a smaller but highly urgent job, (ii) a mechanism for dynamic resource allocation, namely reassigning nodes to already running jobs, (iii) adding nodes to a running calculation and (iv) a failover mechanism that enables a node to automatically rejoin calculations after solving/encountering a hardware problem. Research on middleware implementing these exact features as an industry standard is currently ongoing (Wang, Mueller et al. 2008) but not available. Another highly desired feature was to include the increasing computational power of standard workstations available locally in calculations. For example, a secretary's workstation that was usually utilized only during daytime hours had more computational power than some dedicated cluster nodes. To implement the above-mentioned features and to also make use of the non-dedicated computational resources, a new framework, called "SmartTray", was implemented. The SmartTray mainly consists of a self-updating Smart-Client, running in the system tray of the Windows operating system. The SmartTray Framework is based on the master worker approach in combination with transactional memory. Computations are treated as jobs. A job consists of work packs, which are administered by a master server.

Since this master server was implemented as a Web service using Microsoft SQL Server 2005, which is a transactional database for storage, the transactional capabilities of the database were used to emulate transactional memory by means of high performance database mechanisms. In contrast to the standard approach, where the master server initiates communication to the computational nodes, due to inversion of control from master to node, the whole system is kept as dynamic as possible. Initiating the communication on the node rather than on the master server is thus the key issue for inverting the control. A list of nodes running the Smart Tray is kept on the master server. This list includes the information if the respective node is currently utilized by a user or not. Additionally, the nodes hardware features are listed (see Figure 3-13).

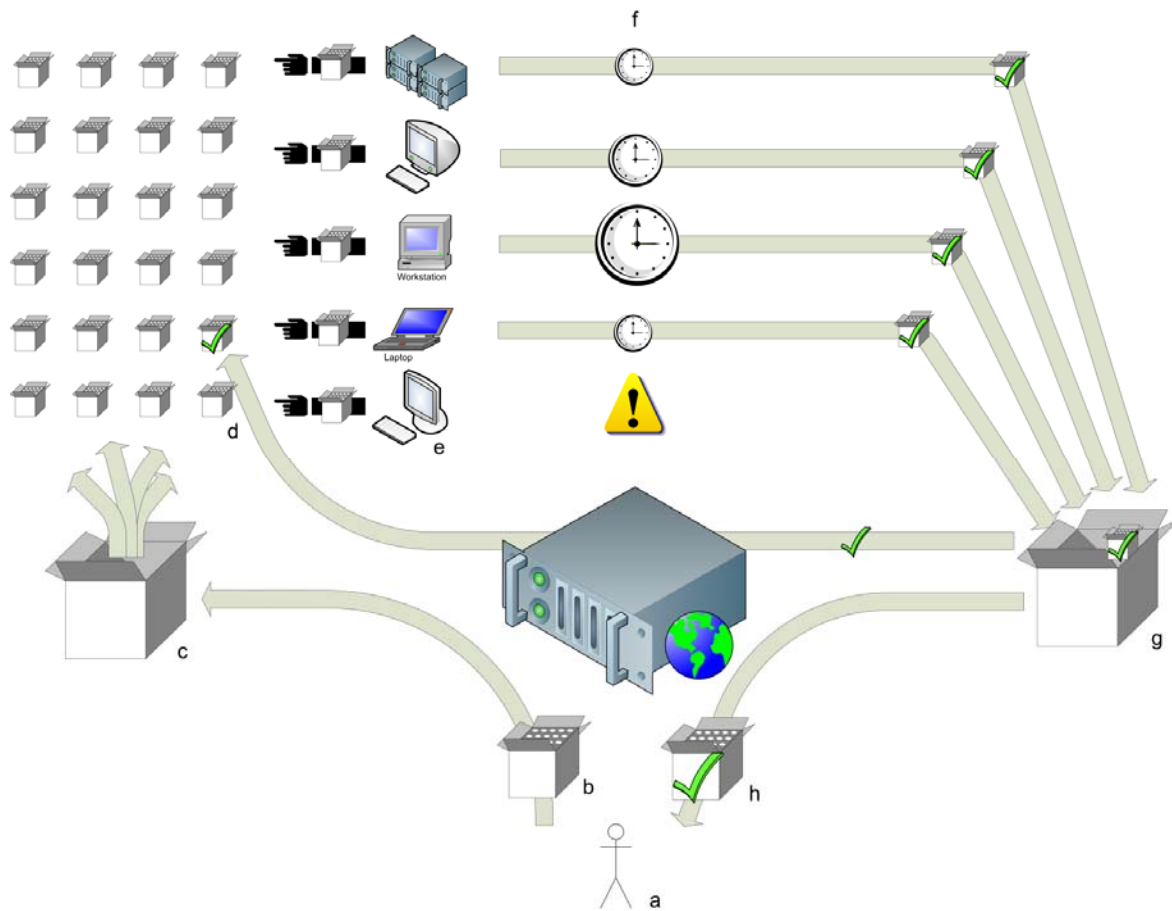


Figure 3-12 The Workflow of the “SmartTray” Framework. A computation is a job (b) that consists of multiple work packs (d) that can be independently processed in parallel. A work pack contains both the data to process and the computation instructions. The job is created by the user (a) and hosted by a master server (represented logical by c and g). All computational nodes, dedicated cluster nodes or volunteer computers (e), poll work packs (d) from the master server (c), execute the calculation (f), and send the result to the master server (g). When a work packs result is not returned within a given time out period (or nodes are idle otherwise), the work pack will be re-dispensed as a failover measure. As a side effect, the master server holds a constantly updated list of nodes that are willing to participate in calculations including their hardware features.

Depending on the hardware configuration regarding number of CPU’s and GPU’s, the corresponding software version is executed, making use of these features. Additionally, individual compute jobs can be paused, resumed and varied in their priority. Nodes can also be assigned to jobs individually. Each single node polls work packs from the master server, executes them and returns the results to the master server. In case of node failure a work pack will not be completely finished in time. The same work pack will then simply be executed again by another node. A recovered node can also restart; contributing to the overall calculations simply by polling a new work pack. A major advantage of the SmartTray approach is that it is programmed to run hardware detection on each node before entering computations. Based on the hardware, the software version of the main logic will then

choose the correct mode of execution. In case of a multicore or a multi CPU node, the OpenMP version will be executed.

Figure 3-13 A list of Nodes running the Smart Tray is kept on the Master server. This list includes the information if the respective node is currently utilized by a user or not and the nodes hardware features. Depending on the hardware configuration regarding number of CPU's and GPU's, the corresponding software version is executed, making use of these features. Additionally, individual compute jobs can be paused, resumed and varied in their priority. Nodes can also be assigned to jobs individually.

3.2.2 Foundations for GPU computing

Several test of usability of parallel hardware were conducted, namely using the Cell BE Processor (Kahle and IBM 2005; MERCURY 2006) and different graphics boards.

The application or algorithm tested was the FFT since it is essential for most computational-intensive problems in EM image processing. First results showed that an actual speed up could only be achieved for image data with a pixel size of > 256 x 256 pixels. This limitation was originated in the limited bus speed, causing the transfer time of data from the CPU to the parallel processing board to extinguish the processing speed improvement for small images but was still very promising especially because even bigger pixel frames are used in refinement to obtain high resolution structures. Best experiences regarding usability and obtained speed up over cost was obtained using NVIDIA GPUs. First experiences with GPU

programming was performed by “abusing” the GPU graphics primitives for general-purpose computations, starting with OpenGL Shading Language (GLSL), followed by NVIDIA shader language, NVIDIA Cg (Mark, Glanville et al. 2003), a C extension originally designed for programming visual effects. NVIDIA Cg and Brook (Buck, Foley et al. 2004) were the first languages for general purpose computations on graphics cards. The first applications ported were FFT calculations and three-dimensional reconstruction techniques such as SIRT and ART. A speedup factor of 30 in 3D reconstruction algorithms on the graphics card lead to incorporation of the GPU version into the SmartTray framework (see Figure 3-13). SmartTray is able to detect the graphics card and can then automatically make use of the faster GPU software

3.3 Getting ready for the next generation of instrumentation

The properties of particles Acetyl-CoA Carboxylase studied under EM conditions combine several features that hinder computation of a reliable starting structure. Heterogeneity and instability, aggravating cryo preparation, in combination with the tendency to bind to the carbon support film in a preferred way render standard RCT methods nearly viewless. The latest generation of cryo electron microscopes like the “FEI Titan Cryos”, whose setup is nearly complete in the Stark lab (see Figure 3-14) improves image acquisition, especially of tilted pairs under cryo conditions in several ways.

The specimen holder’s position can be switched between tilt states in the magnitude of seconds with no adjacent drift. Thermal drift is also virtually eliminated by advanced engineering. The stability of the specimen holder in combination with a dynamic focusing based on the position of the specimen holder not only unburdens the operator from the task of checking for eucentric height and defocus settings but also drastically increases the number of obtainable tilted pairs at a quality level compared to that of untilted images. The images recorded with the specimen holder in a tilted position are not subjected to a systematic defocus gradient and the influence of drifting does not systematically alter their properties. At this quality level, the OTR method (Leschziner and Nogales 2006) (compare section 1.5.6) yet only described theoretically can be established in practice since classification of images, recorded with a tilted sample stage, becomes feasible. This only holds true for images acquired under cryo conditions, because classification of tilted images recorded under negative stain conditions will still be hindered by specimen flattening, regardless of the microscope used. Particles that are sensitive to procedures required for cryo

preparation may also be analyzed with this type of microscope since the number of intact images acquired in a reasonable time allows for much better statistics.

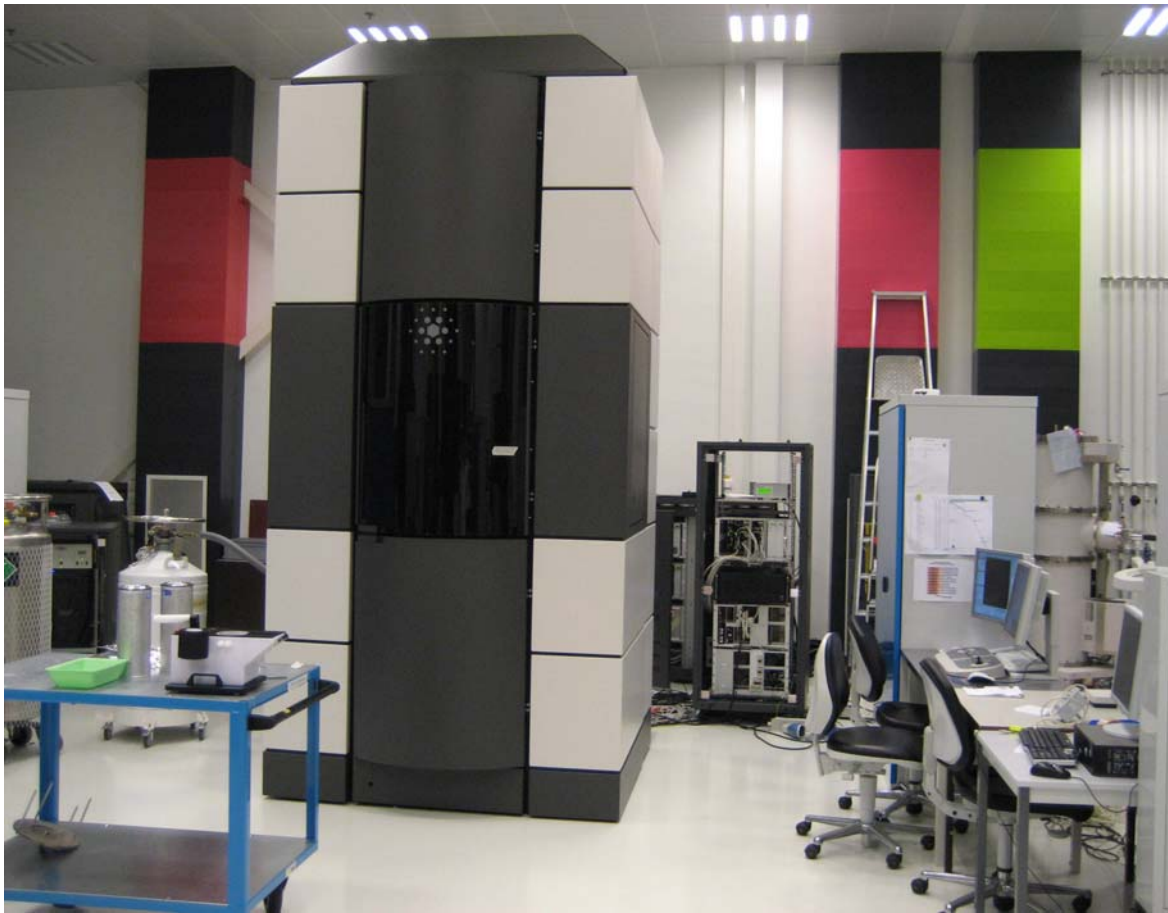


Figure 3-14 The latest generation of cryo electron microscopes like the FEI “Titan Cryos”, whose setup is nearly complete in the Stark department dramatically enhances the process of especially the collection of tilted pairs under cryo conditions dramatically. The specimen holder’s position can be switched between tilt states in the magnitude of seconds with no adjacent drift. Thermal drift is also virtually eliminated by advanced engineering. The stability of the specimen holder in combination with a dynamic defocusing based on the position of the specimen holder not only unburdens the operator from the task of checking for eucentric height and defocus settings but also drastically increases the number of obtainable tilted pairs at a quality level compared to untilted images.

3.3.1 New methods for computation of missing cone free starting models

Based on the experiences while studying Acetyl-CoA Carboxylase, new algorithms were developed, targeting at the features of the next generation not only of computer hardware but also instrumentation. With the prerequisites fulfilled to classify not only untilted but also tilted views reliably, completely new options are made accessible.

3.3.2 Connectivity graph

Between “tilt mates”, the experimental tilt-angle relationship is known. Within classes obtained by e.g. MRA and MSA of the untilted and tilted views separately, a classification and alignment relationship exists as illustrated in Figure 3-15.

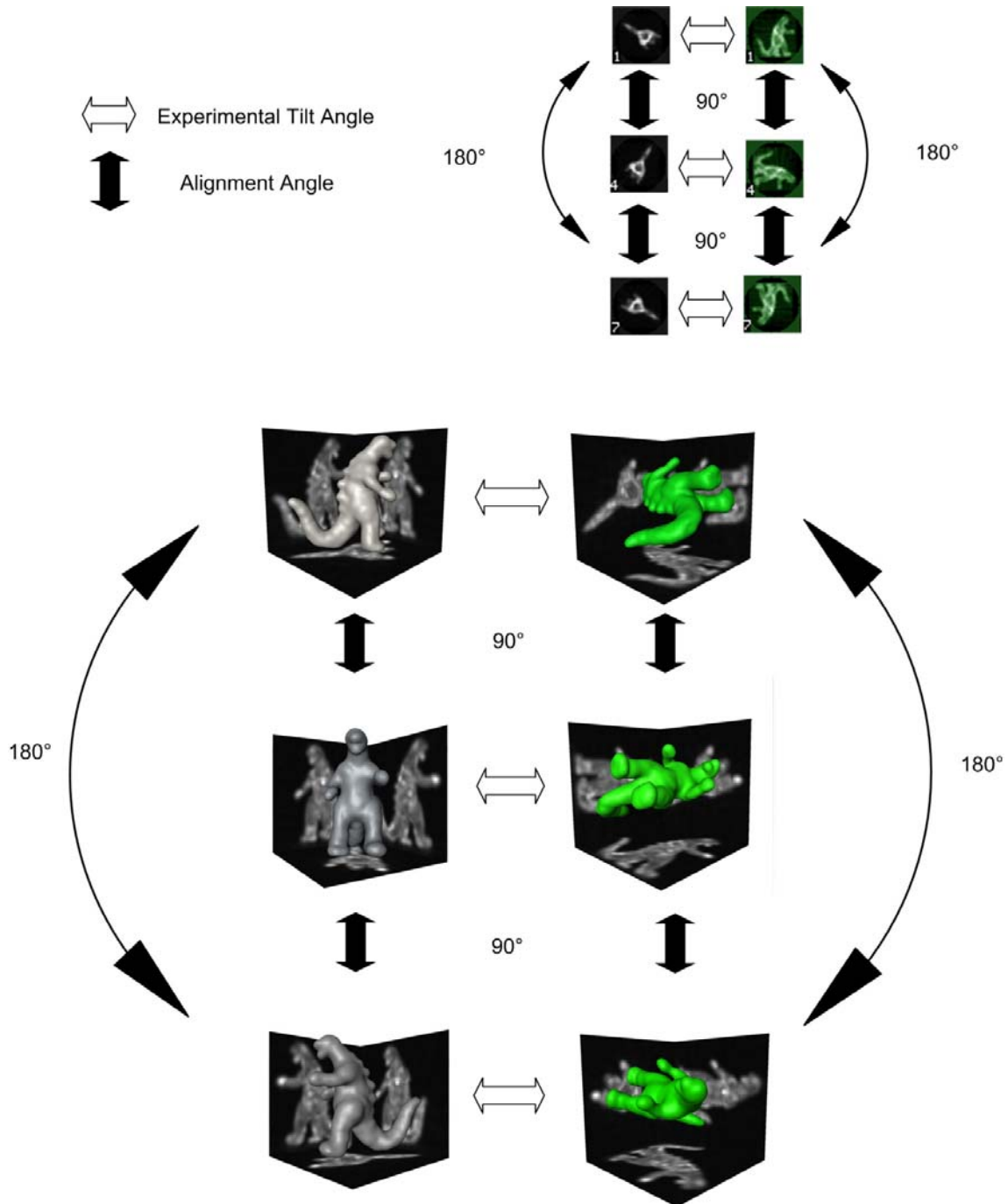


Figure 3-15 A schematic illustration of tilt and class sum relations of projection images. (Here depicted for the OTR approach and therefore a total tilt angle of 90°.)

This information can now be combined (see Figure 3-25). Since the experimental tilt angle relationship is known and the alignment angle of a class sum relative to its class members

can also easily be obtained, projection direction, e.g. Euler angles can be assigned to every projection image based on the angular relationships of classification and tilt. In the following algorithm description, the term “untilted” is not restricted to images recorded with an untilted specimen holder. In case of image acquisition under OTR conditions, untilted would e.g. mean the -45° tilt angle settings and tilted the $+45^\circ$ tilt setting of the sample stage.

The algorithm internally uses spherical polar coordinates, not Euler angles because in addition to the projection directions it needs to access the relative orientation of reference frames in addition to the orientations of three-dimensional objects within different reference frames which cannot be described unambiguously using Euler Angles. The spherical polar coordinates used within the algorithm are depicted in Figure 3-16.

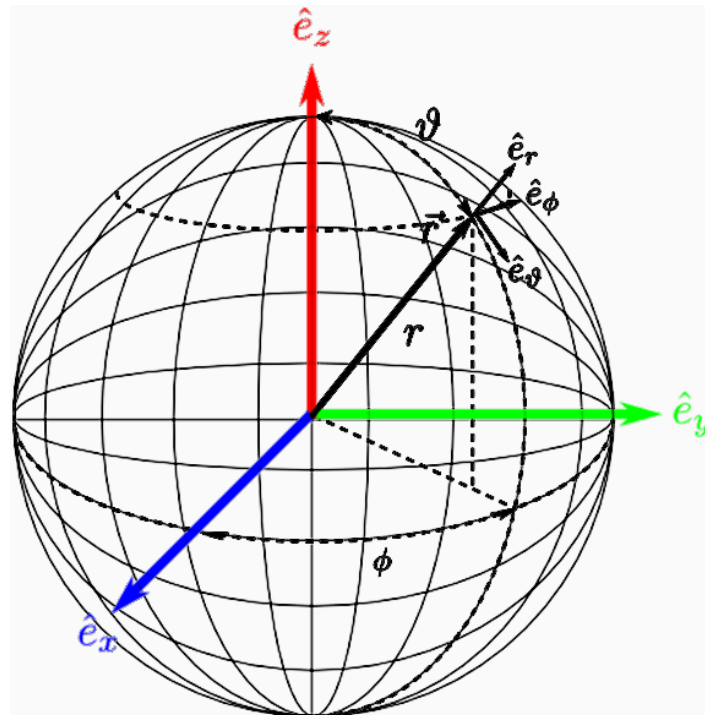


Figure 3-16 Definition of the spherical polar coordinates used. In the following figures these coordinates are depicted rotated by 90° around e_z .

The algorithm for building the connectivity graph and assigning projection directions works as follows: the procedure starts with an untilted single view (starting single view, UT1, depicted in Figure 3-17) belonging to a starting untilted class sum (CS_UT_1).

The first untilted single view (UT1) defines the reference frame for projection direction assignment. Its Euler angles are set to $\text{Euler}(\alpha,\beta,\gamma)=(0,0,0)$ by definition.

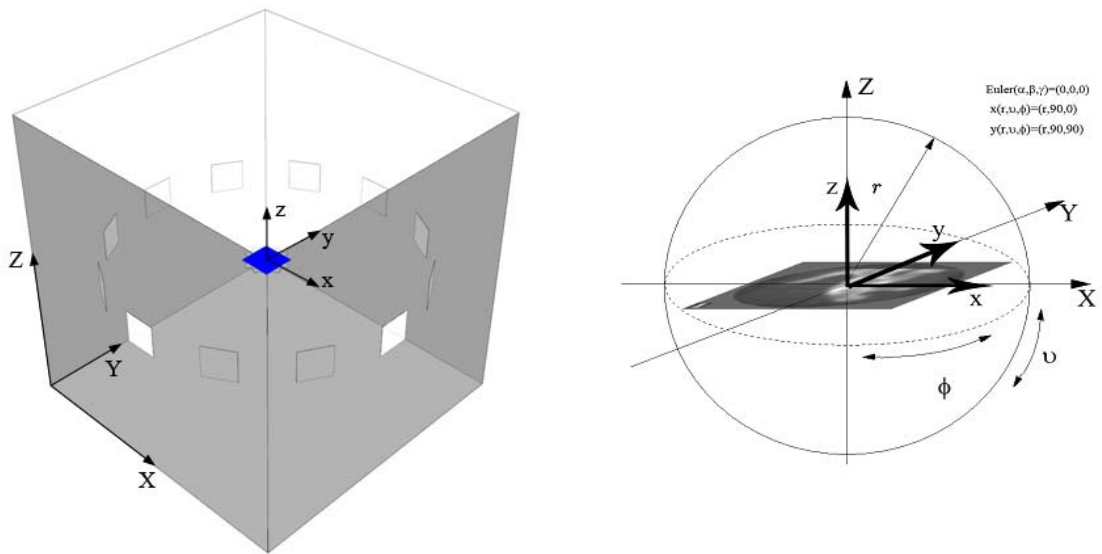


Figure 3-17 The first untilted image (UT1) used as the starting point for the algorithm. The image's reference frame (X,Y,Z) defines the global reference frame (x,y,z) , in which projection directions are expressed for all other images. (X,Y,Z) for the very first image equals (x,y,z) by definition.

Now the class members of the starting untilted class sum (CS_UT_1) can be attributed with Euler angles based on their alignment angles as depicted in Figure 3-18.

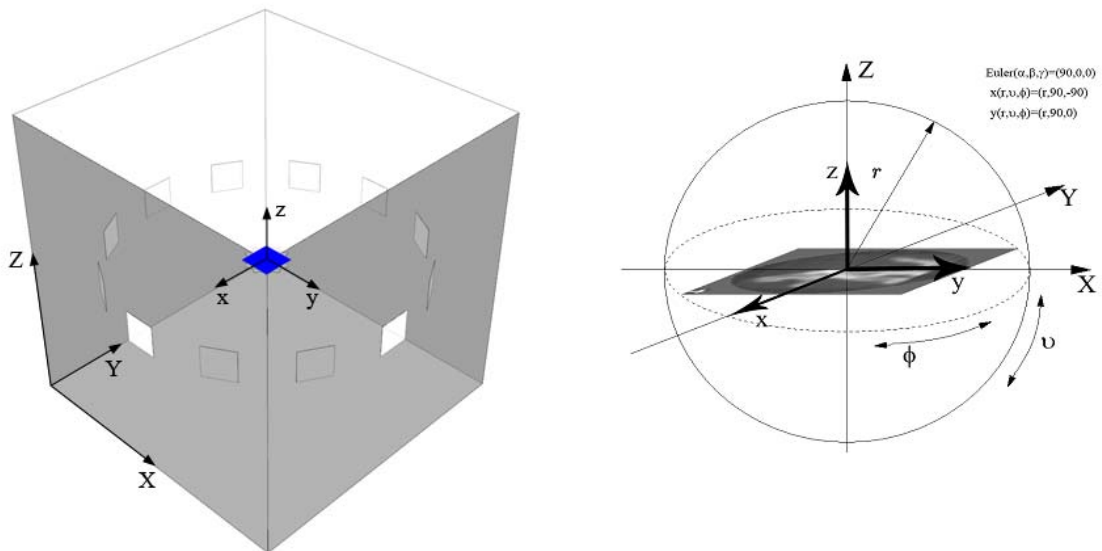


Figure 3-18 The untilted single view (UT2). Its reference frame (X,Y,Z) is rotated in-plane only, relative to the global reference frame by the Euler angle α around the z axis. UT2 is a class member of the same class as the very first starting image (UT1). (Operations performed starting from (UT1): alignment untilted side)

Then for every class member of (CS_UT_1), tilted single views can be identified, having a tilt-mate relation to the class members of (CS_UT_1).

Assignment of projection directions can now be performed for all tilt-mates. For the starting single view (UT1), this can easily be done as depicted in Figure 3-19.

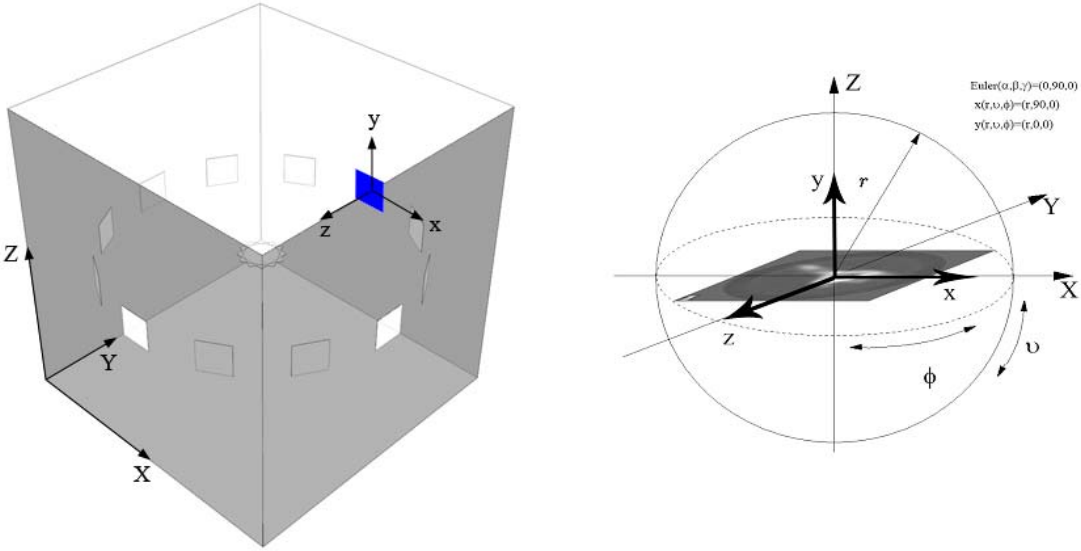


Figure 3-19 The image (T1) is the "tilt-mate" to the very first starting image for the algorithm (UT1). The reference frame (X,Y,Z) of (T1) is tilted by the experimental tilt angle β (here 90°) around the X axis. (Operations performed starting from (UT1): tilt from untilted to tilted side)

Due to the tilt angle relationship, a conical geometry is defined, as in the RCT method (compare section 1.5.5). The origin of the azimuthal angle (Φ in the spherical polar coordinates) is now defined by the position of the tilt mate to the starting single view (UT1). This relation now defines the virtual tilt-axis for all following projection direction assignments.

For the tilt-mates of the other members of CS_UT_1, starting with the tilted single view T2 which is the tilt-mate to UT2, the alignment angles, the in plane rotations of the untilted single views relative to their class member UT1, can now be translated to azimuthal rotations of the tilted single views, exploiting the alignment angles of the untilted single views and the tilt relationship as depicted in Figure 3-20.

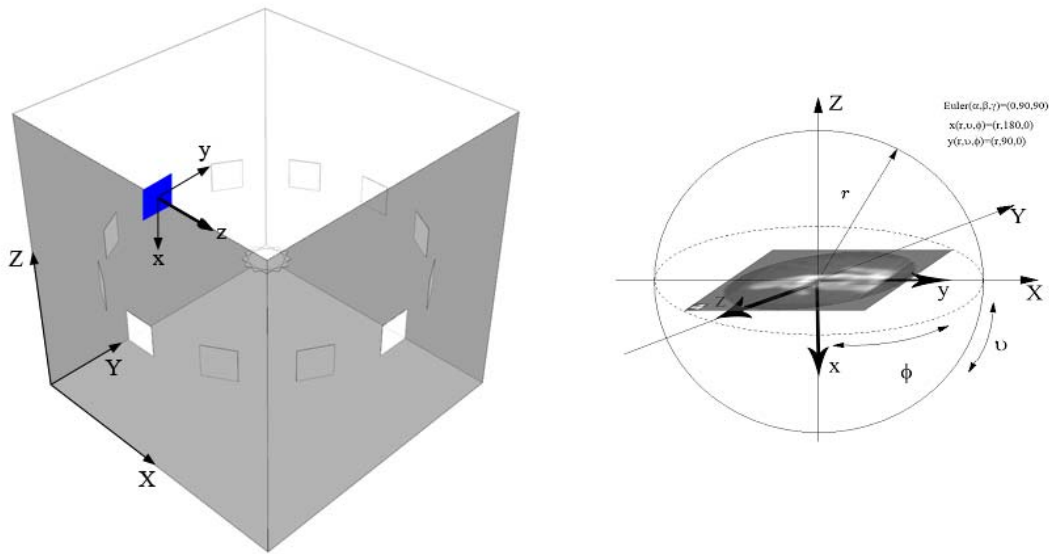


Figure 3-20 The tilted image (T2) is the "tilt-mate" to the untilted, but aligned image (UT2). The image's reference frame (X,Y,Z) is first rotated by the alignment angle α (here 90°) around the z axis and then tilted by the experimental tilt-angle β (here also 90°) around the X axis. (Operations performed starting from (UT1): alignment on untilted side, tilt from untilted to tilted side)

Each tilted single view T_n will now again be member of a tilted class sum CS_T_N . The alignment angles of the tilted single views T_n relative to their class sum CS_T_n can now be exploited to assign projection directions to all other class members of the respective tilted class sum. Here again a case differentiation has to be considered since all projection direction assignments occur in the reference frame of the starting single view. For the class members of CS_T_1 , (the class that the tilt-mate of the starting single view is a member of), no alignment was performed on the untilted side. The assignment of projection directions occurs as depicted in Figure 3-21.

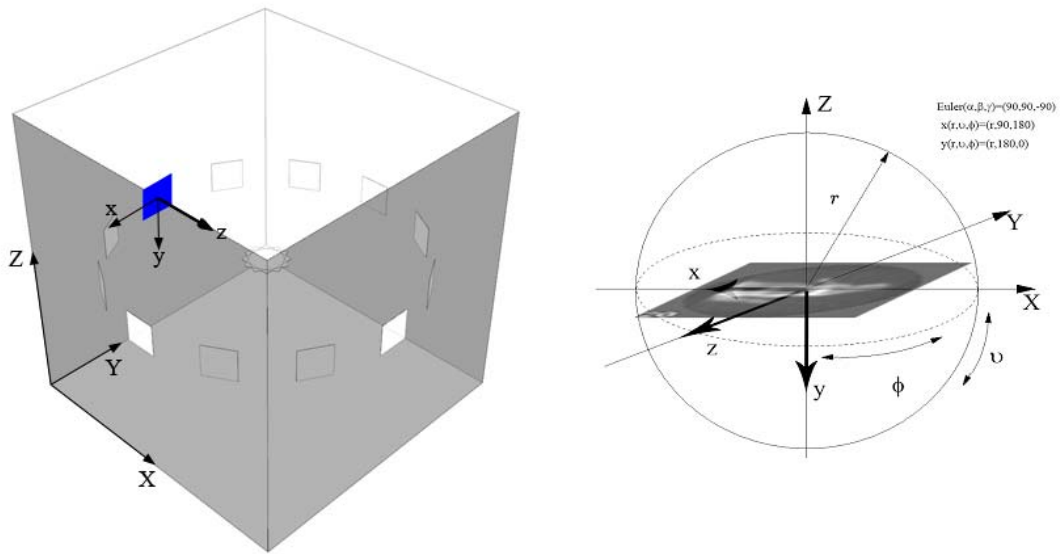


Figure 3-21 The tilted image (T4) is class member of the same tilted class sum as (T2). The image's reference frame (X,Y,Z) is first rotated by the alignment angle α (here 90°) around z, then rotated by the experimental tilt angle β (here also 90°) around X and then again rotated by the alignment angle α (here 180°) around z. (Operations performed starting from (UT1): alignment untilted side, tilt from untilted to tilted side, alignment tilted side).

For tilt-mates of single views that were aligned on the untilted side first, the assignment of projection directions occurs as depicted in Figure 3-22.

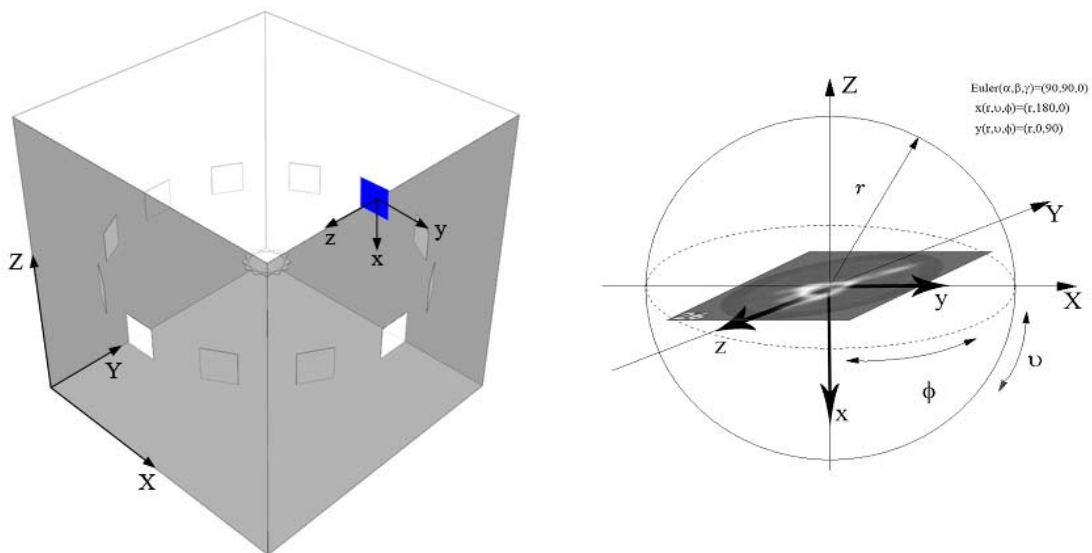


Figure 3-22 The tilted image (T3) is a class member of the same tilted class sum as (T1). The image's reference frame (X,Y,Z) is tilted by the experimental tilt angle β (here 90°) around X and then rotated by the alignment angle α (here also 90°) around z. (Operations performed, starting from (UT1): tilt from untilted to tilted side, alignment on tilted side)

At this stage already, projection directions were assigned to one untilted class sum and all its members and additionally, multiple (depending on the number of class members of the initial untilted class sum) tilted class sums and all their members. This information can already be utilized to reconstruct a three-dimensional model comparable to the RCT approach. But in contrast to RCT now a multi class sum model can be obtained, just by exploiting the information obtained by classification of untilted and tilted projection views independently. Depending on the tilt-angle used, this model is still flawed by a systematic missing cone.

The missing cone can now be eliminated by continuing the algorithm by tracking further alignment, classification, and tilt relations from the tilted back to the untilted side. As depicted in (Figure 3-23 and Figure 3-24) again a distinction of cases has to be taken into account whether an alignment was performed on the untilted side (Figure 3-23) or not (Figure 3-24).

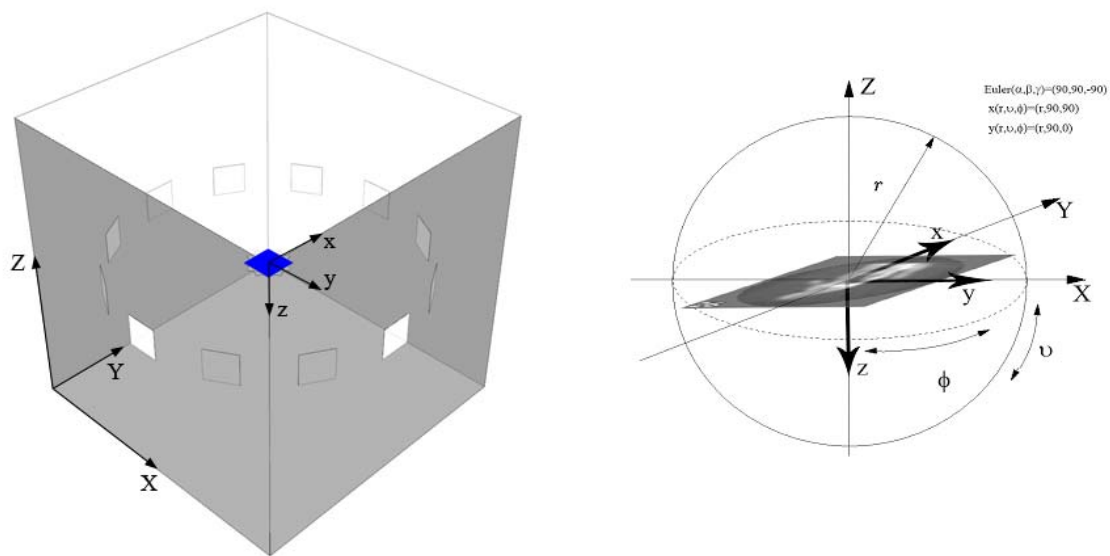


Figure 3-23 The image (UT 3) is the "tilt-mate" to the image (T3). The image's reference frame (X,Y,Z) is first rotated by the experimental tilt angle β (here 90°) around X, then rotated by the alignment angle α (here also 90°) around z and then rotated by the experimental tilt angle β (here now -90° because it is a tilt from the tilted to the untilted side) again around X. (Operations performed starting from (UT1): tilt from untilted to tilted side, alignment tilted side, tilt from tilted to untilted side.

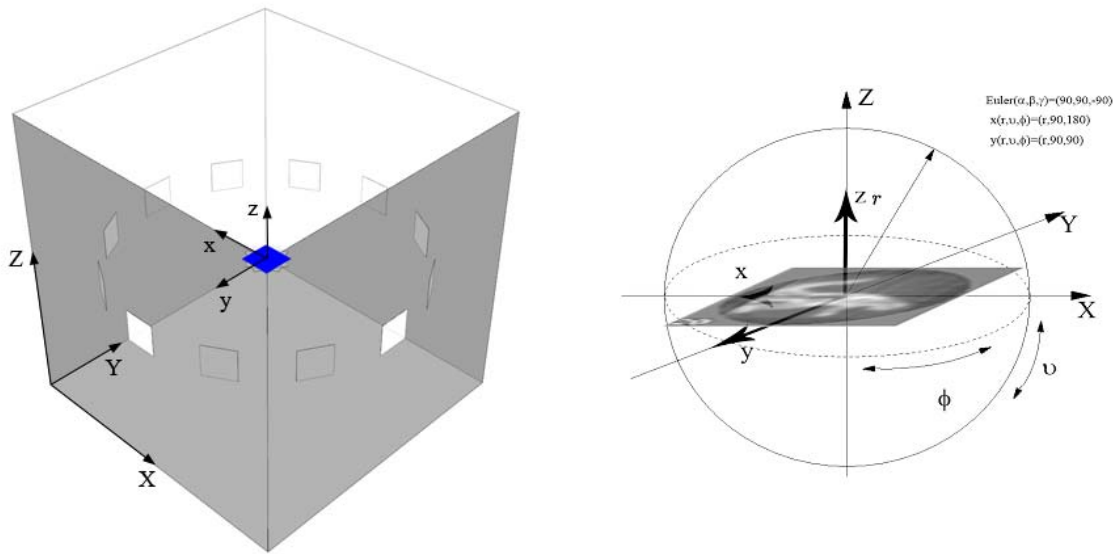


Figure 3-24 The image (UT4) is the "tilt-mate" to (T4). The image's reference frame (X,Y,Z) is first rotated by the alignment angle α (here 90°) around z, then rotated by the experimental tilt-angle β (here also 90°) around X, then rotated by the alignment angle α (here 180°) around z and then rotated by the experimental tilt angle β , (here -90° because the tilt is from the tilted to the untilted side) around X. (Operations performed starting from (UT1): alignment untilted side, tilt from untilted to tilted side, alignment tilted side, tilt from tilted to untilted side.

With the first step performed back from the tilted to the untilted side, projection directions will now cover the Euler unit-sphere without a systematic missing cone but with a random spacing of angular coverage originated in the random alignment angles of the tilted and untilted single views within their respective class sums. In Figure 3-25 the coverage of the Euler sphere is illustrated. The steps illustrated in Figure 3-17 - Figure 3-24 are sufficient to treat all possible alignment and tilt relationships. It is very important to care for the order of operations since the different rotations of reference frames do not commute. In addition to the Euler angles for every projection view, the relative orientations of reference frames has to be stored and taken into account during application of the algorithm. In practice this is realized by storing the orientations of X,Y and Z axes expressed in spherical coordinates of the global (x,y,z) coordinate system. Euler angles can then be obtained by combining coordinate transformation from spherical coordinates to Cartesian coordinates defined by Jacobi-Matrix:

$$J = \frac{\partial(x, y, z)}{\partial(r, \theta, \varphi)} = \begin{pmatrix} \sin\theta \cos\varphi & r \cos\theta \cos\varphi & -r \sin\theta \sin\varphi \\ \sin\theta \sin\varphi & r \cos\theta \sin\varphi & r \sin\theta \cos\varphi \\ \cos\theta & -r \sin\theta & 0 \end{pmatrix}$$

Equation 3-1

with a coordinate transformation from the reference frame (X,Y,Z) to the reference frame (x,y,z). Given a frame (X, Y, Z) expressed in coordinates of the reference frame (x, y, z), its Euler Angles can be calculated searching for the angles that rotate the unit vectors $(\vec{x}, \vec{y}, \vec{z})$ to the unit vectors $(\vec{X}, \vec{Y}, \vec{Z})$ using the following relations:

$$\vec{z} \cdot \vec{Z} = \cos\beta$$

$$\vec{N} = \vec{z} \times \vec{Z}$$

$$|\vec{N}| = \sin\beta$$

Equation 3-2

Therefore:

$$\beta = \arg(\vec{z} \cdot \vec{Z}, |\vec{N}|)$$

$$\alpha = \arg(\vec{N} \cdot \vec{x}, \vec{N} \cdot \vec{y})$$

$$\gamma = -\arg(\vec{N} \cdot \vec{X}, \vec{N} \cdot \vec{Y})$$

Equation 3-3

where $\arg(u,v)$ is the polar argument of the vector $\begin{pmatrix} u \\ v \end{pmatrix}$, taking values in the range $[-\pi < \arg(u,v) < \pi]$. The numerical computation of $\arg(u,v)$ is implemented in the form of the $\text{ATAN2}(u,v)$ function in nearly every numerical computation package and also is a part of the FORTRAN programming language.

By continuing the algorithm (schematically illustrated in Figure 3-26), a graph or adjacency matrix containing multiple relationships between all projection images recorded can be obtained as depicted in Figure 3-27 and Figure 3-28 where in Figure 3-27 the relationships used and in Figure 3-28 a sample graph obtained are illustrated.

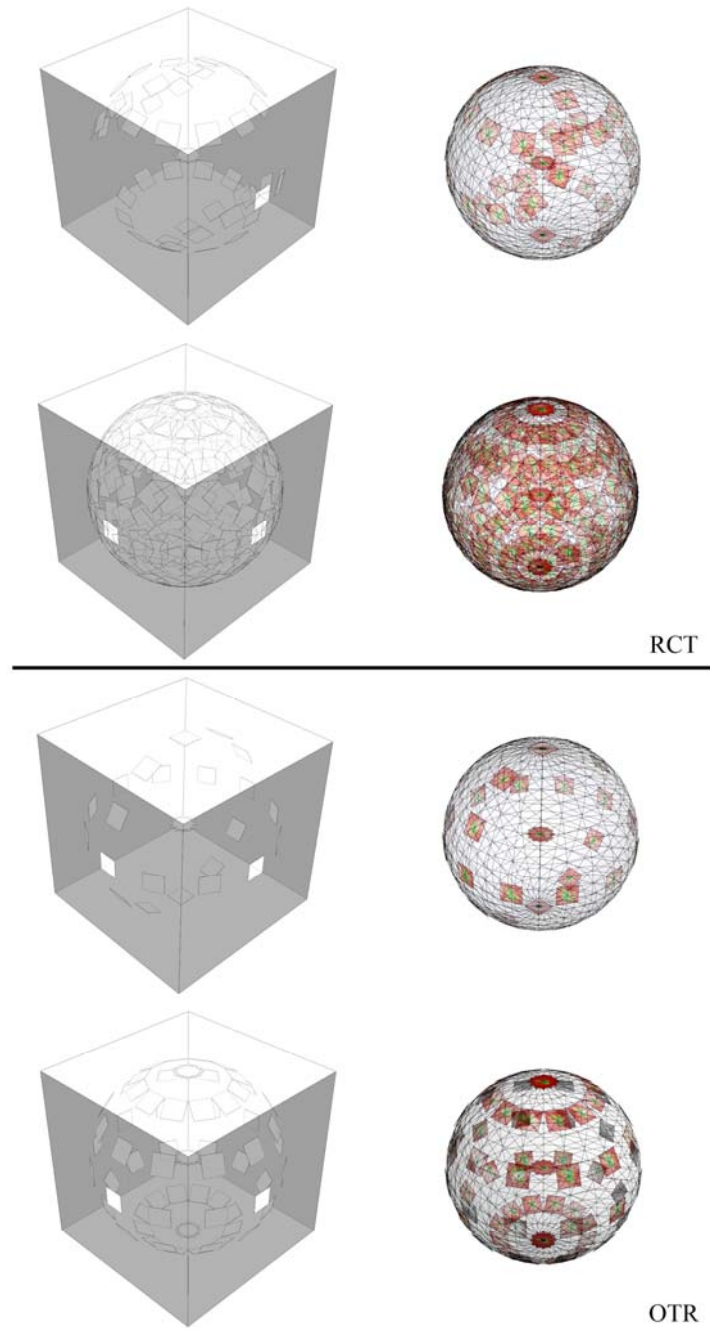


Figure 3-25 Illustration of the new approach, here depicted for image acquisition under RCT (top) and OTR (bottom) conditions. Note that the algorithm can in principal work on any kind of tilted pairs, regardless of the tilt angle. Under the condition that the raw images taken at both tilt states of the specimen holder were classified, each of these tilt mates will now itself be member of a class sum. These class sums members will never be members of the group of tilt mates to the initial class sums, the algorithm started with. (This is a criterion for cross checking of classification.) Each member of the class sum will now again have tilt mates. The halos of tilt mates can therefore be combined within one Euler sphere. The halos orientations depend on the in plane rotation of the respective class members relative to the class sum recorded at the other tilt state of the specimen holder. The orientations are identified by alignment of the class sum to the class member of interest in combination with the experimental tilt angular relationship. Multiple class sums halos of tilt mates can therefore be assigned with projection directions and thus be used for three dimensional reconstructions. Depending on the angular distribution of the tilt mates, a full coverage of the Euler sphere is obtained after few iterations.

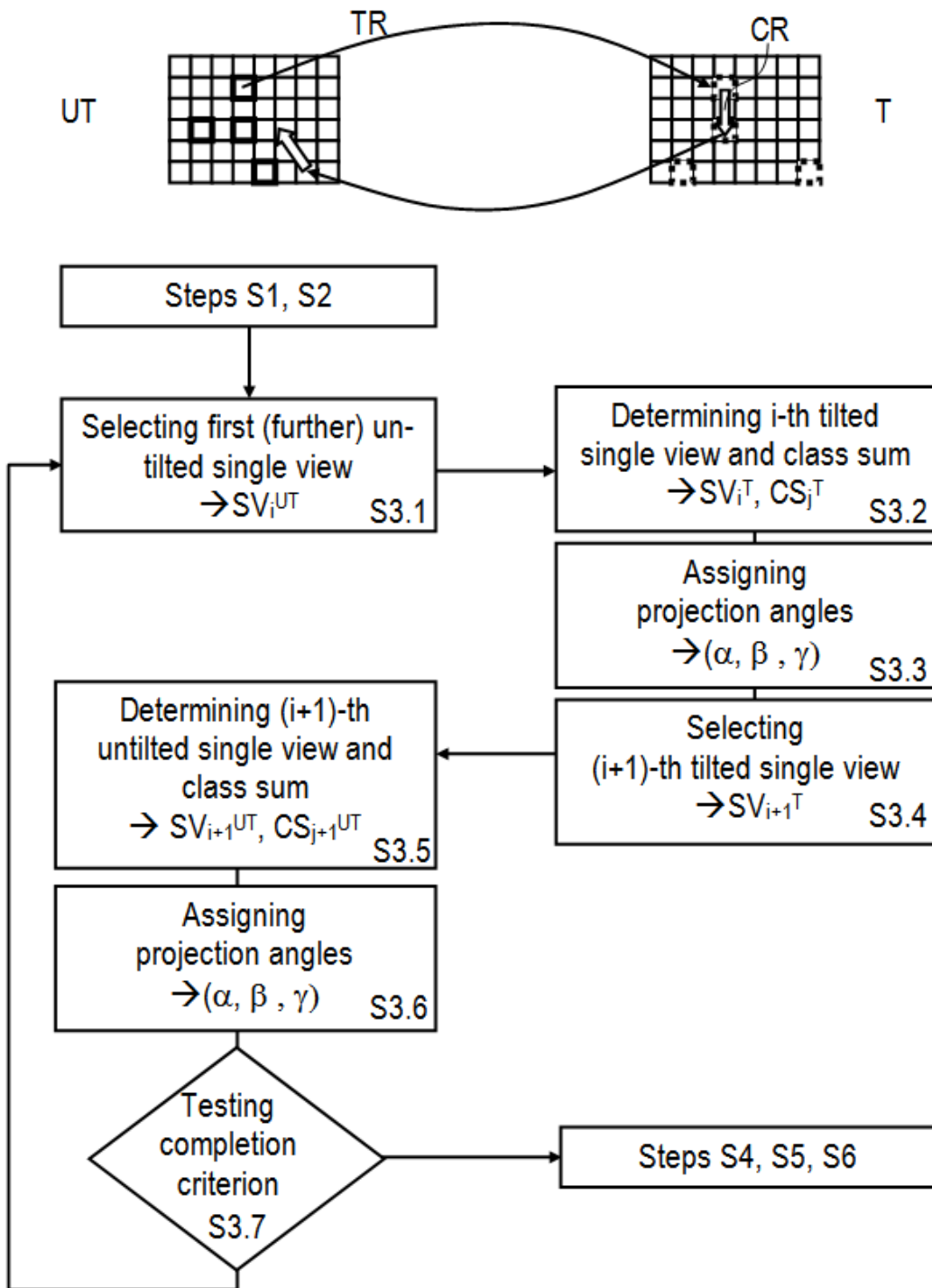


Figure 3-26 A flow chart illustrating details of the algorithm for building a connectivity graph and assignment of projection directions.

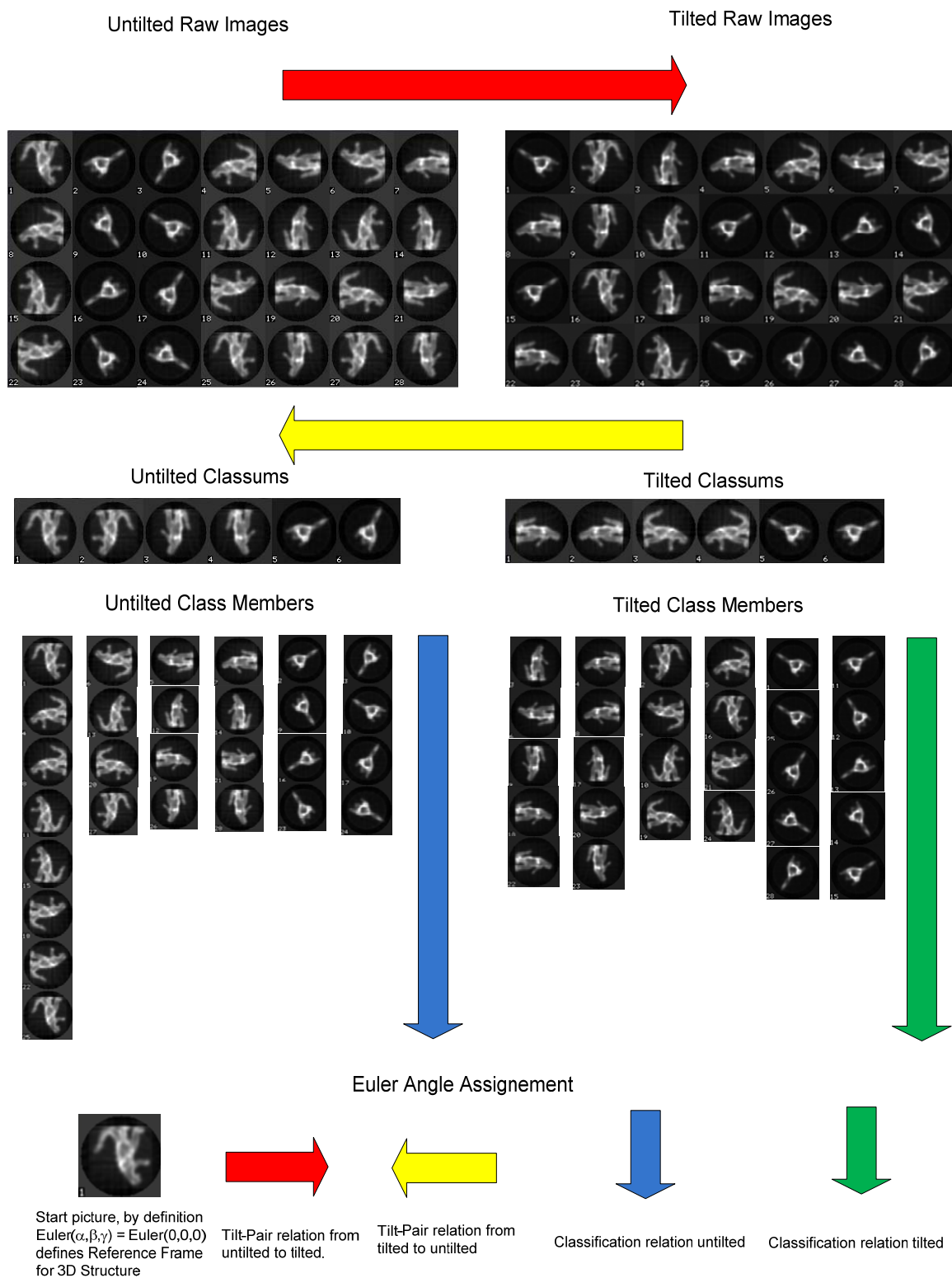


Figure 3-27 Illustration of the relationships utilized for building a connectivity graph and assigning projection directions. In this case obtained by acquisition of tilted pairs and independent MSA and MRA of the views recorded at different tilt settings of the specimen holder.

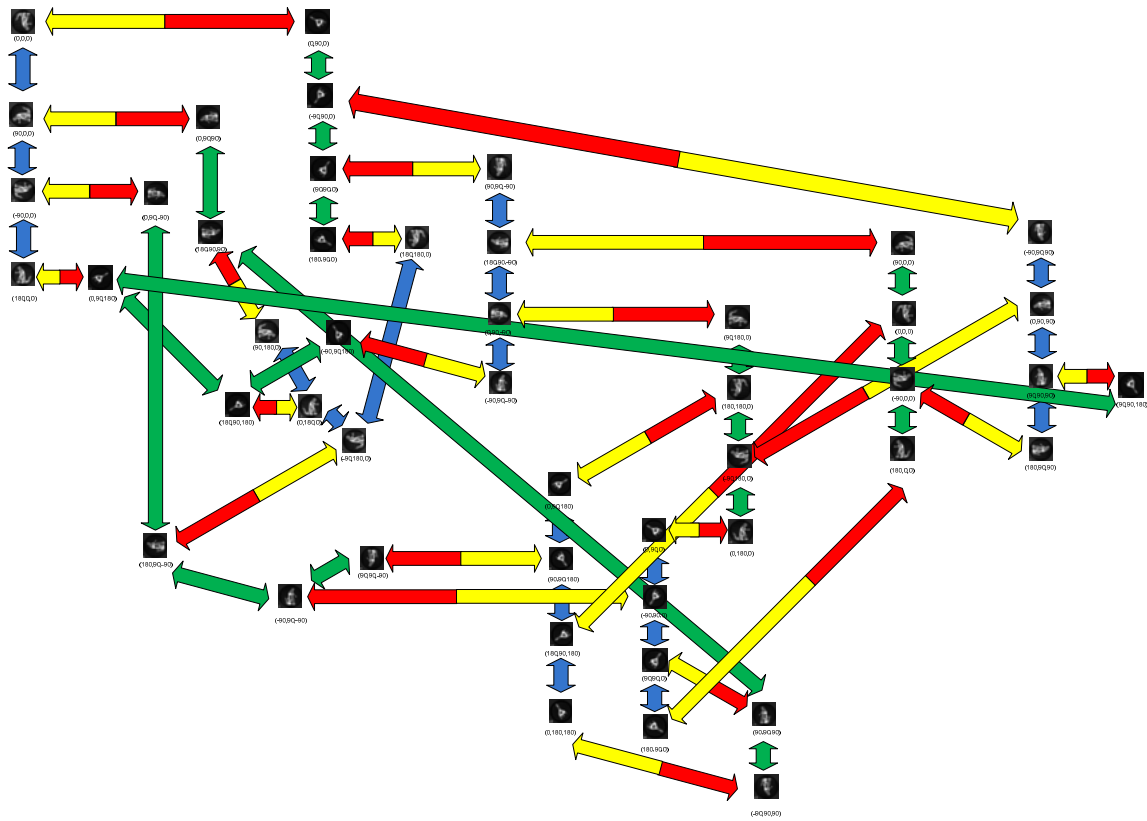


Figure 3-28 A sample connectivity graph obtained combining the alignment and classification relationships. Green arrows indicate a classification relationship among tilted single views, blue arrows between untilted single views. The yellow/red arrows depict a tilt-mate relationship where the yellow tips point to the untilted and the red tip to the tilted single views forming a tilt-mate.

3.3.3 Informative value of connectivity graphs

The tilt-mate relationships identified in the connectivity graph are correct by definition since they are “defined” by the operator. The correctness of the assigned projection directions in respect to the tilt-angle strongly depend on the angular accuracy of the specimen holder used, possible drifting effects, and the correctness of adjustment of eucentric height. With the newest generation of microscopes, combinations of these factors lead to an angular error of the β angle that can be estimated to be $<5^\circ$.

The correctness of the classification relationships strongly depend on the quality of the classification algorithm used, which itself strongly depends on the imaging conditions. Especially the signal to noise ratio obtained is important because the quality of the alignment algorithm used is also sensitive to signal to noise ratio. The quality of the combination of alignment and classification together defines the translational and rotational error range of images within one class sum and whether projection views of conformationally different particles are mistakenly merged within one class sum. Heterogeneity is therefore a prevalent problem that limits full exploitation of cryo-EM data and progress toward higher

resolution (Rye, Roseman et al. 1999; Zhou, Liao et al. 2001; Brink, Ludtke et al. 2004; Burgess, Walker et al. 2004).

Since the SNR of real microscopic data cannot be determined reliably, standard program packages for EM and their classification and alignment performance have been tested on synthetic data of known SNR (Fu, Gao et al. 2007). Best results were obtained by a combination of PCA and K-means clustering. Down to a SNR of 0.07 (which is thought to be in the range of realistic conditions under cryo conditions), a reliable alignment and classification of artificial projection images generated by forward projection could be reliably clustered down to an angular separation of 2° . However, a separation of (major) conformational differences (in this case the presence or absence of EF-G from a density map of a 70S ribosome bound or unbound with EF-G, accounting for $\sim 4\%$ of total mass (Valle, Zavialov et al. 2003)) lead to a drop of classification accuracy to $\sim 82\%$ (Fu, Gao et al. 2007) resulting in classes of mixed conformations, thus correctly aligned translationally and rotationally.

3.3.4 Influences of misclassification and alignment errors on the connectivity graph and assigned projection directions

The building of a connectivity graph may be affected by misclassification resulting in classification and alignment relationships between projection views originating from different conformations. Additionally, the projection directions assigned to projection images may be affected by propagation of alignment errors, demanding a mechanism for identification of misclassified projection views, a mechanism for verification of correct classification and a mechanism for correction of propagating alignment errors.

The information gained by the “double classification” of untilted and tilted views independently can then be used for several purposes. (i) Since multiple relationships are likely to exist twice between untilted and tilted class sums, depending on the number of single views processed and thus the statistics acquired, these relationships can be used to verify outcome of classification and alignment and correct for possible errors. As depicted in Figure 3-29, sub graphs can be verified if a closed loop can be identified in which all classification relationships are supported by tilt relationships which are known to be correct by definition.

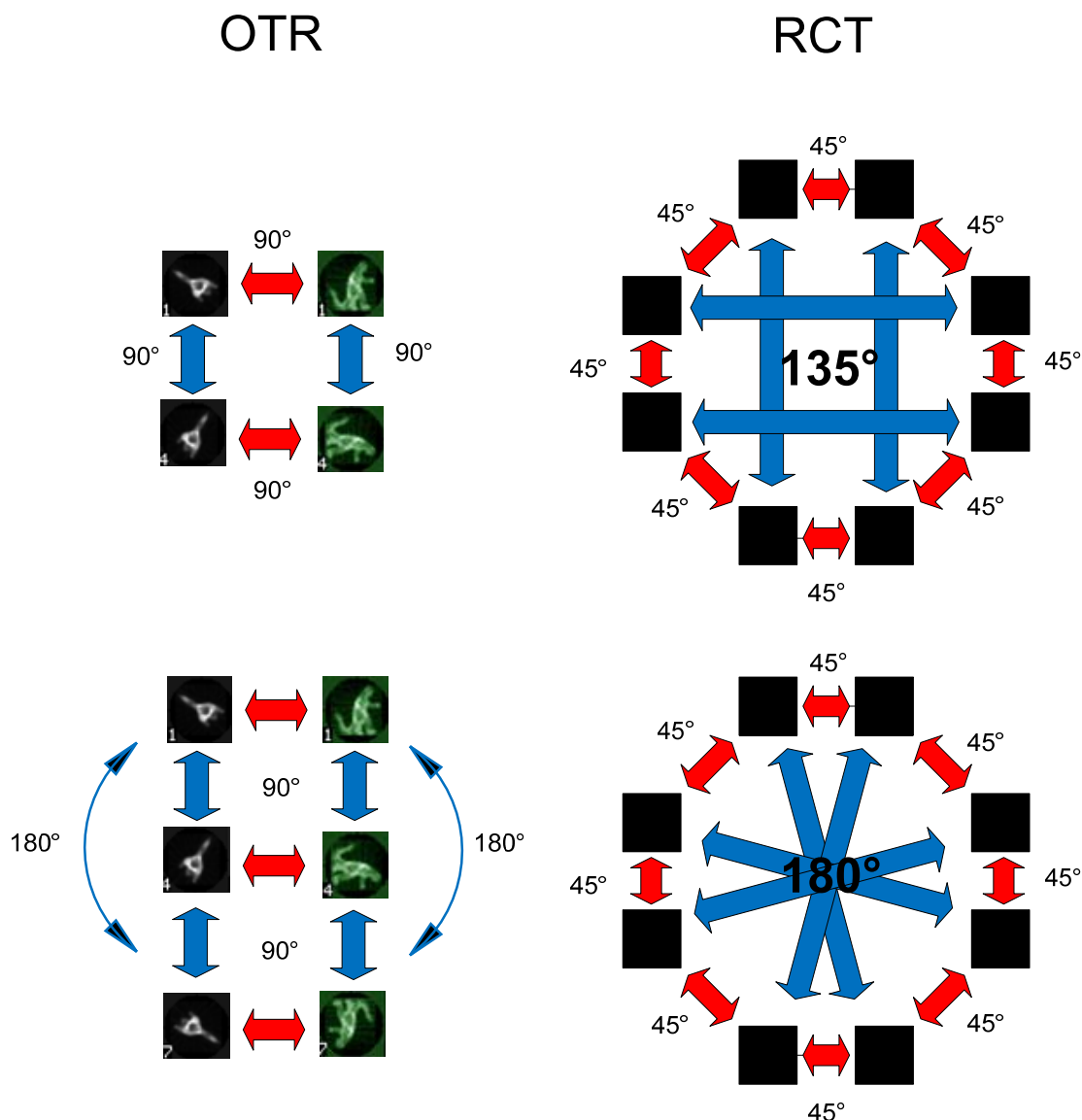


Figure 3-29 Visualization of the criteria for validation of circular sub graphs. If a circular path can be identified in which all classification relationships are supported by tilt relationships which are known to be correct, the relations in the sub graph can be assumed to be correct.

Additionally, statistics can be used to correct for the propagation of alignment and tilt errors. Every single view can be reached by tree traversal of the graph in multiple ways. The projection direction can be assigned independently for every path and i.e. averaged.

3.3.5 Separation of conformational differences

Since published classification and alignment algorithms currently fail to identify small conformational differences reliably for all projection directions, based on the misclassification, images belonging to different conformations will be errantly mixed within one class. If this classification error is not corrected for, the algorithm will merge several

images with similar projection directions in reality belonging to different conformations within one model. If this error is not corrected for, the resulting model obtained will be a consensus model, representing an averaged representation of several conformations. Since classification will not be insensitive to conformational differences for all projection directions, it is unlikely that sub graphs that mix different conformations will be errantly verified. This case can only occur when tilted and untilted views are errantly misclassified in the same way. This property can serve to (i) identify misclassified single views (ii) split up the connectivity graph in sub graphs representing different conformations and (iii) align different conformations in 3D space for further processing by e.g. 3D MSA.

Typical connectivity graphs obtained by the algorithm for underlying classification results are depicted in Figure 3-30 to Figure 3-32. In all cases, exactly two different conformations exist within the data set consisting of tilted pairs acquired under OTR imaging conditions. The reduced number of images for reasons of clear representation leads to a low number of connections. In reality every class sum would consist of ~ 30 class members and ~ 200 class sums would exist. In Figure 3-30, the underlying classification worked perfectly resulting in sub graphs representing the two different conformations separately. Because only 3 projection directions are present resulting in very low statistics, views that would serve to connect sub graphs belonging to the same conformation are missing. Additionally, because no erratic classification occurred, the different conformations are unlinked and no angular relationship exists between them. The outcome is four models representing two conformations that would have to be 3D aligned before further analysis. In Figure 3-31 the case of an underlying systematic misclassification for one view in each tilted and untilted class sums is illustrated. The erratic classification relationships remain unverified and the conformations can be split up. Additionally, the erratic classifications relationships can serve to 3D align the different conformations for further analysis. Due to the missing links caused by insufficient statistics, two pairs of models representing different conformations are the outcome, already 3D aligned for further analysis. In Figure 3-32 the case of an underlying cross misclassification is illustrated. For two tilted and untilted class sums each, not only an erratic merging of views belonging to different conformations but also a cross misclassification is illustrated (this being the most realistic case.) Another method for the separation of conformations is illustrated, solely based on statistics. The number of tilt relations between class sums is counted and a threshold value is then used to only consider class sums connected by a user defined number of tilt relations as belonging to the same conformation. This threshold value can be user-adjusted depending on the underlying data.

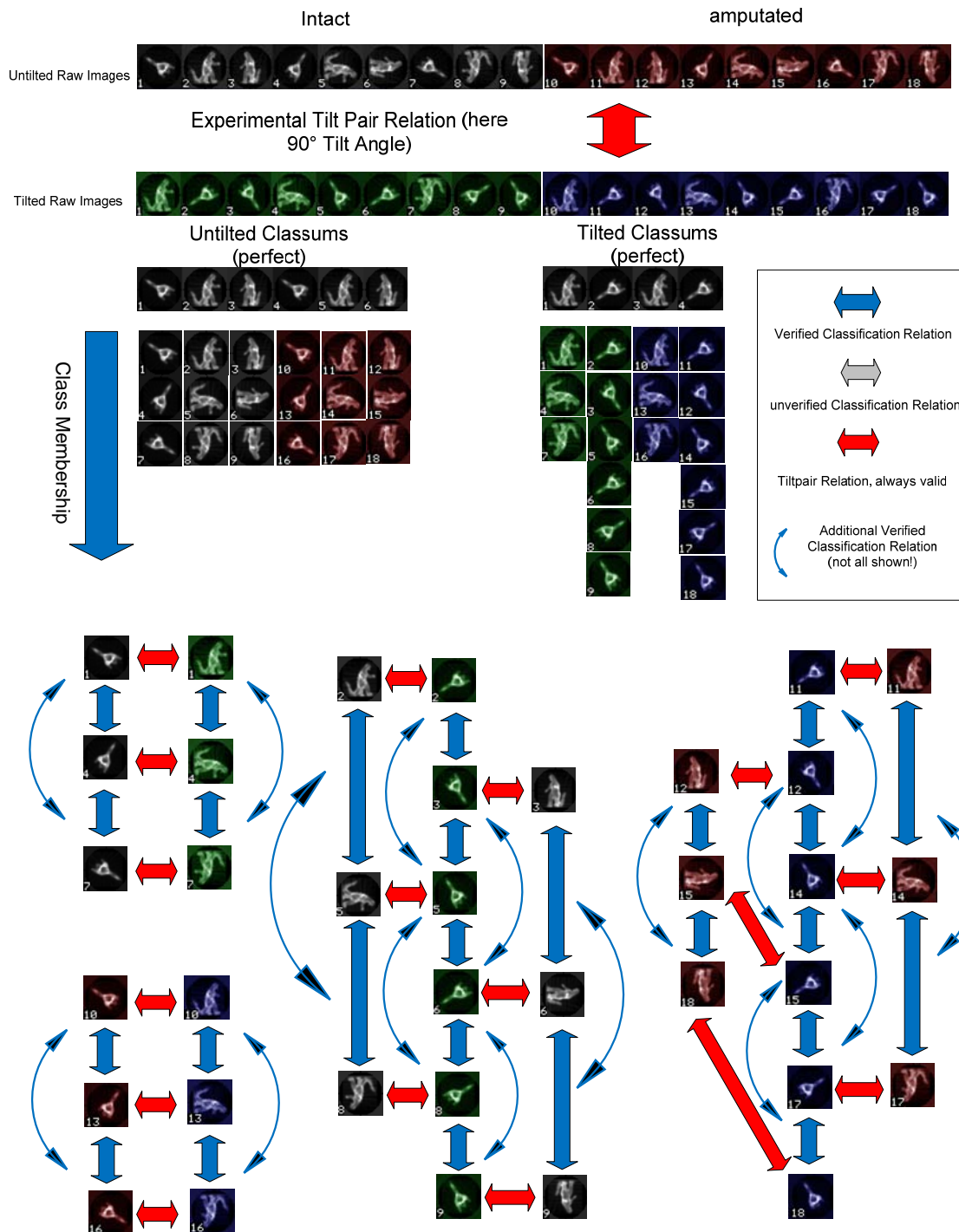


Figure 3-30 Connectivity graph obtained from a data set consisting of two conformation depicted here for the case of perfect underlying classification. The result are sub graphs representing the two different conformations separately. Because only 3 projection directions are present, resulting in very low statistics, views that would serve to connect sub graphs belonging to the same conformation are missing. The outcome are 4 models representing 2 conformations that still have to be 3D aligned for further analysis.

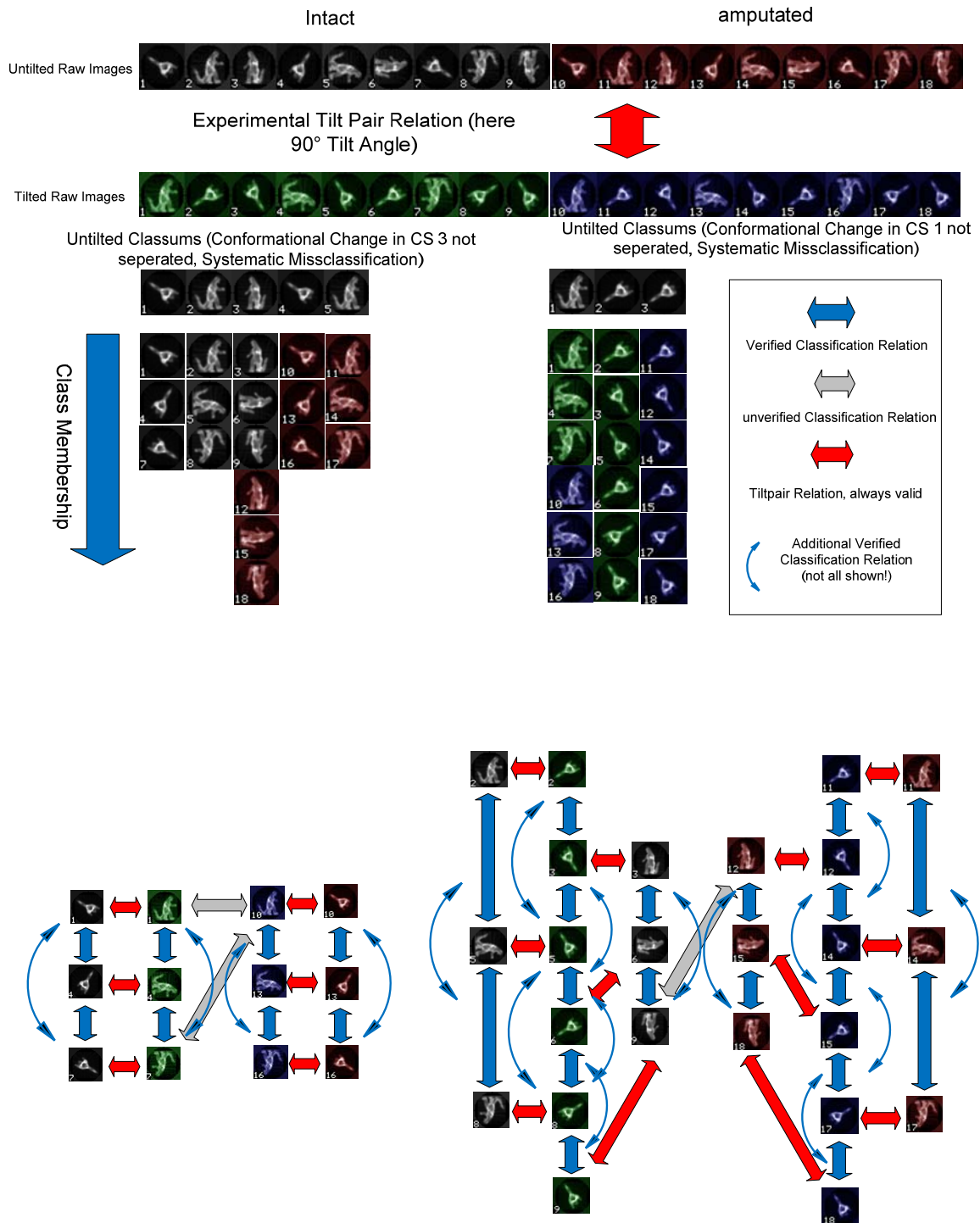


Figure 3-31 Connectivity graph obtained from a data set consisting of two different conformations depicted here for the case of an underlying systematic misclassification for one view in each tilted and untitled class sum. The erratic classification relationships remain unverified and the conformations can be split up. Additionally, the erratic classifications relationships can serve to 3D align the different conformations for further analysis. Due to the missing links caused by insufficient statistics, two pairs of models representing different conformations are the outcome already 3D aligned for further analysis.

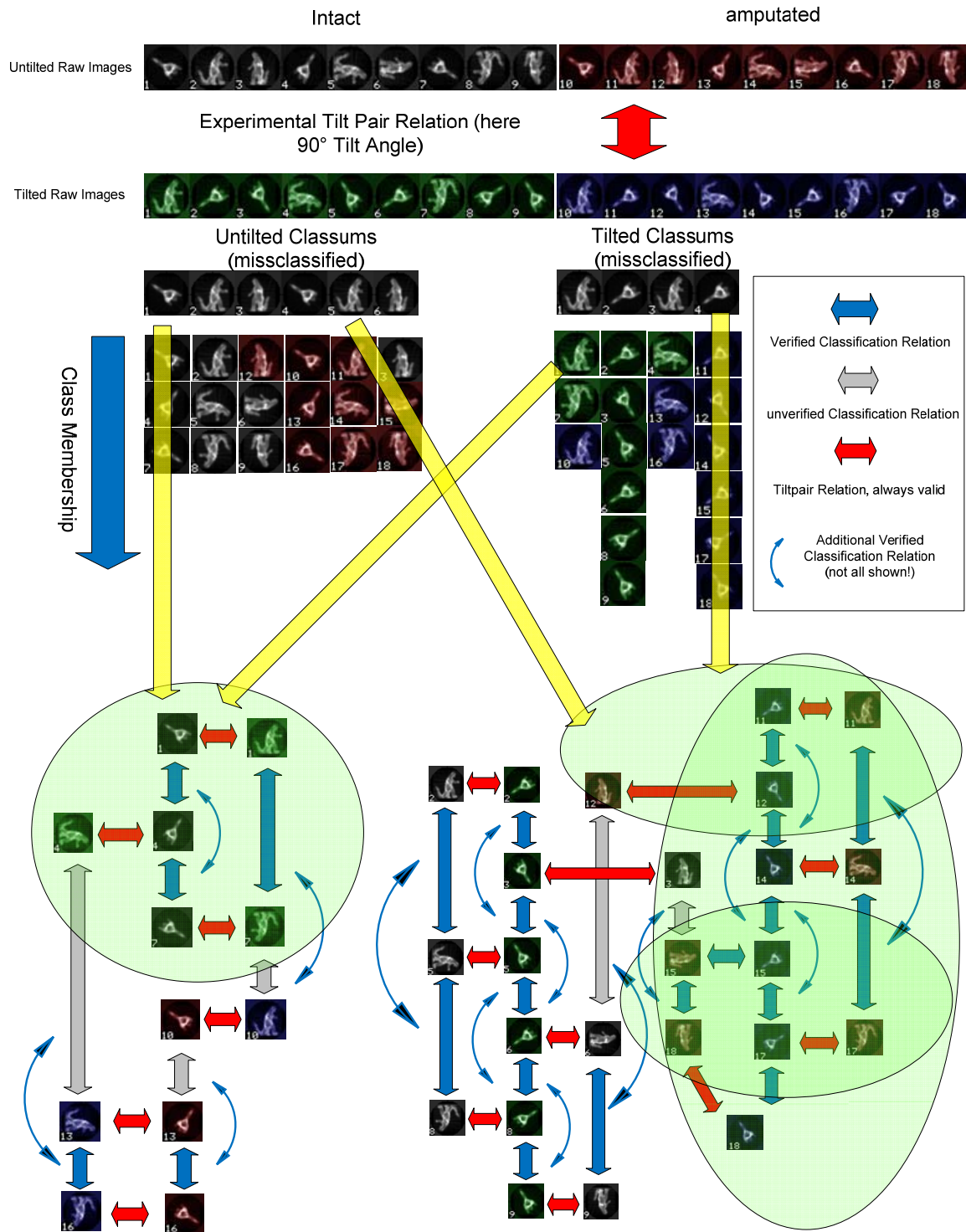


Figure 3-32 Connectivity graph obtained from a data set consisting of two conformations depicted here for the case of an underlying cross misclassification. For two tilted and untitled class sums each, not only an erratic merging of views belonging to different conformations but also a cross miss classification is illustrated (this is the most realistic case). A quick statistics-based method for the separation of conformations is also illustrated. The number of tilt relations between class sums is counted and a threshold value is then used to only consider class sums connected by a user defined number of tilt relations as belonging to the same conformation.

3.3.6 Influence of alignment and tilt errors on reconstructed starting models

In addition to the overall image quality of recorded projection views dependent on SNR, aberrations, defocus and drifting effect, the quality of classification, translational and rotational alignment as well as accuracy of tilt angle assignment strongly influence the quality of reconstructed starting models. While alignment and classification quality depend on the overall imaging quality itself, tilt angle accuracy mostly depends on the quality of instrumentation e.g. the compustage used in combination with the accuracy of the adjustment of eucentric height. Because imaging quality and quality of alignment and classification of experimental data depends on a vast number of parameters and cannot be accurately determined in the case of imaging of biological objects, simulations were performed using synthetic data of defined properties in respect to translational and angular errors. The goal is to identify the influence of individual error sources on the quality of the reconstructed starting models comparing RCT and the newly developed method. Therefore, synthetic tilted pairs of varying quality in respect to translational and angular errors were generated by forward projection of given volumes followed by 3D reconstruction using RCT and the new method. The influence of noise was found to mainly affect the quality of alignment and classification. Additionally, a linear degradation of 3D quality could be observed that could be compensated for by increasing the number of class members per class sum and thus improving the SNR of class sums for reconstruction. The influence of noise is therefore ignored in the following simulations. The number of class members of class sums and therefore the number tilted pairs used in the simulation was chosen by the demands of the RCT approach. The class size was chosen depending on the desired average angular distance of tilted single views to attend a uniform azimuthal spacing of the tilt mates to a untilted class sum used for the RCT reconstruction. In addition to visual inspection, the 3D CCC of reconstructed volumes compared to the model used for generation of the tilted pairs was calculated. In Figure 3-33 the ideal case is illustrated comparing RCT reconstruction and reconstruction using the new method for different average angular distances of the projection views. While volumes computed using the RCT reconstruction method suffer from an elongation along the missing cone in addition to resolution limits resulting from the constricted angular range covered, models computed using the new method only depend on the angular distance of projections, not aggravated by a missing cone of information.

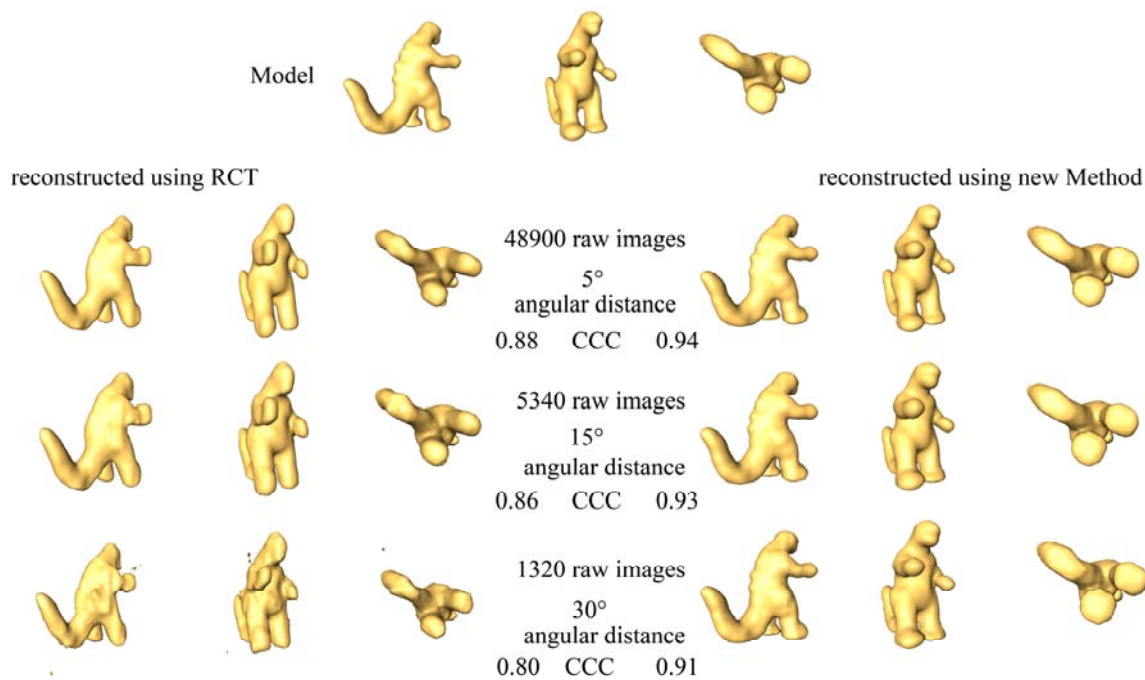


Figure 3-33 Models obtained by processing tilted pairs using the RCT reconstruction method (left) and the newly developed reconstruction method based on the connectivity graphs (right). Here the ideal case is illustrated for perfect classification and alignment, differing in the average angular distance of tilted pairs used. In addition to imperfections originated at the constricted angular coverage, RCT models are additionally elongated in the direction of the missing cone. The CCCs were computed in comparison to the 3D model used for the generation of tilt mates.

The influence of angular and translational alignment errors as well as an inaccuracy of tilt angle assignment is illustrated in Figure 3-34. The influence was analyzed for combinations of translational error in the range of 0-30% in respect to the particle radius, angular alignment errors of 0-20° and a tilt inaccuracy of 0-20° as depicted in Figure 3-35 to Figure 3-36. The distribution of errors was uniformly dispersed amongst generated projection views. The most severe influence on reconstructed 3D volumes was observed for translational alignment errors, followed by rotational alignment errors. The tilt inaccuracy was observed to have the lowest absolute influence on the quality of reconstructed volumes. The analyzed errors exceed errors occurring in reality. For the new method, angular error propagation was compensated for by averaging of assigned projection directions obtained from multiple relationships as present in the underlying data. In Figure 3-36 a comparison to the quality of models obtained from RCT reconstruction using an average angular distance of 30° without errors is depicted. These conditions proved to be sufficient for refinement of the starting model by projection matching without bias from an erratic starting model. The influence of translational alignment has a severe effect on volumes reconstructed using the new method. This effect is originated in the missing correction for translational errors and thus a

propagation of these in the form of erratic angular assignments throughout the whole connectivity graph. However, alignment algorithms used in combination with accurately centered particles do not generate severe translational errors. In practice it can be observed that CCC based methods deliver translational alignment accuracy < 2 pixels which is far below 5% in most cases, depending on the pixel frame and particle radius used. Projections generated from different conformations can be observed to translate to a rotational alignment error using CCC based methods, but the angular alignment error can still also be assumed to be far below 5° . Additionally, new methods of alignment and classification being developed right now within the Stark Lab (unpublished work) are promising to deliver angular alignment accuracy $< 1^\circ$ including high sensitivity for conformational changes and translational alignment accuracy in the sub-pixel range.

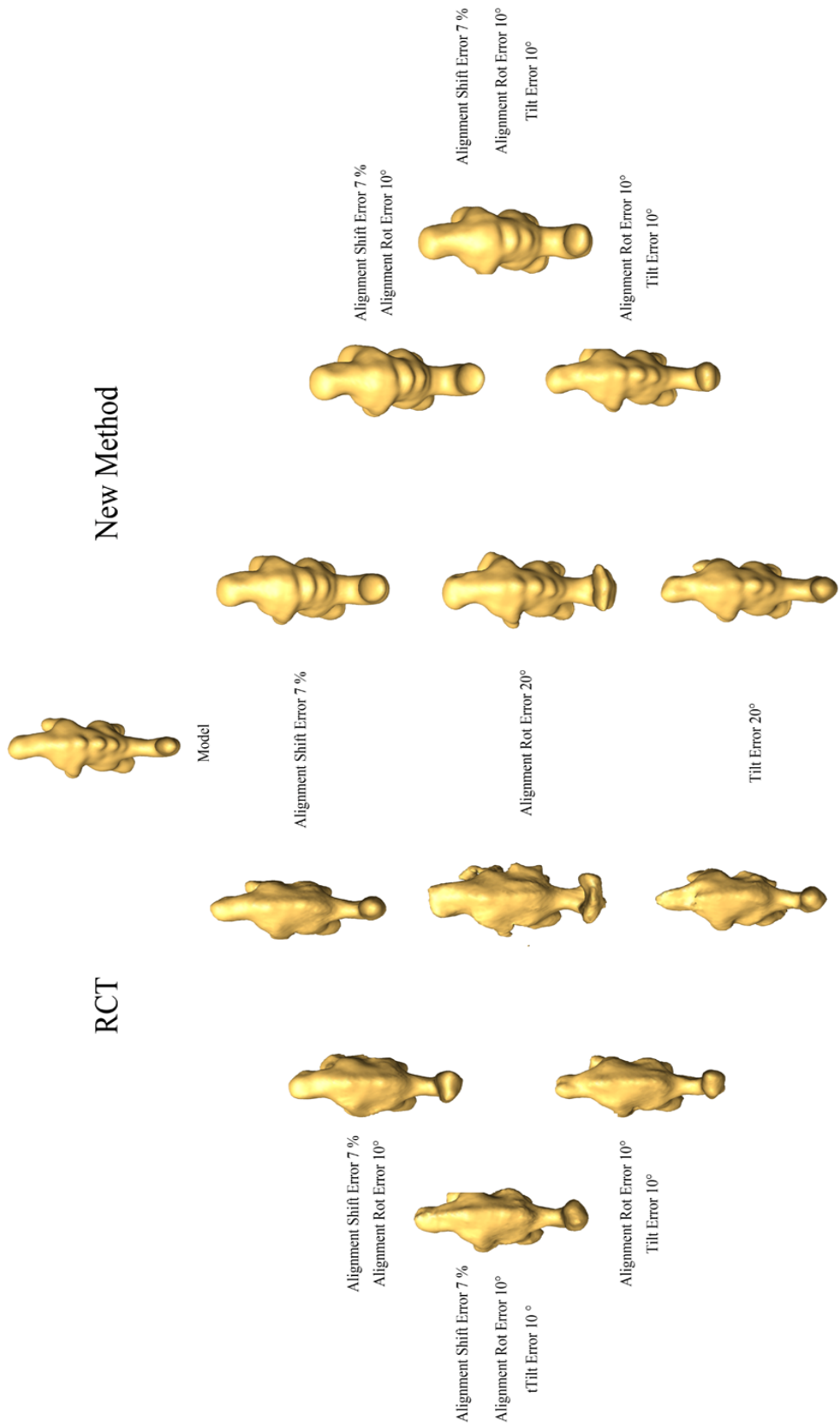


Figure 3-34 Visualization of the influence of translational and rotational alignment inaccuracy as well as tilt angle accuracy on models obtained using the RCT and the newly developed reconstruction techniques.

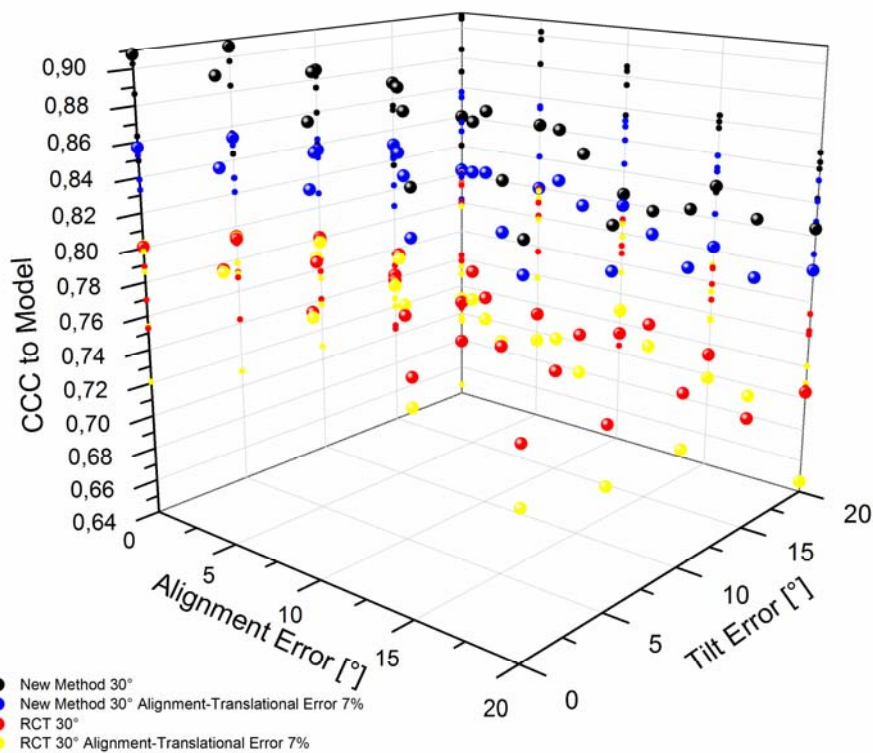
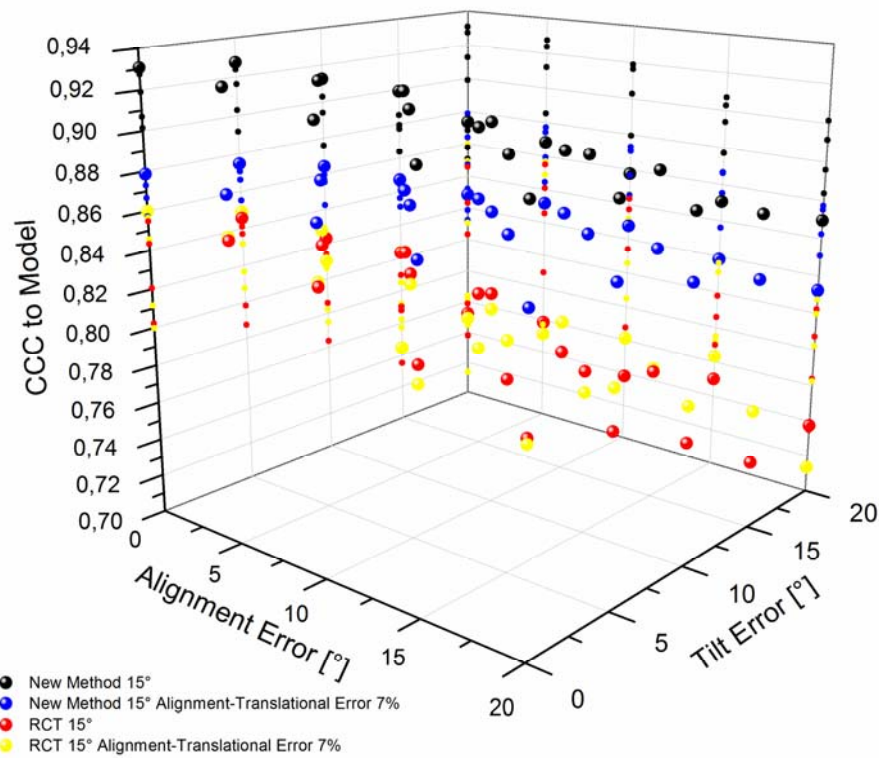


Figure 3-35 Comparison of quality of models obtained by reconstruction from tilted pairs with known alignment and tilt inaccuracy. The CCC was computed in comparison to the model used to generate the tilted pairs used for the reconstruction by forward projection. The case of an average angular distance of tilted pairs of 15° is depicted in the top plot. The bottom plot depicts an average angular distance of 30°.

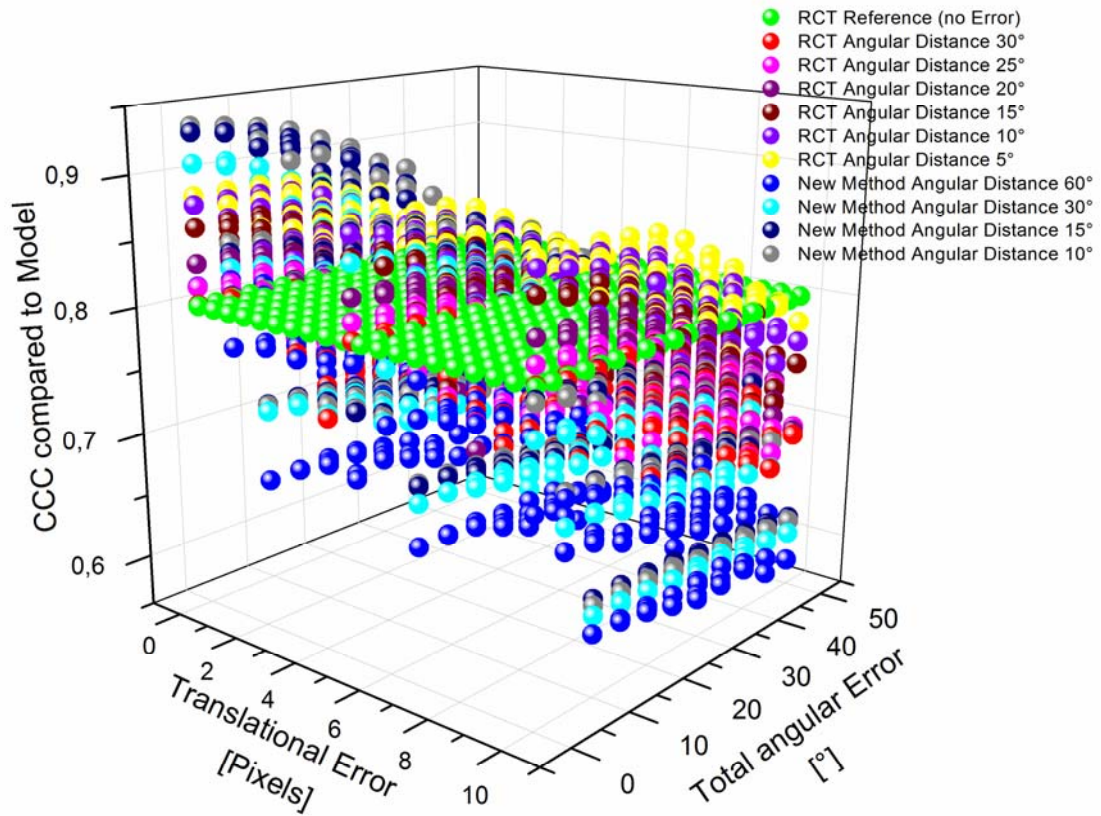


Figure 3-36 Comparison of reconstructed models quality obtained from RCT reconstruction and newly developed reconstruction method. The particle radius was 32 Pixels. The green spheres indicate the quality of a best case RCT model obtained from tilted pairs with an average angular distance of 30°. This reference proved to be sufficient for refinement of the starting model by projection matching without bias from an erratic starting model. The newly developed method was applied here without any error correction leading to a propagation of errors. Nevertheless, the new method delivers higher quality starting models even without error correction as long as the underlying alignment and tilt accuracy is kept in reasonable ranges which can be easily obtained using high performance alignment algorithms and the newest generation of microscopes.

4 Discussion

In cryo-electron microscopy (cryo-EM) single-particle reconstruction, the heterogeneity of two-dimensional projection image data resulting from the co-existence of different conformational or ligand binding states in addition to different states of integrity caused by purification and sample preparation of a macromolecular complex remains a major obstacle. It impairs the validity of reconstructed density maps and limits the progress toward higher resolution. Particles that additionally tend to orient in a preferred way in the EM sample such as the Acetyl-CoA Carboxylase, were studied as a heterogeneous test object in this thesis. These particles can be analyzed and insight into their overall properties can be gained. The loss of subunits during purification, not leading to a disabling of enzymatic activity is revealed, but a high resolution 3D structure cannot be obtained using established techniques.

Nevertheless, single particle Electron Microscopy is the method of choice for structure determination of large macromolecular complexes that are difficult to purify in the amounts and quality needed for X-ray crystallization. In contrast to other structure determining techniques, single particle cryo-EM is not an ensemble technique. Images of individual macromolecular complexes are recorded that can potentially be used to detect structural variations within a single dataset which is highly important for structure determination of large and dynamic macromolecular assemblies. Using currently available technologies, sample heterogeneities are considered as one of the factors most limiting resolution since appropriate methods for computational separation of images representing different conformations of macromolecules without any prior knowledge of the molecule are basically missing.

Here a new method is described that can be used to study heterogeneous samples in a mostly user independent manner, allowing 3D structure determination of a set of 3D structures from a single data set that best reflects the structural and conformational dynamics of macromolecules and thus describes the functionally important behavior of a given macromolecule in solution. Generating reliable initial models is a critical step in the reconstruction of asymmetric single-particles by 3D electron microscopy. This is particularly difficult to do if heterogeneity is present in the sample. The Random Conical Tilt (RCT) method (Radermacher, Wagenknecht et al. 1987), arguably the most robust established method to accomplish this task, requires significant user intervention to solve the “missing

cone” problem. A novel approach is presented here, which eliminates the missing cone and facilitates the separation of conformations that are still mixed due to an erratic 2D classification. This method is capable of correcting for 2D rotational alignment inaccuracies, and makes it possible for multiple multi-class-volumes to be computed separated into different conformations. These models can be used directly for further analysis by e.g. 3D MSA. Depending on the data set acquired, and the underlying statistics, e.g. the number of orientations on the grid, the models can either be used directly without the need of a 3D alignment, or if such an alignment is still necessary, without a systematic cone impeding 3D alignment. 3D MSA and classification are powerful tools to analyze the heterogeneity present in a sample, provided a method exists to identify a sufficient number of relatively homogeneous volumes to be used in this analysis. Comparisons among individual reconstructions by 3D MSA and classification are complicated by the presence of a missing wedge or cone and a relatively low signal-to-noise ratio (SNR) (Walz, Typke et al. 1997; Iwasaki, Mitsuoka et al. 2005). Due to the multi class sums generated by the new approach with increased SNR and no systematic missing cone, this limitation can be overcome. The models that are obtained can thus be used directly as initial references in refinement without further processing. The method involves collecting data at two different tilt stages of the specimen holder, under cryo conditions with high accuracy of eucentric height, tilt angular setting and defocus correction. With these prerequisites fulfilled, data collected at both tilt states of the specimen holder can be classified and aligned independently. The parameters obtained by this double classification of the data in combination with the experimentally defined tilt angular and tilt-mate relationships serve to build up a connectivity graph that can be used to (i) assign projection directions for 3D reconstruction to multiple single views and class sums, belonging to the same conformational state. (ii) Identify misclassified single views and thus (iii) separate different conformational states. The need for data acquisition under cryo conditions originates from the property of negatively stained particles to have been shown to be affected by significant flattening (Carazo, Wagenknecht et al. 1989; Boisset, Taveau et al. 1990). When this is the case, classification of projection views recorded with a tilted specimen holder is difficult if not impossible. This results from the fact that although two flattened particles related by an in-plane rotation on the grid yield the same projection when imaged untilted, they result in *different* projections once the sample is tilted. Because the new method relies on the classification of projections obtained from a tilted sample, such a pair of particles would not be expected to classify together. Particles embedded in vitreous ice are not affected by flattening (Frank, Penczek et

al. 1991). Another method targeted at elimination of the missing cone is the OTR approach (Leschziner and Nogales 2006) proposing image acquisition at -45° and $+45^\circ$ resulting in an effective tilt angle of 90° and thus no missing cone as already proposed in (Stoops, Momany et al. 1991). This method is thought to be applicable under negative stain conditions in an ideal situation: a class showing an even distribution of rotations from the 2D alignment of (tilted) particles should only contain particles mostly unaffected by flattening. The difficulty of collecting tilted data under cryo-EM conditions, thought to be an obstacle to become a practical approach (Leschziner and Nogales 2006) is resolved using the newest generation of cryo Electron Microscopes, featuring high stability cryo stages. The separation of conformations is based on the property that different conformations might lead to similar projection views for some but not for all projection directions. This misclassification will be sample dependent: images with higher signal to noise ratio, or particles with strong features, rather than globular, should experience a much reduced rate of misclassification. Clearly, the separation of conformations will be less effective in any situation where the heterogeneity is continuous rather than discrete. In this case the worst case is no separation of conformations but the computation of a consensus model with full coverage of reciprocal space, representing different minor merged conformational states, which can still be utilized for further analysis such as supervised classification.

It is obvious that the new method would benefit from large data sets; a larger number of particles would enable one to generate a larger number of single class volumes of increasing resolution and this would in turn facilitate the identification and characterization of any heterogeneity present in the sample. Larger data sets would also benefit the procedure used for increasing the homogeneity of individual class volumes in those cases where the sample is heterogeneous. Larger data sets require an automated way of image acquisition and processing which in addition to the requirements to instrumentation which can be fulfilled using the newest generation of microscopes, increases the demands regarding computational processing power and speed leading to restrictions by computational demands. Recent developments in information technology such as Multicore, Parallel, GPU processing and farming can be used to overcome these limitations. Especially Graphics Processing Units (GPUs), originally developed for rendering real-time effects in computer games, are now ubiquitous and provide unprecedented computational power for scientific applications. Each parallel processing paradigm alone can improve overall performance, while combining all paradigms, unleashes the full power of today's technology. The increased computational

performance makes certain applications feasible that were virtually impossible before. The preferred trend of increasing CPU core count over execution speed is very likely to continue in the future. Algorithms only benefit from these state of the art processing paradigms if they are recoded to fit these new paradigms. Therefore, the next generation of CPUs will not significantly speed up existing applications if they are not prepared to harness the power of additional cores. Further, commodity graphics hardware is evolving to become a new generation of massively parallel streaming processors for general purpose computing. Scientists and developers are challenged to port existing applications to the new data parallel computing paradigms and to introduce as much concurrency in the algorithms as possible (if possible, using one thread per data element). This strategy guarantees optimum scaling with core count. Additionally, hardware such as GPUs can and should be included either at the level of desktop computers but also even up to dedicated GPU cluster solutions. Today these new paradigms are still hardware dependent, but there are first indications that this will change within the near future (Hou, Zhou et al. 2008; Munshi 2008; Stratton, Stone et al. 2008). Currently, one still needs to be prepared that entering GPU computing may require rewriting the code partially for the next hardware generation. Nevertheless, this can be expected to be rather trivial because the data parallel approach is not likely to change dramatically over time. The technology exists to harness today's state of the art system architecture for at least one full compute cluster duty cycle from commissioning to the end of the financial amortization. Approaches such as OpenCL, MCUDA or BSGP target these architectures and are also prepared for interesting Intel's and AMD's GPU/CPU developments of hybrid or extreme multicore architectures that will soon enter the market. Larrabee for Intel (Seiler, Carmean et al. 2008) and Fusion from ATI are targeted to recapture market shares from GPU manufacturers and in visual computing. No matter how powerful GPUs may be for general purpose computations, they are still a workaround and no panacea. Especially when irregular data structures are needed or scatter gather operations cannot be avoided, GPU programming is suboptimal because of the fixed function logic. Nevertheless, a lot of high performance and high throughput calculations can be speeded up significantly using GPUs although a hardware and platform independent technology is not available until hardware manufacturers and/or operating system manufacturers involved agree on a common API that does not depend on the selected hardware. In the long run it is very likely that companies such as Intel or AMD will (re-)enter the data parallel market. Intel already released a new compiler generation called High Performance, Parallel Optimizer that is capable of auto vectorizing and auto parallelization, which utilizes loop

unrolling and peeling. A great deal of workloads were analyzed by Intel including well-known HPC kernels like 3D-FFT and BLAS3, converging towards a common core of computing (Chen, Chhugani et al. 2008). This approach shows great potential for a common run time, a common programming model and common compute kernels, data structures and math functions. Once these steps are complete, the code generation for a specific platform being CUDA / CTM or Larrabee / Fusion is a political and marketing but not an academic problem.

In summary, it is still too early to tell which API or programming model will succeed in the long run, but today's technology can be already utilized. The trend is set, get ready for the data-parallel Multicore age (Che, Boyer et al. 2008) and exploit as much concurrency in algorithms as possible. Single particle cryo-EM is certainly one field where GPU computing currently pays off. There are now electron microscopes that allow data collection to be completely automated. In combination with fast and large detectors, these instruments can produce massive amounts of data within a very short amount of time. In the best case one can expect such microscopes to collect up to several million particle images within a week. To collect this huge amount of data is only reasonable if the computer infrastructure needed for processing this data is powerful enough to keep up with data collection. In the cryo-EM field it is thus almost impossible to rely only on CPUs alone. In contrast, the massive increase in computation speed that can be achieved on GPUs for most of the embarrassingly parallel applications needed in single particle cryo-EM image processing makes the computational analysis of millions of images possible on a medium sized GPU cluster. For compute intense applications such as single particle cryo-EM, GPUs are thus the only option, simply because of the lack of any other affordable alternatives. In single particle cryo-EM the most compute intense applications are image alignment of a large number of randomly oriented macromolecules imaged in the electron microscope and the 3D reconstruction using these aligned images.

The SmartTray framework presented in this work can be used to run a dynamic cluster, featuring e.g. compute nodes partly equipped with CUDA enabled GPUs. Three-dimensional reconstructions using the simultaneous iterative reconstruction technique (SIRT) algorithm e.g. can be speeded up by a factor of ~ 65 comparing one CPU to one GPU using a pixel frame of 64×64 . Scaling up to multiple nodes was observed to follow Gustafson law for 3D reconstruction and alignment. Large image statistics and pixel frame sizes can

thus be handled by adding further nodes to the computations. The speedup of image alignment is more difficult to measure because the actual alignment algorithms implemented on CPU and GPU are also significantly different. Additionally, there is a significant dependence of the measured speedup on the image size. Using small images (like 64x64 pixels) the speedup on the GPU compared to the CPU is almost negligible. However, for high resolution 3D structure determination high image statistic needs to be combined with small pixel sampling. Theoretical considerations assuming an ideal sample, imaging conditions and instrumentation predict that a projection structure at 3 Å can be obtained by averaging of ~13000 asymmetric subunits (Henderson 1995; Glaeser 1999; Glaeser 2004). In reality, neither the sample nor the instrumentation are ideal and affect the quality of acquired projection images. Therefore, practical experience (Gabashvili, Agrawal et al. 2000; Unwin 2003; Ludtke, Chen et al. 2004) points toward a requirement of ~50,000 particle images to reach a resolution below ~10 Å, which is necessary to resolve α -helices. It is predicted that to produce a statistically well defined 3D reconstruction at a resolution high enough to trace a polypeptide chain (e.g. ~3 Å), more than ~1,000,000 particle images need to be considered. For high resolution studies of most macromolecules millions of raw images at a pixel frame size in the range of 256 x 256 pixels and 1024 x 1024 pixels are thus to be expected. Using these larger images the measured speedup of GPU computing is in the range of 10-100 times allowing determining high-resolution 3D structures by single particle cryo-EM in an acceptable time frame.

The newly developed reconstruction method can thus benefit from increased statistics and alignment accuracy and thus multiple SNR improved multi class volumes, separated for conformational differences with known relative orientation can be reconstructed. The prerequisites to apply this technique regarding tilt stage and alignment accuracy were analyzed and can be routinely fulfilled using a modern electron microscope with a highly stable cryo specimen stage in combination with state of the art alignment and classification algorithms speeded up by state of the art parallel processing software and hardware. The traditional approach of combining the particle images within one single reconstruction can thus be overcome. The novel strategy is intended to gain insight into the 3D structures and structural diversity of so-far poorly characterized dynamic assemblies in a user independent way. Snapshots of different conformations are provided and can therefore reveal dynamic states that are elusive to any standard technique in structural biology. Overall, these methodological advances open new perspectives for the decryption and quality evaluation of

3D structure dynamics of complex and fugacious macromolecular machines. With the setup of the newest generation TEM, a FEI Titan Cryos in the Stark Lab completed, in combination with the in place GPU compute cluster, the prerequisites to apply the new algorithm to experimental data are fulfilled. Simulations performed indicate that the new method will deliver reliable starting models separated for conformational states, as long as alignment and tilt accuracy are kept in ranges that can easily be obtained by the combination of state of the art instrumentation as well as established and emerging alignment algorithms.

5 Bibliography

Abbe, E. (1873). Beiträge zur Theorie des Mikroskops und der mikroskopischen Wahrnehmung. Arch. Mikroskop. Anat. **9**: 413-420.

Adrian, M., J. Dubochet, J. Lepault and A. W. McDowell (1984). "Cryo-electron microscopy of viruses." Nature **308**(5954): 32-6.

Adrian, M., B. ten Heggeler-Bordier, W. Wahli, A. Z. Stasiak, A. Stasiak and J. Dubochet (1990). "Direct visualization of supercoiled DNA molecules in solution." EMBO J **9**(13): 4551-4.

Amdahl, G. M. (1967). Validity of the single-processor approach to achieving large scale computing capabilities. Proceedings of AFIPS Conference.

Anderson, D. P. (2004). BOINC: A System for Public-Resource Computing and Storage. GRID '04: Proceedings of the Fifth IEEE/ACM International Workshop on Grid Computing, IEEE Computer Society: 4--10.

Beckmann, R., R. Bubeck, R. A. Grassucci, P. A. Penczek, A. Verschoor, G. Blobel and J. Frank (1997). "Alignment of conduits for the nascent polypeptide chain in the ribosome-Sec61 complex." Science **278**(5346): 2123-2126.

Beguelin, A., J. Dongarra, A. Geist, R. Manchek and V. Sunderam (1991). A User's Guide to PVM Parallel Virtual Machine, University of Tennessee.

Bilbao-Castro, J. R., J. M. Carazo, J. J. Fernández and I. García (2004). "Parallelization and Comparison of 3D Iterative Reconstruction Algorithms" 12th Euromicro Conference on Parallel, Distributed and Network-Based Processing: 96.

Boersch, H. (1947). "Über die Kontraste von Atomen im Elektronenmikroskop." Z. Naturforschung(2a): 615.

Bohm, J., A. S. Frangakis, R. Hegerl, S. Nickell, D. Typke and W. Baumeister (2000). "Toward detecting and identifying macromolecules in a cellular context: template matching applied to electron tomograms." Proc Natl Acad Sci U S A **97**(26): 14245-50.

Boisset, N., J. C. Taveau, J. Lamy, T. Wagenknecht, M. Radermacher and J. Frank (1990). "Three-dimensional reconstruction of native *Androctonus australis* hemocyanin." J Mol Biol **216**(3): 743-60.

Booth, C. R., W. Jiang, M. L. Baker, Z. H. Zhou, S. J. Ludtke and W. Chiu (2004). "A 9 angstroms single particle reconstruction from CCD captured images on a 200 kV electron cryomicroscope." J Struct Biol **147**(2): 116-27.

Boyd, C. (2008). "Data-parallel computing." Queue **6**(2): 30--39.

Bracewell, R. N. (1965). The Fourier Transform and Its Applications. New York, Mc-Graw-Hil.

Bradford, M. M. (1976). "A rapid and sensitive method for the quantitation of microgram quantities of protein utilizing the principle of protein-dye binding." Anal Biochem **72**: 248-54.

Brink, J., S. J. Ludtke, Y. Kong, S. J. Wakil, J. Ma and W. Chiu (2004). "Experimental verification of conformational variation of human fatty acid synthase as predicted by normal mode analysis." Structure **12**(2): 185-91.

Bronstein, I. N. and K. A. Semendjajew (2004). Oxford Users' Guide to Mathematics, Oxford University Press.

Buck, I. (2007a). GPU computing with NVIDIA CUDA International Conference on Computer Graphics and Interactive Techniques, San Diego, California.

Buck, I. (2007b). GPU Computing: Programming a Massively Parallel Processor. Proceedings of the International Symposium on Code Generation and Optimization.

Buck, I., T. Foley, D. Horn, J. Sugerman, K. Fatahalian, M. Houston and P. Hanrahan (2004). "Brook for GPUs: stream computing on graphics hardware." ACM Trans. Graph. **23**(3): 777--786.

Budinger, T. F., G. T. Gullberg and R. H. Huesman (1979). Emission computed tomography, in Image Reconstruction from Projections Berlin, Springer-Verlag.

Burgess, S. A., M. L. Walker, K. Thirumurugan, J. Trinick and P. J. Knight (2004). "Use of negative stain and single-particle image processing to explore dynamic properties of flexible macromolecules." J Struct Biol **147**(3): 247-58.

Burnette, W. N. (1981). "'Western blotting': electrophoretic transfer of proteins from sodium dodecyl sulfate-polyacrylamide gels to unmodified nitrocellulose and radiographic detection with antibody and radioiodinated protein A." Anal Biochem **112**(2): 195-203.

Cambie, R., K. H. Downing, D. Typke, R. M. Glaeser and J. Jin (2007). "Design of a microfabricated, two-electrode phase-contrast element suitable for electron microscopy." Ultramicroscopy **107**(4-5): 329-339.

Carazo, J. M., T. Wagenknecht and J. Frank (1989). "Variations of the three-dimensional structure of the Escherichia coli ribosome in the range of overlap views. An application of the methods of multicone and local single-cone three-dimensional reconstruction." Biophys. J. **55**(3): 465-477.

Castaño-Díez, D., D. Moser, A. Schoenegger, S. Pruggnaller and A. S. Frangakis (2008). "Performance Evaluation of Image Processing Algorithms on the GPU." Journal of Structural Biology **164**(1): 153-160.

Champeney, D. C. (1973). Fourier Transforms and Their Physical Applications. London Academic Press.

Chapman-Smith, A. and J. E. Cronan, Jr. (1999). "Molecular biology of biotin attachment to proteins." J Nutr **129**(2S Suppl): 477S-484S.

Che, S., M. Boyer, J. Meng, D. Tarjan, J. W. Sheaffer and K. Skadron (2008). "A performance study of general-purpose applications on graphics processors using CUDA." J. Parallel Distrib. Comput. **68**(10): 1370-1380.

Chen, Y.-K., J. Chhugani, P. Dubey, C. J. Hughes, K. Daehyun, S. Kumar, V. W. Lee, A. D. Nguyen and M. Smelyanskiy (2008). "Convergence of Recognition, Mining, and Synthesis Workloads and Its Implications." Proceedings of the IEEE **96**(5): 790-807.

Crick, F. H. C. (1988). What Mad Pursuit: A Personal View of Scientific Discovery, Basic Books.

Crowe, J., H. Dobeili, R. Gentz, E. Hochuli, D. Stuber and K. Henco (1994). "6xHis-Ni-NTA chromatography as a superior technique in recombinant protein expression/purification." Methods Mol Biol **31**: 371-87.

Dagum, L. and R. Menon (1998). "OpenMP: An Industry-Standard API for Shared-Memory Programming." IEEE Comput. Sci. Eng. **5**(1): 46--55.

Danev, R. and K. Nagayama (2001). "Transmission electron microscopy with Zernike phase plate." Ultramicroscopy(88): 243–252

De Haas, F., J. C. Taveau, N. Boisset, O. Lambert, S. N. Vinogradov and J. N. Lamy (1996). "Three-dimensional Reconstruction of the Chlorocruorin of the Polychaete Annelid *Eudistylia vancouverii*." Journal of Molecular Biology **255**(1): 140-153.

Denk, W., J. H. Strickler and W. W. Webb (1990). "Two-photon laser scanning fluorescence microscopy." Science **248**(4951): 73-6.

DeRosier, D. J. and A. Klug (1968). "Reconstruction of three dimensional structures from electron micrographs." Nature **217**(130).

Downing, K. H. (1991). "Spot-scan imaging in transmission electron microscopy." Science **251**(4989): 53-9.

Dube, P., R. Tavares, R. Lurz and M. van Heel (1993). "The portal protein of bacteriophage SPP1: a DNA pump with 13-fold symmetry." EMBO J **12**(4): 1303-1309.

Flynn, M. J. (1972). "Some computer organizations and their effectiveness." IEEE Transactions on Computers **21**(9): 948-960

Frank, J. (1973). "The envelope of electron microscopic transfer functions for partially coherent illumination." Optik **38**(5): 519-536.

Frank, J. (1996). Three-Dimensional Electron Microscopy of Macromolecular Assemblies, Academic Press, Inc.

Frank, J. (2002). "Single-particle imaging of macromolecules by cryo-electron microscopy." Annu Rev Biophys Biomol Struct **31**: 303-19.

- Frank, J., J. P. Bretaudiere, J. M. Carazo, A. Verschoor and T. Wagenknecht (1988). "Classification of images of biomolecular assemblies: a study of ribosomes and ribosomal subunits of Escherichia coli." J Microsc **150**(Pt 2): 99-115.
- Frank, J., P. Penczek, R. Grassucci and S. Srivastava (1991). "Three-dimensional reconstruction of the 70S Escherichia coli ribosome in ice: the distribution of ribosomal RNA." J Cell Biol **115**(3): 597-605.
- Frank, J., M. Radermacher, P. Penczek, J. Zhu, Y. Li, M. Ladjadj and A. Leith (1996). "SPIDER and WEB: processing and visualization of images in 3D electron microscopy and related fields." J Struct Biol **116**(1): 190-9.
- Fu, J., H. Gao and J. Frank (2007). "Unsupervised classification of single particles by cluster tracking in multi-dimensional space." J Struct Biol **157**(1): 226-39.
- Gabashvili, I. S., R. K. Agrawal, C. M. Spahn, R. A. Grassucci, D. I. Svergun, J. Frank and P. Penczek (2000). "Solution structure of the E. coli 70S ribosome at 11.5 Å resolution." Cell **100**(5): 537-49.
- Gande, R. (2005). Untersuchungen zur Lipid- und Zellwandsynthese in Corynebacterium glutamicum. Düsseldorf, Heinrich-Heine-Universität.
- Gande, R., L. G. Dover, K. Krumbach, G. S. Besra, H. Sahn, T. Oikawa and L. Eggeling (2007). "The two carboxylases of Corynebacterium glutamicum essential for fatty acid and mycolic acid synthesis." J Bacteriol **189**(14): 5257-64.
- Gao, H., M. Valle, M. Ehrenberg and J. Frank (2004). "Dynamics of EF-G interaction with the ribosome explored by classification of a heterogeneous cryo-EM dataset." J Struct Biol **147**(3): 283-90.
- Gao, N., A. V. Zavialov, W. Li, J. Sengupta, M. Valle, R. P. Gursky, M. Ehrenberg and J. Frank (2005). "Mechanism for the disassembly of the posttermination complex inferred from cryo-EM studies." Mol Cell **18**(6): 663-74.
- Gilbert, P. (1972). "Iterative methods for the three-dimensional reconstruction of an object from projections." J. theor. Biol. **36**: 105–117.
- Glaeser, R. M. (1999). "Review: electron crystallography: present excitement, a nod to the past, anticipating the future." J Struct Biol **128**(1): 3-14.
- Glaeser, R. M. (2004). "Historical background: Why is it important to improve automated particle selection methods?" J Struct Biol **145**(1-2): 15-8.
- Glaeser, R. M. and K. H. Downing (1992). "Assessment of resolution in biological electron crystallography." Ultramicroscopy **47**(1-3): 256-65.
- Golas, M. M., B. Sander, C. L. Will, R. Luhrmann and H. Stark (2003). "Molecular architecture of the multiprotein splicing factor SF3b." Science **300**(5621): 980-4.

- Golas, M. M., B. Sander, C. L. Will, R. Luhrmann and H. Stark (2005). "Major conformational change in the complex SF3b upon integration into the spliceosomal U11/U12 di-snRNP as revealed by electron cryomicroscopy." Mol Cell **17**(6): 869-83.
- Gordon, R., R. Bender and G. T. Herman (1970). "Algebraic Reconstruction Techniques (ART) for Three-dimensional Electron Microscopy and X-ray Photography." J. theor. Biol. **29**: 471-481.
- Gottschalk, A., G. Neubauer, J. Banroques, M. Mann, R. Luhrmann and P. Fabrizio (1999). "Identification by mass spectrometry and functional analysis of novel proteins of the yeast [U4/U6.U5] tri-snRNP." EMBO J **18**(16): 4535-48.
- Govindaraju, N. K., B. Lloyd, Y. Dotsenko, B. Smith and J. Manferdelli (2008). High performance discrete Fourier transforms on graphics processors. Proceedings of the 2008 ACM/IEEE conference on Supercomputing, Austin, Texas, IEEE Press.
- Guchhait, R. B., S. E. Polakis, P. Dimroth, E. Stoll, J. Moss and M. D. Lane (1974). "Acetyl coenzyme A carboxylase system of Escherichia coli. Purification and properties of the biotin carboxylase, carboxyltransferase, and carboxyl carrier protein components." J Biol Chem **249**(20): 6633-45.
- Gustafson, J. (1988). "Reevaluating Amdahl's Law." Communications of the ACM **31**(5): 532-533.
- Haider, M., S. Uhlemann, E. Schwan, H. Rose, B. Kabius and K. Urban (1998). "Electron microscopy image enhanced." Nature(392): 768.
- Harauz, G. and M. van Heel (1986). "Direct 3D Reconstruction From Projections With Initially Unknown Angles." Pattern Recognition and Image Processing **2**: 279-288.
- Hawkes, P. W. and E. Kasper (1996). Principles of Electron Optics. New York, Acad Press.
- Henderson, R. (1995). "The potential and limitations of neutrons, electrons and X-rays for atomic resolution microscopy of unstained biological molecules." Q Rev Biophys **28**(2): 171-93.
- Hensley, J. (2007). AMD CTM overview. SIGGRAPH '07: ACM SIGGRAPH 2007 courses, ACM: 7.
- Herlihy, M. (1991). "Wait-Free Synchronization." ACM Transactions on Programming Languages and Systems **13**(1): 124-149.
- Herlihy, M. and V. Luchangco (2008). "Distributed computing and the multicore revolution." SIGACT News **39**(1): 62-72.
- Herlihy, M. and J. E. B. Moss (1993). "Transactional memory: Architectural support for lock-free data structures." Proceedings of the 20th Annual International Symposium on Computer Architecture: 289-300.
- Heseler, K. (2005). Untersuchungen zu Acyl-CoA Carboxylasen in *Corynebacterium Glutamicum*. Düsseldorf, Heinrich-Heine-Universität.

Heymann, J. B., J. F. Conway and A. C. Steven (2004). "Molecular dynamics of protein complexes from four-dimensional cryo-electron microscopy." J Struct Biol **147**(3): 291-301.

Hoppe, W., H. J. Schramm, M. Sturm, N. Hunsmann and J. Gaßmann (1976a). "Three-dimensional electron microscopy of individual biological objects. I. Methods." Z. Naturforsch. **31a**: 645–655.

Hoppe, W., H. J. Schramm, M. Sturm, N. Hunsmann and J. Gaßmann (1976b). "Three-dimensional electron microscopy of individual biological objects. II. Test calculations." Z. Naturforsch. **31a**: 1370.

Hoppe, W., H. J. Schramm, M. Sturm, N. Hunsmann and J. Gaßmann (1976c). "Three-dimensional electron microscopy of individual biological objects. III. Experimental results on yeast fatty acid synthetase." Z. Naturforsch. **31a**.

Hou, Q., K. Zhou and B. Guo (2008). "BSGP: bulk-synchronous GPU programming." ACM Trans. Graph. **27**(3): 1-12.

Iwasaki, K., K. Mitsuoka, Y. Fujiyoshi, Y. Fujisawa, M. Kikuchi, K. Sekiguchi and T. Yamada (2005). "Electron tomography reveals diverse conformations of integrin α IIb β 3 in the active state." J Struct Biol **150**(3): 259-67.

Jager, W., P. G. Peters-Wendisch, J. Kalinowski and A. Puhler (1996). "A *Corynebacterium glutamicum* gene encoding a two-domain protein similar to biotin carboxylases and biotin-carboxyl-carrier proteins." Arch Microbiol **166**(2): 76-82.

Joyeux, L. and P. A. Penczek (2002). "Efficiency of 2D alignment methods." Ultramicroscopy **92**(2): 33-46.

Kahle, J. and IBM (2005). The Cell Processor Architecture. Proceedings of the 38th Annual IEEE/ACM International Symposium on Microarchitecture: 3.

Kastner, B. (1998). RNP Particles, Splicing and Autoimmune diseases. Berlin, Springer.

Kastner, B., N. Fischer, M. M. Golas, B. Sander, P. Dube, D. Boehringer, K. Hartmuth, J. Deckert, F. Hauer, E. Wolf, H. Uchtenhagen, H. Urlaub, F. Herzog, J. M. Peters, D. Poerschke, R. Luhrmann and H. Stark (2008). "GraFix: sample preparation for single-particle electron cryomicroscopy." Nat Methods **5**(1): 53-5.

Kimura, Y., T. Kojyo, I. Kimura and M. Sato (1998). "Propionyl-CoA carboxylase of *Myxococcus xanthus*: catalytic properties and function in developing cells." Arch Microbiol **170**(3): 179-84.

Klaholz, B. P., T. Pape, A. V. Zavialov, A. G. Myasnikov, E. V. Orlova, B. Vestergaard, M. Ehrenberg and M. van Heel (2003). "Structure of the *Escherichia coli* ribosomal termination complex with release factor 2." Nature **421**(6918): 90-4.

Klar, T. A., S. Jakobs, M. Dyba, A. Egnér and S. W. Hell (2000). "Fluorescence microscopy with diffraction resolution barrier broken by stimulated emission." Proc Natl Acad Sci U S A **97**(15): 8206-10.

Knoll, M. and E. Ruska (1932). "Das Elektronenmikroskop." Z. Physik(78): 318-339.

Knowles, J. R. (1989). "The mechanism of biotin-dependent enzymes." Annu Rev Biochem **58**: 195-221.

Kondo, H., K. Shiratsuchi, T. Yoshimoto, T. Masuda, A. Kitazono, D. Tsuru, M. Anai, M. Sekiguchi and T. Tanabe (1991). "Acetyl-CoA carboxylase from *Escherichia coli*: gene organization and nucleotide sequence of the biotin carboxylase subunit." Proc Natl Acad Sci U S A **88**(21): 9730-3.

Lathe, G. H. and C. R. Ruthven (1955). "The separation of substances on the basis of their molecular weights, using columns of starch and water." Biochem J **60**(4): xxxiv.

Lebart, L., A. Morineau and K. M. Warwick (1984). Multivariate Descriptive Statistical Analysis: Correspondence Analysis and Related Techniques for Large Matrices. New York.

Leschziner, A. E. and E. Nogales (2006). "The orthogonal tilt reconstruction method: An approach to generating single-class volumes with no missing cone for ab initio reconstruction of asymmetric particles." Journal of Structural Biology **153**: 284-299.

Leschziner, A. E. and E. Nogales (2007). "Visualizing flexibility at molecular resolution: analysis of heterogeneity in single-particle electron microscopy reconstructions." Ann Rev Biophys Biomol Struct **3**: 43-62.

Ludtke, S. J., P. R. Baldwin and W. Chiu (1999). "EMAN: semiautomated software for high-resolution single-particle reconstructions." J Struct Biol **128**(1): 82-97.

Ludtke, S. J., D. H. Chen, J. L. Song, D. T. Chuang and W. Chiu (2004). "Seeing GroEL at 6 Å resolution by single particle electron cryomicroscopy." Structure **12**(7): 1129-36.

Majorovits, E., B. Barton, K. Schultheiss, F. Perez-Willard, D. Gerthsen and R. R. Schroder (2007). "Optimizing phase contrast in transmission electron microscopy with an electrostatic (Boersch) phase plate." Ultramicroscopy **107**(2-3): 213-226.

Marabini, R. and J. M. Carazo (1994). "Pattern recognition and classification of images of biological macromolecules using artificial neural networks." Biophys J **66**(6): 1804-14.

Mark, W. R., R. S. Glanville, K. Akeley and M. J. Kilgard (2003). "Cg: a system for programming graphics hardware in a C-like language." ACM SIGGRAPH 2003 Papers 896-907.

Matsumoto, T. and A. Tonomura (1996). "The phase constancy of electron waves traveling through Boersch's electrostatic phase plate." Ultramicroscopy **63**(1): 5-10.

MERCURY, C. S. I. (2006). "CELL PROCESSOR FOR PC WORKSTATION." Computer Workstations: 3-5.

- Mersereau, R. M. and A. V. Oppenheim (1974). "Digital reconstruction of multidimensional signals from their projections." Proc. IEEE **62**: 1319-1338.
- Moore, G. E. (1965). "Cramming More Components Onto Integrated Circuits." Electronics Magazine **38**(8): 114-117.
- Moreland, K. and E. Angel (2003). The FFT on a GPU. Proceedings of the ACM SIGGRAPH/EUROGRAPHICS conference on Graphics hardware.
- Munshi, A. (2008). "OpenCL Parallel Computing on the GPU and CPU." SIGGRAPH 2008: Beyond Programmable Shading: Fundamentals. from <http://s08.idav.ucdavis.edu/munshi-opencl.pdf>.
- Nickolls, J., I. Buck, M. Garland and K. Skadron (2008). "Scalable parallel programming with CUDA." Queue **6**(2): 40--53.
- Nyquist, H. (1928). "Certain Topics in Telegraph Transmission Theory." Transactions of the American Institute of Electrical Engineers **47**: 617-644.
- Park, S.-Y. and S. Hariri (1997). "A High Performance Message-Passing System for Network of Workstations." J. Supercomput. **11**(2): 159-180.
- Pascual-Montano, A., L. E. Donate, M. Valle, M. Barcena, R. D. Pascual-Marqui and J. M. Carazo (2001). "A novel neural network technique for analysis and classification of EM single-particle images." J Struct Biol **133**(2-3): 233-45.
- Penczek, P. A. (2005). Resolution Measures in Single Particle Analysis. Single Particle Reconstructions and Visualization. S. J. Ludtke. Houston, TX.
- Penczek, P. A., R. A. Grassucci and J. Frank (1994a). "The ribosome at improved resolution: new techniques for merging and orientation refinement in 3D cryo-electron microscopy of biological particles." Ultramicroscopy **53**(3): 251-70.
- Penczek, P. A., R. A. Grassucci and J. Frank (1994b). "The ribosome at improved resolution: New techniques for merging and orientation refinement in 3D cryo-electron microscopy of biological particles." Ultramicroscopy **53**(3): 251-270.
- Penczek, P. A., M. Radermacher and J. Frank (1992). "Three-dimensional reconstruction of single particles embedded in ice." Ultramicroscopy **40**(1): 33-53.
- Penczek, P. A., J. Zhu and J. Frank (1996). "A common-lines based method for determining orientations for $N > 3$ particle projections simultaneously." Ultramicroscopy **63**(3-4): 205-18.
- Peters-Wendisch, P. G., B. Schiel, V. F. Wendisch, E. Katsoulidis, B. Mockel, H. Sahm and B. J. Eikmanns (2001). "Pyruvate carboxylase is a major bottleneck for glutamate and lysine production by *Corynebacterium glutamicum*." J Mol Microbiol Biotechnol **3**(2): 295-300.
- Pharr, M. and R. Fernando (2005). GPU Gems 2: Programming Techniques for High-Performance Graphics and General-Purpose Computation (Gpu Gems), Addison-Wesley Professional.

Pratt, W. K. (1991). Digital image processing. New York, John Wiley and Sons.

Qiagen (2003). The QIAexpressionist™ A handbook for high-level expression and purification of 6xHis-tagged proteins, 5th edn. Valencia, CA, QUIAGEN Inc.

Radermacher, M. and W. Hoppe (1978). 3-D reconstruction from conically tilted projections. Proceedings of the 9th International Congress on Electron Microscopy.

Radermacher, M., T. Wagenknecht, A. Verschoor and J. Frank (1987). "Three-dimensional reconstruction from a single-exposure, random conical tilt series applied to the 50S ribosomal subunit of Escherichia coli." J Microsc **146**(Pt 2): 113-36.

Radon, J. (1917). "Über die Bestimmung von Funktionen durch ihre Integralwerte längs gewisser Mannigfaltigkeiten. ." Ber. Verh. König. Sächs. Ges. Wiss. Leipzig, Math. Phys. **69**: 262–267.

Rainwater, D. L. and P. E. Kolattukudy (1982). "Isolation and characterization of acyl coenzyme A carboxylases from Mycobacterium tuberculosis and Mycobacterium bovis, which produce multiple methyl-branched mycocerosic acids." J Bacteriol **151**(2): 905-11.

Reimer, L. (1997). Transmission electron microscopy; physics of image formation and microanalysis. Berlin; Heidelberg; New York, Springer Verlag.

Rempfer, G. F., D. M. Desloge, W. P. Skoczylas and O. H. Griffith (1997). "Simultaneous correction of spherical and chromatic aberrations with an electron mirror: An electron optical achromat." Microsc Microanal **3**(1): 14-27.

Rose, H. and D. Preikszas (1995). "Time-dependent perturbation formalism for calculating the aberration of systems with large ray gradients." Nuclear Instruments and Methods in Physics Research Section A **363**: 301-315.

Rosenthal, P. B. and R. Henderson (2003). "Optimal determination of particle orientation, absolute hand, and contrast loss in single-particle electron cryomicroscopy." J. Mol. Biol. **333**: 721-745.

Ruska, E. and M. Knoll (1931). "Die magnetische Sammelspule für schnelle Elektronenstrahlen." Z. techn. Physik(12): 389-400 and 448.

Rye, H. S., A. M. Roseman, S. Chen, K. Furtak, W. A. Fenton, H. R. Saibil and A. L. Horwich (1999). "GroEL-GroES cycling: ATP and nonnative polypeptide direct alternation of folding-active rings." Cell **97**(3): 325-38.

Saad, A., S. J. Ludtke, J. Jakana, F. J. Rixon, H. Tsuruta and W. Chiu (2001). "Fourier amplitude decay of electron cryomicroscopic images of single particles and effects on structure determination." J Struct Biol **133**(1): 32-42.

Samols, D., C. G. Thornton, V. L. Murtif, G. K. Kumar, F. C. Haase and H. G. Wood (1988). "Evolutionary conservation among biotin enzymes." J Biol Chem **263**(14): 6461-4.

- Sander, B., M. M. Golas, E. M. Makarov, H. Brahm, B. Kastner, R. Luhrmann and H. Stark (2006). "Organization of core spliceosomal components U5 snRNA loop I and U4/U6 Di-snRNP within U4/U6.U5 Tri-snRNP as revealed by electron cryomicroscopy." Mol Cell **24**(2): 267-78.
- Sander, B., M. M. Golas and H. Stark (2003a). "Automatic CTF correction for single particles based upon multivariate statistical analysis of individual power spectra." J Struct Biol **142**(3): 392-401.
- Sander, B., M. M. Golas and H. Stark (2003b). "Corrim-based alignment for improved speed in single-particle image processing." J Struct Biol **143**(3): 219-28.
- Sander, B., M. M. Golas and H. Stark (2005). "Advantages of CCD detectors for de novo three-dimensional structure determination in single-particle electron microscopy." J Struct Biol **151**(1): 92-105.
- Saxton, W. O. and W. Baumeister (1982). "The correlation averaging of a regularly arranged bacterial cell envelope protein." J Microsc **127**(Pt 2): 127-38.
- Schaller, R. R. (1997). "Moore's law: past, present and future." Spectrum, IEEE **34**(6): 52-59.
- Schatz, M., E. V. Orlova, P. Dube, H. Stark, F. Zemlin and M. van Heel (1997). "Angular Reconstitution in Three-Dimensional Electron Microscopy: Practical and Technical aspects." Scanning Microscopy **11**: 179-193.
- Scherzer, O. (1936). "On Some Errors of Electron Lenses." Z. Physik(101): 593.
- Scherzer, O. (1947). "Sphärische und chromatische Korrektur von Elektronenlinsen." Optik **2**: 114-132.
- Scherzer, O. (1949). "The theoretical resolution limit of the electron microscope." J. Appl. Phys. (20): 20.
- Schroder, R. R., B. Barton, H. Rose and G. Benner (2007). "Contrast enhancement by anamorphic phase plates in an aberration corrected TEM." Microscopy and Microanalysis **13**: 136-137.
- Seiler, L., D. Carmean, E. Sprangle, T. Forsyth, M. Abrash, P. Dubey, S. Junkins, A. Lake, J. Sugerman, R. Cavin, R. Espasa, E. Grochowski, T. Juan and P. Hanrahan (2008). "Larrabee: A Many-Core x86 Architecture for Visual Computing." ACM Transactions on Graphics **27**(3).
- Sherman, M. B. and W. Chiu (1997). "Reliability of phases retrieved from 400-kV spot-scan images of purple membranes acquired on a slow-scan CCD camera." J Microsc **188**(Pt 3): 285-9.
- Smith, L. and M. Bull (2001). "Development of mixed mode MPI / OpenMP applications." Sci. Program. **9**(2,3): 83--98.

- Stark, H. and R. Luhrmann (2006). "Cryo-electron microscopy of spliceosomal components." Annu Rev Biophys Biomol Struct **35**: 435-57.
- Stark, H., F. Mueller, E. V. Orlova, M. Schatz, P. Dube, T. Erdemir, F. Zemlin, R. Brimacombe and M. van Heel (1995). "The 70S Escherichia coli ribosome at 23 Å resolution: fitting the ribosomal RNA." Structure **3**(8): 815-21.
- Stark, H., E. V. Orlova, J. Rinke-Appel, N. Junke, F. Mueller, M. Rodnina, W. Wintermeyer, R. Brimacombe and M. van Heel (1997). "Arrangement of tRNAs in pre- and posttranslocational ribosomes revealed by electron cryomicroscopy." Cell **88**(1): 19-28.
- Stark, H., J. W. Woods, I. Paul and R. Hingorani (1981). "Direct Fourier reconstruction in computer tomography." IEEE Trans. Acoust. Speech Signal Process. **29**: 237-245.
- Stark, H., F. Zemlin and C. Boettcher (1996). "Electron radiation damage to protein crystals of bacteriorhodopsin at different temperatures." Ultramicroscopy **63**: 75-79.
- Steinkilberg, M. and H. J. Schramm (1980). "Eine verbesserte Drehkorrelationsmethode für die Strukturbestimmung biologischer Makromoleküle durch Mittelung elektronenmikroskopischer Bilder." Z. Physiol. Chem. **361**: 1363-1369.
- Stoops, J. K., C. Momany, S. R. Ernst, R. M. Oliver, J. P. Schroeter, J. P. Breaudiere and M. L. Hackert (1991). "Comparisons of the low-resolution structures of ornithine decarboxylase by electron microscopy and X-ray crystallography: the utility of methylamine tungstate stain and Butvar support film in the study of macromolecules by transmission electron microscopy." J Electron Microscop Tech **18**(2): 157-66.
- Stratton, J. A., S. S. Stone and W. W. Hwu (2008). MCUDA: An Efficient Implementation of CUDA Kernels for Multi-core CPUs. 21st Annual Workshop on Languages and Compilers for Parallel Computing (LCPC'2008).
- Sutter, H. (2005). "The Free Lunch Is Over: A Fundamental Turn Toward Concurrency in Software." Dr. Dobbs's Journal **30**(3).
- Sutter, H. and J. Larus (2005). "Software and the concurrency revolution." Queue **3**(7): 54-62.
- Sutton, M. R., R. R. Fall, A. M. Nervi, A. W. Alberts, P. R. Vagelos and R. A. Bradshaw (1977). "Amino acid sequence of Escherichia coli biotin carboxyl carrier protein (9100)." J Biol Chem **252**(11): 3934-40.
- Tarditi, D., S. Puri and J. Oglesby (2005). "Accelerator: simplified programming of graphics-processing units for general-purpose uses via data-parallelism." Technical Report MSR-TR-2004-184, Microsoft Corporation.
- Tarditi, D., S. Puri and J. Oglesby (2006). Accelerator: using data-parallelism to program GPUs for general-purpose uses. 12th International Conference on Architectural Support for Programming Languages and Operating Systems. San Jose, California, USA; .
- Taylor, K. A. and R. M. Glaeser (1974). "Electron diffraction of frozen, hydrated protein crystals." Science **186**(4168): 1036-7.

- Taylor, K. A., J. Tang, Y. Cheng and H. Winkler (1997). "The use of electron tomography for structural analysis of disordered protein arrays." J Struct Biol **120**(3): 372-86.
- Thon, F. (1966). "Zur Defokussierungsabhaengigkeit des Phasenkontrastes bei der elektronenmikroskopischen Abbildung." Z. Naturforschg(21a): 476-478.
- Tilg, Y. (2002). *Lipidsynthese in Corynebacterium glutamicum: Genetische und biochemische Untersuchungen zu Acyl-CoA Carboxylasen*. Düsseldorf, Heinrich-Heine-Universität.
- Tischendorf, G. W., H. Zeichhardt and G. Stoffler (1974). "Determination of the location of proteins L14, L17, L18, L19, L22, L23 on the surface of the 50S ribosomal subunit of Escherichia coli by immune electron microscopy." Mol Gen Genet **134**(3): 187-208.
- Umen, J. G. and C. Guthrie (1995). "A novel role for a U5 snRNP protein in 3' splice site selection." Genes Dev **9**(7): 855-68.
- Unwin, N. (2003). "Structure and action of the nicotinic acetylcholine receptor explored by electron microscopy." FEBS Lett **555**(1): 91-5.
- Vainshtein, B. K. (1971). "The synthesis of projecting functions." Sov. Phys. Dokl. **16**: 66-69.
- Valentine, R. C., B. M. Shapiro and E. R. Stadtman (1968). "Regulation of glutamine synthetase. XII. Electron microscopy of the enzyme from Escherichia coli." Biochemistry **7**(6): 2143-52.
- Valle, M., J. Sengupta, N. K. Swami, R. A. Grassucci, N. Burkhardt, K. H. Nierhaus, R. K. Agrawal and J. Frank (2002). "Cryo-EM reveals an active role for aminoacyl-tRNA in the accommodation process." EMBO J **21**(13): 3557-67.
- Valle, M., A. Zavialov, J. Sengupta, U. Rawat, M. Ehrenberg and J. Frank (2003). "Locking and unlocking of ribosomal motions." Cell **114**(1): 123-34.
- van Heel, M. (1984). "Multivariate statistical classification of noisy images (randomly oriented biological macromolecules)." Ultramicroscopy **13**(1-2): 165 - 183.
- van Heel, M. (1987). "Angular reconstitution: a posteriori assignment of projection directions for 3D reconstruction." Ultramicroscopy **21**(2): 111-23.
- van Heel, M. (2002). *Three Dimensional Imaging of Single Particles*. W. I. P. Organization. GB.
- van Heel, M. (2008). *Pushing the Resolution Limits of cryo-EM. New Algorithms in Macromolecular Crystallography and Electron Microscopy*. J. P. Abrahams. Leiden, NL.
- van Heel, M. and G. Harauz (1986). "Exact filters for general geometry three dimensional reconstruction." Optik **4**: 146-156.

- van Heel, M., G. Harauz and E. V. Orlova (1996). "A new Generation of the IMAGIC Image Processing System." Journal of Structural Biology **116**(1): 17-24.
- van Heel, M. and M. Schatz (2005). "Fourier shell correlation threshold criteria." J Struct Biol **151**(3): 250-62.
- van Heel, M. and M. Stoffler-Meilicke (1985). "Characteristic views of E. coli and B. stearothermophilus 30S ribosomal subunits in the electron microscope." EMBO J **4**(9): 2389-95.
- Vogel, S. and S. Wainwright (1969). A Functional Bestiary, Laboratory Studies About Living Systems, Addison-Wesley Publishing Co.
- von Neumann, J. (1946). "The Principles of Large-Scale Computing Machines." reprinted in Ann. Hist. Comp. **3**(3): 263-273.
- Wade, R. H. and J. Frank (1977). "Electron microscope transfer functions for partially coherent axial illumination and chromatic defocus spread." Optik **49**(2): 81-92.
- Walker, J. S. (1991). Fast Fourier Transforms. Boca Raton, Fla., CRC.
- Walz, J., D. Typke, M. Nitsch, A. J. Koster, R. Hegerl and W. Baumeister (1997). "Electron Tomography of Single Ice-Embedded Macromolecules: Three-Dimensional Alignment and Classification." J Struct Biol **120**(3): 387-95.
- Wang, C., F. Mueller, C. Engelmann and S. L. Scott (2008). Proactive process-level live migration in HPC environments. Proceedings of the 2008 ACM/IEEE conference on Supercomputing. Austin, Texas, IEEE Press.
- Weber, K. and M. Osborn (1969). "The reliability of molecular weight determinations by dodecyl sulfate-polyacrylamide gel electrophoresis." J Biol Chem **244**(16): 4406-12.
- Wood, H. G. and R. E. Barden (1977). "Biotin enzymes." Annu Rev Biochem **46**: 385-413.
- Wrinn, M. (2007). "Is the free lunch really over? Scalability in Many-core Systems." Intel Whitepaper.
- Zemlin, F. (1988). "Dynamic focussing for recording images from tilted samples in small-spot scanning with a transmission electron microscope." Journal of Electron Microscopy Technique **11**(4): 251-257.
- Zernike, F. (1942). "Phase contrast, a new method for the microscopic observation of transparent objects." Physica(9): 686.
- Zhou, Z. H., W. Liao, R. H. Cheng, J. E. Lawson, D. B. McCarthy, L. J. Reed and J. K. Stoops (2001). "Direct evidence for the size and conformational variability of the pyruvate dehydrogenase complex revealed by three-dimensional electron microscopy. The "breathing" core and its functional relationship to protein dynamics." J Biol Chem **276**(24): 21704-13.

Zuzan, H., A. Holbrook, P. T. Kim and G. Harauz (1998). "Self-organization of cryoelectron micrographs of the phosphoenolpyruvate synthase from *Staphylothermus marinus*." Optik **109**: 181-189.

Curriculum Vitae

Martin Schmeißer, M.Sc. (Physics)

Born: April 29, 1975 in Hamburg, Germany

MPI for Biophysical Chemistry

Department of 3D Electron Cryomicroscopy

Am Fassberg 11, 37077 Goettingen, Germany

Phone: +49 (0)176 21 20 66 08

eMail: mschmei@gwdg.de



University Studies

04/2006 – 03/2009

Doctoral Studies, GGNB, Goettingen Graduate School for Neurosciences and Molecular Biosciences, Goettingen, Germany

Ph.D. thesis "New computational methods for 3D structure determination of macromolecular complexes by single particle cryo-EM", Department of **Three-dimensional Electron Cryomicroscopy, MPI for Biophysical Chemistry**, Goettingen, Germany

03/2004 – 03/2005

Master thesis "Towards Video Rate 4-Pi Microscopy", Department of **Nanobiophotonics, MPI for Biophysical Chemistry**, Goettingen, Germany

10/2002 – 01/2004

Graduate Studies, Physics, GGSP, Goettingen Graduate School of Physics, Goettingen, Germany

* 02/1997 – 09/2002

CID GmbH Startup Phase, Co-Founder, R&D, software architecture and technical infrastructure, Gelnhausen, Germany

06/1999

Diploma Examination, Astronomy and Astrophysics, **DUT**, Darmstadt University of Technology, Darmstadt, Germany

01/1999 – 03/1999

Stay abroad, JUAS, Joint Universities Accelerator School, arranged by CAS, **CERN** Accelerator School, Geneva, Switzerland, Archamps, France

10/1997 – 10/1998

Graduate Studies, Diploma Examination, Software Engineering, Institute for applied computer science, **DUT**, Darmstadt University of Technology, Darmstadt, Germany

10/1995 – 03/1998

Undergraduate Studies, Pre-Diploma Examination, Physics, **DUT**, Darmstadt University of Technology, Darmstadt, Germany

* Entrepreneurship

- 10/2000 – 09/2002 Step up of CID to **CID GmbH** (Limited Liability Company under German Law), **Partner**, R&D, technical infrastructure, Gelnhausen, Germany
- 02/1997 – 09/2000 **Co Founder** of **CID** – Creative Internet Dienste (Creative Internet Solutions), Initial set-up during startup phase as partnership under German Civil Code, R&D, software architecture and technical infrastructure, Gelnhausen, Germany

Project Management

- 04/2002 – 04/2005 Network-Administration / **IT-Structure Organization**, **IT-Delegate**, Department of **Nanobiophotonics**, **MPI BPC**, Goettingen, Germany
- 10/2002 – 03/2006 **Free lance consultant** for eBusiness and eCommerce, Goettingen, Germany
- 02/1997 – 09/2002 **Project Management**, Software architecture design and Consulting in the main areas of eCommerce, eBusiness and eProcurement, as a **Partner and Co-Founder** of **CID**, Creative Internet Dienste GmbH, Gelnhausen, Germany
- 02/1999 “Building an accelerator together“, **Project Management** of an international team of 25 students on the design of a fast cycling synchrotron for **CERN**, Geneva, Switzerland
- 10/1997 – 10/1998 **Quality management** and **Project Management** during development of an online information system for public transport “**phi-punkt Software Engineering**“, Darmstadt, Germany